



Doctoral Thesis

## Imaging techniques to study nickel-root interactions of the Ni hyperaccumulator plant *Berkheya coddii*

**Author(s):**

Moradi, Ahmad

**Publication Date:**

2008

**Permanent Link:**

<https://doi.org/10.3929/ethz-a-005705176> →

**Rights / License:**

[In Copyright - Non-Commercial Use Permitted](#) →

This page was generated automatically upon download from the [ETH Zurich Research Collection](#). For more information please consult the [Terms of use](#).

Diss. ETH No. 17773

**Imaging techniques to study nickel-root interactions of the Ni  
hyperaccumulator plant *Berkheya coddii***

A dissertation submitted to the  
SWISS FEDERAL INSTITUTE OF TECHNOLOGY ZURICH

for the degree of  
DOCTOR OF SCIENCES

presented by

AHMAD MORADI  
Master degree, Isfahan University of Technology (IUT)  
born 21 March 1977  
citizen of Iran

accepted on the recommendation of  
Prof. Dr. Rainer Schulin, examiner  
Prof. Dr. Walter Wenzel, co-examiner  
Dr. Sascha Oswald, co-examiner  
Dr. Eberhard Lehmann, co-examiner

2008



*For my parents*



---

# Acknowledgements

---

Many people have contributed to successful completion of this study in various ways, which I gratefully appreciate.

I would like to thank Prof. Dr. Rainer Schulin, for giving me the opportunity to carry out and finish this project with much freedom and for his support and encouragement, when needed. I would also like to thank Dr. Sascha Oswald and Dr. Brett Robinson for their constant advice and support during this time. I feel very lucky to have had them all accompanying me and contributing to my thesis.

I am very grateful to René Saladin, Martin Keller, Werner Attinger, and Anna Grünwald for their technical help in the laboratory and field and for constructing various containers that I used in my experiments.

My thanks also go to Dr. Eberhard Lehmann, Peter Vontobel, Guido Kühne, Gabriel Frei, David Mannes and George Necola for their generous support and technical help to do neutron radiography at Paul Scherer Institut (PSI), Prof. Dr. Klaas Pruessmann, Jurek Massner, and Reto Treier for their contribution and technical help with MRI measurements, Professor Dr. Walter Wenzel, Dr. Walter Fitz, Prof. Dr. Thomas Prohaska, and Siegfried Swoboda for their support, advice and technical help with the rhizobox system and Laser ablation experiment. I am also grateful to Dr. Anders Kaestner for his great help and support to analyse and process the images.

Finally, I would like to thank all the persons who provided a friendly environment at work and contributed in a 'non-scientific' way to the work throughout the last years. This includes the members of the soil protection and soil physics group. I am very grateful to Dr. Hector Conesa for being a great co-worker and a reliable friend at the same time.

My deepest gratitude goes to my parents for their love and unconditional support and encouragement to pursue my interests beyond the boundaries of language, culture, and geography.

## Acknowledgements

---

The financial support of the Swiss National Science Foundation (SNF) is gratefully acknowledged.

---

# Contents

---

<b>Acknowledgements</b>	<b>I</b>
<b>Summary</b>	<b>VII</b>
<b>Zusammenfassung</b>	<b>IX</b>
<b>1 Introduction</b>	<b>1</b>
1.1 Background .....	1
1.2 Objectives of this study .....	4
1.3 References .....	5
<b>2 Magnetic resonance imaging methods to reveal the real-time distribution of nickel in porous media</b>	<b>11</b>
2.1 Abstract .....	12
2.2 Introduction .....	13
2.3 Materials and methods .....	15
2.3.1 Materials' testing .....	15
2.3.2 Ni absorption experiment .....	16
2.3.3 MRI techniques and data analysis .....	16
2.3.4 Modelling .....	18
2.4 Results and discussion .....	19
2.4.1 Testing porous materials by Turbo Spin Echo MRI .....	19
2.4.2 Testing the suitability of different MRI methods .....	20
2.4.3 The absorption experiment .....	25
2.5 Conclusions and applications .....	26
2.6 Acknowledgements .....	27
2.7 References .....	27

<b>3</b>	<b>Analysis of nickel concentration profiles in the rhizosphere of the hyperaccumulator plant, <i>Berkheya coddii</i>, using MRI and numerical simulations</b>	<b>31</b>
3.1	Abstract .....	32
3.2	Introduction .....	33
3.3	Materials and Methods .....	35
3.3.1	Rhizobox setup and plant growth .....	35
3.3.2	MRI technique and data analysis .....	36
3.3.3	Ni uptake experiment .....	37
3.3.4	Modelling .....	38
3.4	Results and discussions .....	38
3.4.1	Temporal changes of Ni distribution .....	38
3.4.2	Ni concentration mapping at different soil water contents .....	40
3.4.3	Modelling Ni <sup>2+</sup> uptake .....	43
3.4.4	Effects of various parameters on Ni <sup>2+</sup> concentration profile .....	44
3.5	Acknowledgements .....	46
3.6	References .....	46
<b>4</b>	<b>Laser ablation mapping of nickel in root cross-sections of the hyperaccumulator plant <i>Berkheya coddii</i></b>	<b>51</b>
4.1	Abstract .....	52
4.2	Introduction .....	53
4.3	Materials and methods .....	54
4.3.1	Rhizobox experiment and sampling .....	54
4.3.2	LA-ICP-MS analysis .....	56
4.3.3	DMG Staining and image processing .....	57
4.4	Results .....	59
4.4.1	Analysis of LA-ICP-MS line scans .....	59
4.4.2	Analysis of DMG-stained root cross-sections .....	59
4.4.3	Two-dimensional map of Ni in root cross-section .....	61
4.4.4	Comparing LA-ICP-MS and DMG staining results .....	62

4.4.5 Comparison of LA-ICP-MS with ICP-OES and XRF results .....	65
4.5 Discussion .....	65
4.6 Conclusions .....	66
4.7 Acknowledgements .....	67
4.8 References .....	67
<b>5 Neutron radiography as a tool for revealing root development in soil: capabilities and limitations</b>	<b>71</b>
5.1 Abstract .....	72
5.2 Introduction .....	73
5.3 Materials and methods .....	74
5.3.1 Neutron and X-ray radiography systems .....	74
5.3.2 Materials testing .....	77
5.3.3 Calibration for soil water content .....	79
5.3.4 Plant growth .....	79
5.3.5 Imaging procedure .....	80
5.3.6 Image analysis .....	80
5.4 Results and discussions .....	83
5.4.1 Analysis of neutron radiographs .....	83
5.4.2 Factors affecting root contrast in NR .....	84
5.4.3 Relationship between $\Sigma$ and $\theta$ .....	86
5.4.4 Root detection .....	86
5.4.5 Minimum detectable root diameter as a function of container thickness	87
5.4.6 Comparing NR with X-ray radiography and soil scanning .....	91
5.4.7 Advantages and limitations of NR for the visualisation of plant roots ..	92
5.5 Conclusions .....	92
5.6 Acknowledgements .....	92
5.7 References .....	93
<b>6 Conclusions</b>	<b>97</b>

6.1 MRI to study dynamics of Ni .....	97
6.2 LA-ICP-MS and DMG-staining to study Ni distribution in root cross-sections	98
6.3 Neutron radiography to monitor root development in soil .....	98
6.4 Ni dynamic in the rhizosphere of <i>Berkheya coddii</i> .....	98
6.5 Outlook .....	99
<b>Curriculum Vitae</b>	<b>101</b>

---

## Summary

---

Although chemical, physical, and biological interactions of soil and roots have been investigated for a long time ago, the quantification of these interactions is still very difficult. Some of the reasons are the complexity of the root-soil interactions, the dynamic nature of roots and rhizosphere processes, and the technical difficulties of any measurements due to the small geometrical scale of the rhizosphere. An ideal tool for studying rhizosphere processes should be non-destructive, non-invasive and have a high spatial and temporal resolution. In this project we developed, adapted and tested some new imaging techniques for rhizosphere studies. In particular we applied (i) magnetic resonance imaging (MRI) to study the dynamics of nickel concentration distributions in a porous medium and rhizosphere, (ii) dimethylglyoxime (DMG) staining and laser ablation inductively coupled plasma mass spectroscopy (LA-ICP-MS) for qualitative and quantitative mapping of Ni distribution inside the root cross-sections, and (iii) neutron radiography (NR) combined with image analysis technique for studying growth and development of roots in soil. We used the Ni hyperaccumulator plant *Berkheya coddii* in all the experiments as a model plant.

To develop and adapt the MRI technique, we tested various porous materials and various MRI imaging sequences. Porous glass beads was found to be the best root-growth medium compatible with MRI. Then we developed a MRI method sensitive to the presence of Ni through the effect of Ni on the relaxation time of hydrogen. The method then was tested to obtain gradients of Ni concentration in a glass beads medium as Ni was sorbed into an exchange resin as a sink for Ni. A real-time map of Ni dynamics with relatively high spatial resolution was obtained.

The developed MRI sequence was used to investigate the temporal and spatial dynamics of Ni in the rhizosphere of *Berkheya coddii*. A high resolution distribution pattern of Ni was obtained. Nickel concentration was found to increase as approaching the root surface showing an exclusion pattern. The observed Ni concentration pattern was simulated using the numerical model, MIN3P. The gradient of Ni adjacent to the root surface was shown using numerical simulations to be a function of concentration, uptake rate, and transpiration.

Two independent methods, LA-ICP-MS and DMG-staining, were used to investigate the qualitative and quantitative distribution of Ni inside the root cross-sections of *Berkheya coddii*. Both methods showed a higher concentration of Ni in the cortex than the stele in the

Ni spiked roots, while the opposite trend was observed for the unspiked roots. This results indicate that an active uptake or ion selection mechanism exists for *Berkheya coddii* at low available Ni.

Finally, we combined neutron radiography with image analysis technique to provide a quantitative tool for root growth and development investigations. Suitability of various root-growth materials for neutron radiography was tested and neutron attenuation coefficient of various materials calculated. We improved the relationship between neutron attenuation coefficient and water content of the soil using neutron scattering correction algorithm. Neutron radiographs were compared with X-ray radiographs and scan images and the capability and limitations of each technique to detect the roots in soil were compared. Neutron radiography was found to detect roots with a thickness larger than 0.2 mm.

The results demonstrate that each technique has its own benefits and limitations in application. To apply each of these techniques in order to study root-soil interactions, compensation between real soil conditions and the requirements of each specific technique is necessary. However, they are valuable tools to address the specific questions in a well defined system. In case of *Berkheya coddii*, it was found to exclude Ni in high concentration of available Ni, although Ni may get depleted in soils with poor content of available Ni. It was shown that *Berkheya coddii* takes up Ni through an active uptake or ion selective mechanisms at low concentration of Ni in the rhizosphere.

---

## Zusammenfassung

---

Obwohl die chemischen, physikalischen und biologischen Interaktionen zwischen Boden und Pflanzenwurzeln bereits seit einiger Zeit erforscht werden, ist die Quantifikation dieser Interaktionen weiterhin schwierig. Gründe dafür sind die Komplexität der Wurzel-Boden Interaktionen, die dynamische Natur der Wurzeln und Prozesse in der Rhizosphäre und technisch Schwierigkeiten bei Messungen aufgrund der geringen Grösse der Rhizosphäre. Deshalb sollte eine ideale Methode für Rhizosphären-Forschung weder destruktiv noch invasiv sein und eine hohe temporäre und räumliche Auflösung bieten. In diesem Projekt haben wir verschiedene neuartige bildgebende Verfahren für die Rhizosphären-Forschung getestet, angepasst und entwickelt. Diese sind im Einzelnen: (i) die Magnetresonanztomographie (MRI) um die Dynamik der Nickel(Ni)-Verteilung in porösen Medien und der Rhizosphäre zu untersuchen, (ii) die Dimethylglyoxime (DMG) Verfärbungs-Methode und Laser ablation inductively coupled plasma mass spectroscopy (LA-ICP-MS) für die quantitative und qualitative Kartierung von Ni in Wurzel-Querschnitten, und Neutronen Radiographie (NR) in Verbindung mit Bildverarbeitungsmethoden für die Untersuchung des Wurzelwachstums im Boden. *Berkheya coddii* Roessl, ein Ni-Hyperakkumulator wurde dabei in allen Experimenten als Modellpflanze benutzt.

Zur Entwicklung und Anpassung einer geeigneten MRI-Technik haben wir verschiedene poröse Materialien als Medien für Pflanzenwachstum in Kombination mit verschiedenen MRI Imaging Sequenzen getestet. Als das am besten mit MRI kompatibel Medium für Wurzelwachstum haben sich poröse Glaskugeln herausgestellt. Anschliessend wurde eine MRI-Methode entwickelt, die auf Ni sensitiv reagiert und auf der Änderung der Relaxationszeit von Wasserstoff unter Anwesenheit von Ni basiert. Diese Methode wurde dann getestet, indem die Veränderung eines Ni-Konzentrationsgradienten in einem Glaskugelmedium durch Sorption von Ni an einem Austauschharz gemessen wurde. Wir erhielten eine Abbildung der Ni-Verteilung in Echtzeit mit einer relativ hohen räumlichen Auflösung.

Die entwickelte MRI Sequenz wurde verwendet, um die temporäre und räumliche Dynamik von Ni in der Rhizosphäre von *Berkheya coddii* zu erforschen. Wir erhielten ein hochaufgelöstes Abbild der Ni-Verteilung. Die Erhöhung der Ni-Konzentration in der Nähe

der Wurzeloberfläche zeigte ein Ausschluss-Schema. Das beobachtete Schema der Ni-Konzentration wurde anschliessend mit dem Numerischen Modell MIN3P simuliert. Mit der numerischen Modellierung konnte gezeigt werden, dass der Ni-Konzentrationsgradient in der Nähe der Wurzeloberfläche von der Ni-Konzentration, der Aufnahmegeschwindigkeit von Ni und der Transpiration der Pflanze abhängig ist.

Zwei eigenständige Methoden, LA-ICP-MS und DMG-Verfärbung, wurden benutzt um die qualitative und quantitative Verteilung von Ni in Wurzel-Querschnitten von *Berkheya coddii* zu ermitteln. Beide Methoden zeigten bei ausgewachsenen Pflanzen in belastetem Boden eine höhere Konzentration von Ni im Cortex als in den Stielen an, während ein gegenseitiger Trend in unbelastetem Boden beobachtet wurde. Diese Ergebnisse legen nahe, dass es eine aktive Aufnahme oder eine Ionen-Selektion bei *Berkheya coddii* gibt wenn die Konzentration von verfügbarem Ni niedrig ist.

Um das Wurzelwachstum quantitativ bestimmen zu können benutzten wir Neutronenradiographie und digitale Bildverarbeitungsmethoden. Verschiedene Medien für die Aufzucht von Pflanzen wurden auf ihre Eignung für die Experimente mit Neutronenstrahlung untersucht und ihr Neutronendämpfungsfaktor gemessen. Unter Verwendung des neutron scattering correction algorithm (Neutronenstreuungskorrekturalgorithmus) verbesserten wir die Beziehung zwischen dem Neutronendämpfungsfaktor und dem Wassergehalt des Bodens.

Um die Möglichkeiten und Grenzen von Neutronenradiographien, Röntgen-Bildern und Bildern der eingescannten Bodenoberfläche im Bezug auf ihre Eignung Wurzeln im Boden zu detektieren, wurden die Bilder miteinander verglichen. Mit Neutronradiographie konnten Wurzeln von 0.2 mm und dicker identifiziert werden.

Die Resultate dieser Studie zeigen, dass jede der eingesetzten Methoden ihre Vor- und Nachteile hat. Eine von diesen Methoden im System Wurzel-Boden anzuwenden, stellt immer einen Kompromiss zwischen den realen Bedingungen im Boden und den Ansprüchen der jeweiligen Methode dar. Allerdings sind sie äusserst wertvoll, um spezifische Fragen in Bezug auf das System Wurzeln-Boden zu beantworten.

---

# 1 Introduction

---

## 1.1 Background

Although chemical, physical and biological interactions of roots and soil and the role of the rhizosphere in plant nutrition have been studied for decades (Clark, 1949; Starkey, 1958; Slavnina, 1971; Barber, 1973; Grinsted *et al.*, 1982; Darrah, 1993), the quantification of soil-root interactions and of rhizosphere processes is still very difficult. The understanding of soil-plant interactions has been lagging behind due to limitations in the experimental accessibility of soil, the microscopic scale of the rhizosphere, and the complexity of these interactions. For example, there is a lack of methods to monitor root development and to determine spatial distributions of chemicals in situ on the micro-scale non-destructively (Figure 1.1). Traditional techniques for studying root functions and morphology are often destructive, tedious, and inaccurate. The need for new non-destructive research technologies to address rhizosphere dynamics is urgent and widely stressed (Gregory & Hinsinger, 1999; Wenzel *et al.*, 2001; Wenzel, 2005; Hertel & Leuschner, 2006; Blossfeld & Gansert, 2007). Moreover, unraveling chemical, physical and biological phenomena in the rhizosphere also requires an understanding of the processes within the roots such as the uptake of solutes and their transport through the roots to the above-ground part of the plants.

Current non-invasive and non-destructive methods for the in-situ studies of roots include rhizoboxes and minirhizotrons, which are transparent plastic tubes inserted into the ground to view the roots using a camera (Youssef & Chino, 1988; Gahoonia & Nielsen, 1991; Dinkelaker *et al.*, 1993; Wenzel *et al.*, 2001; Kuchenbuch & Ingram, 2002), magnetic resonance imaging (Bottomley *et al.*, 1993; Fischer & Hall, 1996; Herrmann *et al.*, 2002; Doussan *et al.*, 2003; Heyes & Clark, 2003; Pierret *et al.*, 2003; Osuga & Han, 2004), neutron radiography and tomography (Willatt *et al.*, 1978; Willatt & Struss, 1979; Bois & Couchat, 1983; Nakanishi *et al.*, 2005; Hassanein *et al.*, 2006; Menon *et al.*, 2007), X-Ray imaging and tomography (Moran *et al.*, 2000; Naftel *et al.*, 2001; Gregory *et al.*, 2003), as well as scanning electron microscopy (Birchem *et al.*, 1981).

Root observation using minirhizotrons is non-destructive once they are in place. However, the installation of rhizotrons is invasive and may perturb root development and water flux (Majdi, 1996). Root growth chambers such as the rhizoboxes developed by Wenzel *et al.* (2001) can greatly facilitate measurements in the rhizosphere of the plants, but

sampling the soil solution of the rhizosphere requires micro suction cups and unavoidably disturbs the distribution of water and solutes around the sampling ports.

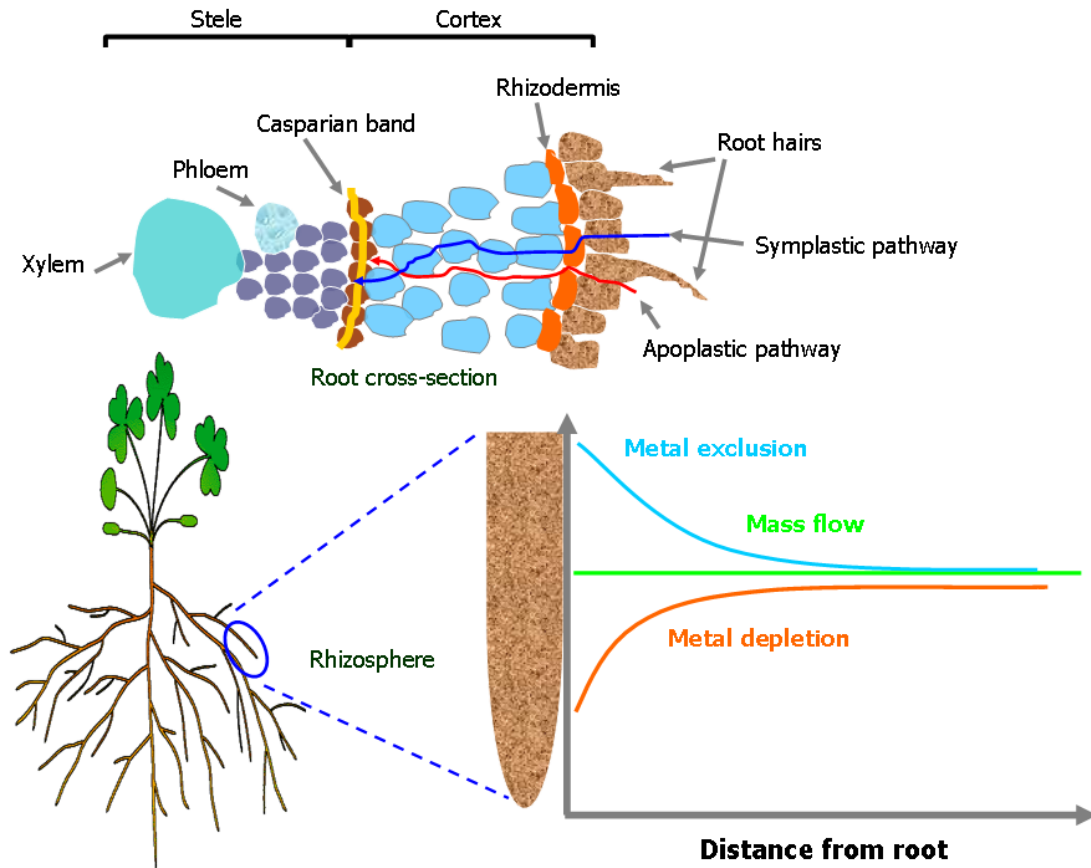


Figure 1.1: Schematic view of the micro-scale distribution of chemicals in the rhizosphere and uptake pathways through the root cross-section

Magnetic Resonance Imaging can provide information on the spatial distribution of water and dissolved ions, and thus also on transport processes (Stapf & Song-I, 2006). One advantage of MRI over other non-destructive methods is its potential for the simultaneous determination of structure and transport processes in real time (Van As & van Dusschoten, 1997). Although MRI can be an effective tool for the detailed study of chemical and physical processes in soil and other porous systems, it suffers from several limitations. MRI is sensitive to paramagnetic and ferromagnetic impurities that are present naturally in soil. These disturb the local magnetic field and thereby distort or destroy the local MRI imaging information (Tollner *et al.*, 1991; Kinchesh *et al.*, 1994; Hall *et al.*, 1997). Therefore, most

studies use carefully selected media or artificial systems with reduced ferromagnetic components such as pre-treated sand and soil, agar medium, glass beads and sand mixtures.

Neutron radiography provides images similar to X-ray radiography. Neutrons interact with the nuclei of atoms while X-rays interact with electrons. Whereas X-ray attenuation increases with the atomic number  $Z$  among different elements, the neutron attenuation does not show such a dependency on  $Z$  and only a few elements such as hydrogen strongly attenuate neutrons. Therefore, H-rich materials such as water and organic matter, in particular roots, are clearly visible in neutron radiographs.

The methods that are currently used for microscopic spatial localization of metals within biological tissues are primarily micro-analytical techniques based on X-ray emission in response to irradiation with charged particles (Bhatia *et al.*, 2004), including micro-PIXE (micro proton-induced X-ray emission spectroscopy; also known as nuclear microprobe) and EDXS (energy dispersive X-ray spectroscopy). Both methods simultaneously measure and map elemental contents. While micro-PIXE gives higher analytical sensitivities than EDXS (Przybylowicz *et al.*, 2001), the application of micro-PIXE is limited by the accessibility to a proton-beam facility, of which there are only a few world-wide.

Laser-ablation combined with inductively-coupled-plasma mass-spectrometry (LA-ICP-MS) has become a powerful analytical approach for the micro-scale mapping of a large number of elements with detection limits in the  $\mu\text{g kg}^{-1}$  range. Other key advantages of LA-ICP-MS are excellent sensitivity, reduced sample preparation and relatively high spatial resolution (Russo *et al.*, 2002; Hattendorf *et al.*, 2003). LA-ICP-MS has been successfully used for highly resolved plant biological and physiological analysis (Prohaska *et al.*, 1998; Hoffmann *et al.*, 2000; Polatajko *et al.*, 2007; Ulrich *et al.*, 2007). These methods offer particular potential for the study of metal uptake by hyperaccumulator plants, because the concentration of metals accumulated in plant tissues can be well above the detection limits of these methods without causing toxicity.

Hyperaccumulator plants are of particular practical importance as a sustainable treatment option for the remediation of metal-contaminated sites (mining activity, refinery emissions, waste disposal, fossil fuel combustion, and agricultural application of pesticides and biosolids) and also as an opportunity to mine naturally metal-rich soils i.e. phytomining of ultramafic soils (Brooks *et al.*, 1998; Angle *et al.*, 2001; Li *et al.*, 2003). A nickel hyperaccumulator plant is defined as a plant accumulating Ni at concentrations exceeding  $1000 \text{ mg kg}^{-1}$  dry weight in the above-ground biomass (Reeves *et al.*, 1999). *Berkheya coddii* is a Ni-hyperaccumulator plant that has attracted particular attention because of its high Ni uptake and rapid biomass production. Robinson *et al.* (1997) reported an annual biomass

production of 22 t ha<sup>-1</sup> and up to 1% (w:w) Ni in the above-ground biomass. The combination of these two traits, which is very rare, makes the plant particularly suitable for the remediation of Ni-contaminated soils by means of phytoextraction. *Berkheya coddii* is an asteraceous summer-green perennial plant that is found on ultramafic (serpentine) soils in southern Africa (Morrey *et al.*, 1992). The mechanisms involved in metal hyperaccumulation by plants are still not well understood. Among other reasons, this is also due to a lack in methods for analysing metal distribution and localisation in plant tissues, cells and organelles.

Although above-mentioned techniques have the potential to be used for investigations of root-metal interactions in the rhizosphere, they all have their own limitations and drawbacks. Some of the major limitations often are their need for adaptation to the rhizosphere conditions, their poor detection limit and their performance under variable water-saturation conditions when applied to root-soil system. Little has been done so far to quantitatively assess and evaluate the capability of these methods for rhizosphere studies.

## 1.2 Objectives of this study

The aims of this study were to develop, adapt and apply the above-mentioned imaging techniques to the investigations of nickel-root interactions and metal accumulation by plants, using the Ni accumulator plant *Berkheya coddii* as a model system. The specific objectives of this study were to:

- develop a quantitative MRI technique capable of studying the distribution of Ni in porous media with a spatial and temporal resolution that is adequate for the analysis of rhizosphere processes,
- study the dynamics of Ni in the rhizosphere of *Berkheya coddii* using MRI under well defined conditions,
- determine the distribution of Ni inside the roots of *Berkheya coddii*,
- develop a method to quantify root growth and development in soil using neutron radiography.

The study proceeded in four steps, each of which is described in one of the main chapters of this dissertation:

- (i) Various root-growth media and MRI sequences were tested at first in order to find the best porous medium compatible with MRI. Then we developed a quantitative MRI method sensitive to the presence of Ni for studying the distribution of Ni in porous media with sufficiently high spatial and temporal resolutions. The method was then applied to a glass bead medium with an ion exchange resin as a Ni sink to map the real-time development of the Ni depletion zone around the resin as Ni was sorbed into the resin (Chapter 2).
- (ii) The developed MRI method (Chapter 2) was subsequently applied to the rhizosphere of *Berkheya coddii* grown in a rhizobox system to map the temporal and spatial distribution of Ni adjacent to the roots. A numerical model was used to interpret the observed the distribution pattern of Ni (Chapter 3).
- (iii) In order to study qualitative and quantitative distribution of Ni inside the roots of *Berkheya coddii*, two independent methods, one using laser ablation combined with inductively coupled plasma mass spectrometry (LA-ICP-MS) and the other based on dimethylglyoxime (DMG) staining, were developed and applied to analyze the allocation of accumulated Ni in root cross-sections of *Berkheya coddii*. The results obtained from each technique were compared and discussed (Chapter 4).
- (iv) Combining neutron radiography with image analysis techniques, a quantitative method was developed for studying root growth and development in soil. Various root-growth materials and plant species were analyzed. NR images were compared with X-ray radiographs and scan images in order to assess the relative benefits as well as limitations of NR method (Chapter 5).

### 1.3 References

- Angle, J.S., Chaney, R.L., Baker, A.J.M., Li, Y., Reeves, R., Volk, V., Roseberg, R., Brewer, E., Burke, S. & Nelkin, J. 2001. Developing commercial phytoextraction technologies: practical considerations. *South African Journal of Science*, **97**, 619-623.
- Barber, D.A. 1973. Effects of Microorganisms on the Absorption of Inorganic Nutrients by Plants. *Pesticide Science*, **4**, 367-373.
- Bhatia, N.P., Walsh, K.B., Orlic, I., Siegele, R., Ashwath, N. & Baker, A.J.M. 2004. Studies on spatial distribution of nickel in leaves and stems of the metal hyperaccumulator *Stackhousia tryonii* using nuclear microprobe (micro-PIXE) and EDXS techniques. *Functional Plant Biology*, **31**, 1061-1074.

- Birchem, R., Sommer, H.E. & Brown, C.L. 1981. Scanning Electron-Microscopy of Shoot and Root Development in Sweetgum Callus-Tissue Culture. *Forest Science*, **27**, 206-212.
- Blossfeld, S. & Gansert, D. 2007. A novel non-invasive optical method for quantitative visualization of pH dynamics in the rhizosphere of plants. *Plant Cell and Environment*, **30**, 176-186.
- Bois, J.F. & Couchat, P. 1983. Comparison of the Effects of Water-Stress on the Root Systems of 2 Cultivars of Upland Rice (*Oryza-Sativa-L*). *Annals of Botany*, **52**, 479-487.
- Bottomley, P.A., Rogers, H.H. & Prior, S.A. 1993. Nmr Imaging of Root Water Distribution in Intact Vicia-Faba L Plants in Elevated Atmospheric Co<sub>2</sub>. *Plant Cell and Environment*, **16**, 335-338.
- Brooks, R.R., Chambers, M.F., Nicks, L.J. & Robinson, B.H. 1998. Phytomining. *Trends in Plant Science*, **3**, 359-362.
- Clark, F.E. 1949. Soil Microorganisms and Plant Roots. *Advances in Agronomy*, **1**, 241-288.
- Darrah, P.R. 1993. The Rhizosphere and Plant Nutrition - a Quantitative Approach. *Plant and Soil*, **156**, 1-20.
- Dinkelaker, B., Hahn, G., Romheld, V., Wolf, G.A. & Marschner, H. 1993. Nondestructive Methods for Demonstrating Chemical-Changes in the Rhizosphere .1. Description of Methods. *Plant and Soil*, **156**, 67-70.
- Doussan, C., Pages, L. & Pierret, A. 2003. Soil exploration and resource acquisition by plant roots: an architectural and modelling point of view. *Agronomie*, **23**, 419-431.
- Fischer, A.E. & Hall, L.D. 1996. Visualization of the diffusion of metal ions and organic molecules by magnetic resonance imaging of water. *Magnetic Resonance Imaging*, **14**, 779-783.
- Gahoonia, T.S. & Nielsen, N.E. 1991. A Method to Study Rhizosphere Processes in Thin Soil Layers of Different Proximity to Roots. *Plant and Soil*, **135**, 143-146.
- Gregory, P.J. & Hinsinger, P. 1999. New approaches to studying chemical and physical changes in the rhizosphere: an overview. *Plant and Soil*, **211**, 1-9.
- Gregory, P.J., Hutchison, D.J., Read, D.B., Jenneson, P.M., Gilboy, W.B. & Morton, E.J. 2003. Non-invasive imaging of roots with high resolution X-ray micro-tomography. *Plant and Soil*, **255**, 351-359.
- Grinsted, M.J., Hedley, M.J., White, R.E. & Nye, P.H. 1982. Plant-Induced Changes in the Rhizosphere of Rape (*Brassica-Napus Var - Emerald*) Seedlings .1. Ph Change and the Increase in P Concentration in the Soil Solution. *New Phytologist*, **91**, 19-29.

- Hall, L.D., Amin, M.H.G., Dougherty, E., Sanda, M., Votrubova, J., Richards, K.S., Chorley, R.J. & Cislerova, M. 1997. MR properties of water in saturated soils and resulting loss of MRI signal in water content detection at 2 tesla. *Geoderma*, **80**, 431-448.
- Hassanein, R., Meyer, H.O., Carminati, A., Estermann, M., Lehmann, E. & Vontobel, P. 2006. Investigation of water imbibition in porous stone by thermal neutron radiography. *Journal of Physics D-Applied Physics*, **39**, 4284-4291.
- Hattendorf, B., Latkoczy, C. & Gunther, D. 2003. Laser ablation-ICPMS. *Analytical Chemistry*, **75**, 341A-347A.
- Herrmann, K.H., Pohlmeier, A., Wiese, S., Shah, N.J., Nitzsche, O. & Vereecken, H. 2002. Three-dimensional nickel ion transport through porous media using magnetic resonance Imaging. *Journal of Environmental Quality*, **31**, 506-514.
- Hertel, D. & Leuschner, C. 2006. The in situ root chamber: A novel tool for the experimental analysis of root competition in forest soils. *Pedobiologia*, **50**, 217-224.
- Heyes, J.A. & Clark, C.J. 2003. Magnetic resonance imaging of water movement through asparagus. *Functional Plant Biology*, **30**, 1089-1095.
- Hoffmann, E., Ludke, C., Skole, J., Stephanowitz, H., Ullrich, E. & Colditz, D. 2000. Spatial determination of elements in green leaves of oak trees (*Quercus robur*) by laser ablation-ICP-MS. *Fresenius Journal of Analytical Chemistry*, **367**, 579-585.
- Kinchesh, P., Randall, E.W. & Zick, K. 1994. Magnetic-Susceptibility Effects in Imaging - Distortion-Free Images of Plant-Tissue in Soil. *Magnetic Resonance Imaging*, **12**, 305-307.
- Kuchenbuch, R.O. & Ingram, K.T. 2002. Image analysis for non-destructive and non-invasive quantification of root growth and soil water content in rhizotrons. *Journal of Plant Nutrition and Soil Science-Zeitschrift Fur Pflanzenernahrung Und Bodenkunde*, **165**, 573-581.
- Li, Y.M., Chaney, R., Brewer, E., Roseberg, R., Angle, J.S., Baker, A., Reeves, R. & Nelkin, J. 2003. Development of a technology for commercial phytoextraction of nickel: economic and technical considerations. *Plant and Soil*, **249**, 107-115.
- Majdi, H. 1996. Root sampling methods - Applications and limitations of the minirhizotron technique. *Plant and Soil*, **185**, 255-258.
- Menon, M., Robinson, B., Oswald, S.E., Kaestner, A., Abbaspour, K.C., Lehmann, E. & Schulin, R. 2007. Visualization of root growth in heterogeneously contaminated soil using neutron radiography. *European Journal of Soil Science*, **58**, 802-810.

- Moran, C.J., Pierret, A. & Stevenson, A.W. 2000. X-ray absorption and phase contrast imaging to study the interplay between plant roots and soil structure. *Plant and Soil*, **223**, 99-115.
- Morrey, D.R., Balkwill, K., Balkwill, M.J. & Williamson, S. 1992. A review of some studies of the serpentine flora of Southern Africa. In: *The Vegetation of ultramafic (serpentine) soils*, A.J.M. Baker, J. Procter and R.D. Reeves (eds.), pp. 147–158. Intercept. Andover.
- Naftel, S.J., Martin, R.R., Sham, T.K., Macfie, S.M. & Jones, K.W. 2001. Micro-synchrotron X-ray fluorescence of cadmium-challenged corn roots. *Journal of Electron Spectroscopy and Related Phenomena*, **119**, 235-239.
- Nakanishi, T.M., Okuni, Y., Hayashi, Y. & Nishiyama, H. 2005. Water gradient profiles at bean plant roots determined by neutron beam analysis. *Journal of Radioanalytical and Nuclear Chemistry*, **264**, 313-317.
- Osuga, T. & Han, S. 2004. Proton magnetic resonance imaging of diffusion of high- and low molecular-weight contrast agents in opaque porous media saturated with water. *Magnetic Resonance Imaging*, **22**, 1039-1042.
- Pierret, A., Doussan, C., Garrigues, E. & Mc Kirby, J. 2003. Observing plant roots in their environment: current imaging options and specific contribution of two-dimensional approaches. *Agronomie*, **23**, 471-479.
- Polatajko, A., Azzolini, M., Feldmann, I., Stuezel, T. & Jakubowski, N. 2007. Laser ablation-ICP-MS assay development for detecting Cd- and Zn-binding proteins in Cd-exposed *Spinacia oleracea* L. *Journal of Analytical Atomic Spectrometry*, **22**, 878-887.
- Prohaska, T., Stadlbauer, C., Wimmer, R., Stingeder, G., Latkoczy, C., Hoffmann, E. & Stephanowitz, H. 1998. Investigation of element variability in tree rings of young Norway spruce by laser-ablation-ICPMS. *Science of the Total Environment*, **219**, 29-39.
- Przybylowicz, W.J., Mesjasz-Przybylowicz, J., Pineda, C.A., Churms, C.L., Ryan, C.G., Prozesky, V.M., Frei, R., Slabbert, J.P., Padayachee, J. & Reimold, W.U. 2001. Elemental mapping using proton-induced x-rays. *X-Ray Spectrometry*, **30**, 156-163.
- Reeves, R.D., Baker, A.J.M., Borhidi, A. & Berzain, R. 1999. Nickel hyperaccumulation in the serpentine flora of Cuba. *Annals of Botany*, **83**, 29-38.
- Robinson, B.H., Brooks, R.R., Howes, A.W., Kirkman, J.H. & Gregg, P.E.H. 1997. The potential of the high-biomass nickel hyperaccumulator *Berkheya coddii* for phytoremediation and phytomining. *Journal of Geochemical Exploration*, **60**, 115-126.
- Russo, R.E., Mao, X.L., Liu, H.C., Gonzalez, J. & Mao, S.S. 2002. Laser ablation in analytical chemistry - a review. *Talanta*, **57**, 425-451.

- Slavnina, T.P. 1971. Biochemical Processes in Rhizosphere of Crops. *Soviet Soil Science-Ussr*, **3**, 50.
- Stapf, S. & Song-I, H. (eds.) 2006. *NMR imaging in chemical engineering.*, Vol. Wiley-VCH, Weinheim, Germany.
- Starkey, R.L. 1958. Interrelations between Microorganisms and Plant Roots in the Rhizosphere. *Bacteriological Reviews*, **22**, 154-172.
- Tollner, E.W., Verma, B.P., Malko, J.A., Shuman, L.M. & Cheshire, J.M. 1991. Effect of Soil Total Iron on Magnetic-Resonance Image Quality. *Communications in Soil Science and Plant Analysis*, **22**, 1941-1948.
- Ulrich, A., Barrelet, T. & Krahenbuhl, U. 2007. Spatially resolved plant physiological analysis using LA-HR-ICP-MS. *Chimia*, **61**, 111-111.
- Van As, H. & van Dusschoten, D. 1997. NMR methods for imaging of transport processes in micro-porous systems. *Geoderma*, **80**, 389-403.
- Wenzel, W.W. 2005. Rhizosphere Conference. *Journal of Environmental Quality*, **34**, 2156-2156.
- Wenzel, W.W., Wieshammer, G., Fitz, W.J. & Puschenreiter, M. 2001. Novel rhizobox design to assess rhizosphere characteristics at high spatial resolution. *Plant and Soil*, **237**, 37-45.
- Willatt, S.T. & Struss, R.G. 1979. Germination and Early Growth of Plants Studied Using Neutron Radiography. *Annals of Botany*, **43**, 415-&.
- Willatt, S.T., Struss, R.G. & Taylor, H.M. 1978. Insitu Root Studies Using Neutron Radiography. *Agronomy Journal*, **70**, 581-586.
- Youssef, R.A. & Chino, M. 1988. Development of a New Rhizobox System to Study the Nutrient Status in the Rhizosphere. *Soil Science and Plant Nutrition*, **34**, 461-465.



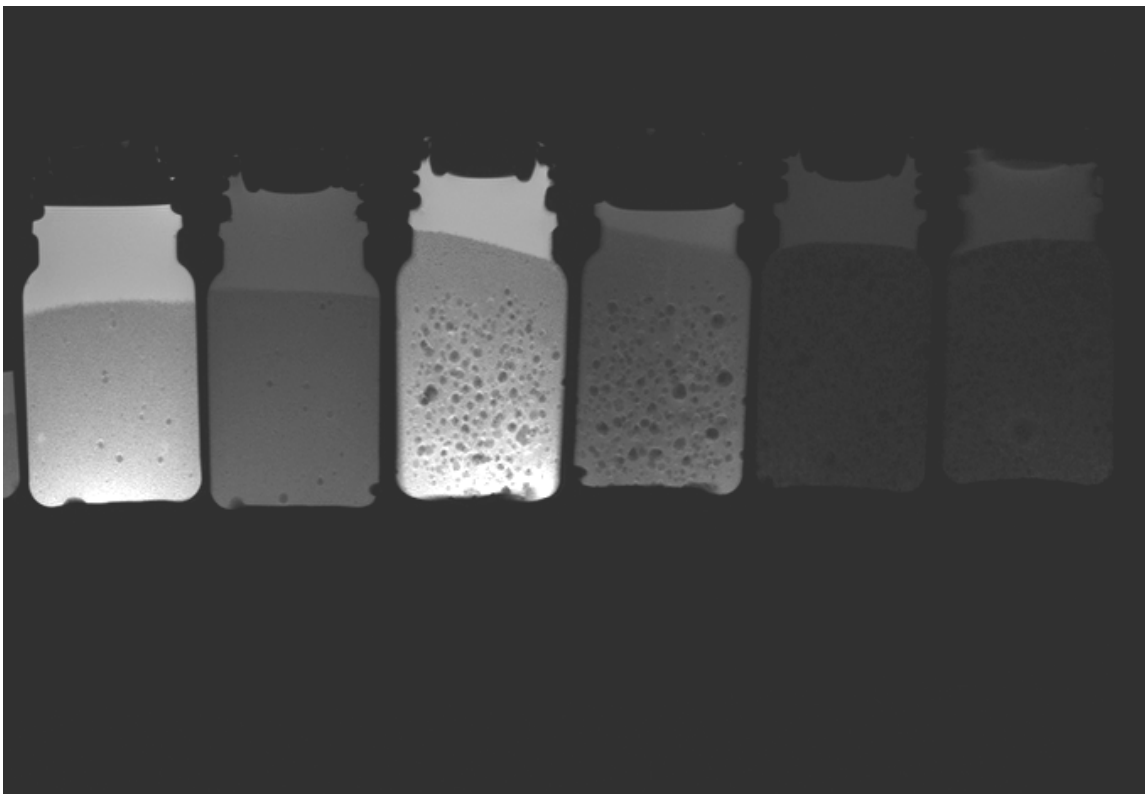
---

## 2 Magnetic resonance imaging methods to reveal the real-time distribution of nickel in porous media

---

*A. B. Moradi, S.E. Oswald, J. A. Massner, K. P. Pruessmann, B. H. Robinson, and R. Schulin*

*European Journal of Soil Science (2008), 59(3): 476-485*



## 2.1 Abstract

Direct and non-destructive measurement of the sorption, diffusion, and mobility of ions and molecules in porous media has applications in industry and environmental science. We used Magnetic Resonance Imaging (MRI) to visualize the dynamic distribution of paramagnetic nickel ( $\text{Ni}^{2+}$ ) ions in porous media. Various MRI sequences were tested to image  $\text{Ni}^{2+}$  at small concentrations. Noisy gradient echo images had poor contrast between samples containing various  $\text{Ni}^{2+}$  concentrations. Turbo spin echo and spoiled gradient echo images showed a linear relation between  $\text{Ni}^{2+}$  concentrations and signal intensity over a wide range of concentrations. Spoiled gradient echo images resolved  $\text{Ni}^{2+}$  concentrations (down to 30  $\text{mg litre}^{-1}$ ) better than turbo spin echo images. However, for smaller concentrations, the uncertainty in intensity values increased. A  $T_1$  measurement, obtained using an inversion recovery sequence, showed a linear correlation between  $T_1$  and  $\text{Ni}^{2+}$  concentration down to 1.5  $\text{mg litre}^{-1}$ . Using an ion exchange resin as a Ni sink in a glass bead medium, we imaged the real-time development of  $\text{Ni}^{2+}$  depletion zone adjacent to the resin, as Ni sorption lead to a diffusion gradient. A spatial resolution of 0.58 mm and a temporal resolution of less than a minute were achieved using  $T_1$  mapping. The two-dimensional  $\text{Ni}^{2+}$  gradient that was determined from MRI agreed well with geochemical modelling results. The results of this study showed that MRI, in particular  $T_1$  mapping, can be used to quantify the micro-scale behaviour of dissolved paramagnetic compounds in porous media. However, ferromagnetic components that naturally occur in most soils can easily disturb the MRI signal.

**Key words:** concentration gradient, magnetic resonance imaging, nickel, porous media, T1 measurement

## 2.2 Introduction

There is a growing need for the direct, non-destructive and non-invasive measurements of retention and transport processes of dissolved molecules and ions in porous materials such as soils, aquifers, bioreactors, biofilm systems, plants, and food products. Traditional methods based on the extraction of solution samples are for many purposes too invasive, tedious, expensive, and insufficient with respect to spatial and temporal resolution.

Recently developed non-destructive approaches include nuclear magnetic resonance imaging (Fischer & Hall, 1996; Herrmann *et al.*, 2002; Pierret *et al.*, 2003; Osuga & Han, 2004), neutron radiography and tomography (Nakanishi *et al.*, 2005; Hassanein *et al.*, 2006), X-ray imaging and tomography (Moran *et al.*, 2000; Naftel *et al.*, 2001; Nakashima *et al.*, 2004), and scanning electron microscopy (Birchem *et al.*, 1981).

Among the new approaches, much research has focused on using Magnetic Resonance Imaging (MRI) to investigate processes in porous media (Brown *et al.*, 1990; Macfall *et al.*, 1991; Randall *et al.*, 1997; Heyes & Clark, 2003). Magnetic Resonance Imaging provides information on the spatial distribution of water and dissolved ions, and on transport processes (see, for a review, Stapf & Song-I, 2006). Magnetic Resonance Imaging usually measures  $^1\text{H}$ , present in water molecules distributed throughout a heterogeneous medium. An important advantage of MRI over other non-destructive methods is its potential for the simultaneous determination of structure and transport processes in real time (Van As & van Dusschoten, 1997). MRI is an effective tool for the detailed study of chemical and physical processes in soil and other porous systems, but also suffers from several limitations. MRI is sensitive to paramagnetic and ferromagnetic components that are present naturally in soil. These disturb the local magnetic field and thereby distort the local MRI imaging information (Tollner *et al.*, 1991; Kinchesh *et al.*, 1994; Hall *et al.*, 1997). Therefore, most studies use artificial, specially treated or at least carefully selected media with reduced ferromagnetic components, e.g. agar, glass beads or treated soils and sand mixtures. Another limitation of MRI is the weak sensitivity and the poor signal-to-noise ratio when the voxel size is decreased in order to gain a better spatial resolution for a given object size. One has to compromise between spatial and temporal resolution for dynamic processes. Nevertheless, MRI can reveal processes that are not too fast with a relatively great spatial resolution.

The movement and sorption of paramagnetic ions or molecules can be observed by measuring their effects on the relaxation times (longitudinal relaxation time  $T_1$  and transverse relaxation time  $T_2$ ) of protons ( $^1\text{H}$ ) in the system. A standard Spin Echo (SE) sequence provides images with moderate  $T_1$  and  $T_2$  weighting. At relatively small

concentrations of a paramagnetic species, the relaxivity,  $1/T_1$ , is proportional to the concentration of the paramagnetic compound (Van As & van Dusschoten, 1997; Herrmann *et al.*, 2002; Oswald *et al.*, 2002; Nestle *et al.*, 2003a). Therefore, in  $T_1$ -weighted images, acquired with sufficiently short repetition times, image intensity will be proportional to  $1/T_1$ , after correcting for the dependency of the image intensity on  $T_2$  changes (Pearl *et al.*, 1991; Nestle *et al.*, 2003b). Spoiled gradient echo is a  $T_1$  sensitive method with a smaller  $T_2$  weighting. It is known as  $T_1$  Fast Field Echo (T1FFE) in Philips' systems and Fast Low Angle SHot (FLASH) in Siemens' systems. Spoiled gradient echo employs a rapidly repeated RF pulse that rotates the magnetization by a small flip angle, followed by a fast readout of data (Haase *et al.*, 1986; Herrmann *et al.*, 2002; Nestle *et al.*, 2003a; Nestle *et al.*, 2003b). Highly sensitive  $T_1$ -weighting and relatively short imaging times make this method especially attractive for studies of fast transport processes in porous media.

Some studies report a linear relationship between the signal intensity in the images and paramagnetic species concentration, for example  $\text{Ni}^{2+}$  (Pearl *et al.*, 1993) or  $\text{Cu}^{2+}$  (Greiner *et al.*, 1997). However, any adjustable parameter in the MRI system can affect the signal. The conversion of signal amplitude into concentration depends on the system's hardware, software and sequence details. Therefore, the calibration is not transferable, at least quantitatively. However, the  $T_1$  relaxation time is a characteristic of the individual system, including the magnetic field, and the concentrations of paramagnetic species. Its value is independent of possible changes in the signal that the scanner software or hardware makes to give a better contrast between different tissues in the image for medical purposes. Thus, methods based on direct  $T_1$  measurement are more promising for quantitative and repeated studies than others that use images with individual relations to actual concentration values. The principal method for measuring  $T_1$  is Inversion Recovery (IR), which has been used for  $T_1$  measurement of biological tissues as well as porous media (Kutsovsky *et al.*, 1996; Jivan *et al.*, 1997). The main drawback of an IR sequence is the long acquisition time resulting from a long Repetition Time (TR) in order to avoid signal saturation. Thus, alternative methods have been developed to accurately determine  $T_1$  with a significant decrease in acquisition time compared to standard IR sequence (Fram *et al.*, 1987; Fischer *et al.*, 1995; Deoni *et al.*, 2003), thus permitting the investigation of faster processes.

We aimed to compare the suitability of various MRI methods to resolve small concentrations of paramagnetic ions and to use MRI to visualize, non-destructively, the dynamic distribution and movement of paramagnetic  $\text{Ni}^{2+}$  ions through porous media, with relatively great temporal and spatial resolution

## 2.3 Materials and methods

### 2.3.1 Materials' testing

We tested the suitability of three types of glass beads, with diameters of 1.0 – 1.5 mm, 1.5 – 2.5 mm and 0.4 – 1.0 mm, as well as three types of quartz sands, with diameters of <0.5 mm, 0.3 – 0.9 mm and 1.0 – 1.5 mm. The glass beads with the diameter of 1.0- 2.5 mm were smooth-surfaced and non-porous, while the others were rough-surfaced and porous. We also tested a loamy soil. Table 2.1 gives relevant properties of these materials. Unlike the loamy soil, the glass beads and sands contained small concentrations of paramagnetic components, such as  $\text{Fe}^{3+}$ , that cause signal distortion.

*Table 2.1: Selected properties of the materials tested using MRI.*

Sample number	Type	Particle size mm	Total porosity % by volume	Bulk density $\text{g cm}^{-3}$	Provenence
1	Non-porous glass beads	1-1.5	34	1.53	Sigmund Linder, Germany
2	Porous glass beads	1.5-2.5	65	0.5	Schott, Germany
3	Porous glass beads	0.4-1	65	0.46	Sera Werke, Germany
4	Sand	<0.5	35-45	1.4-1.6	Carlo, Switzerland
5	Sand	0.3-0.9	35-45	1.4-1.6	Carlo, Switzerland
6	Sand	1-1.5	35-45	1.4-1.6	Carlo, Switzerland
7	Loamy soil	13% clay, 39% silt, 48% sand	49	1.25	Dornach, Switzerland

Each material was filled into in a 50-ml polyethylene bottle containing either deionised water or  $300 \text{ mg litre}^{-1} \text{ Ni}^{2+}$  solution (prepared using  $\text{Ni}(\text{NO}_3)_2 \cdot 6\text{H}_2\text{O}$ ). We filled the bottles under saturated conditions to prevent the formation of air bubbles and MR images were checked for the presence of air bubbles. While packing bottles by filling the material into

water is a simple and reliable approach to minimize air bubbles (Oswald *et al.*, 2002; Nestle *et al.*, 2003b), there is a potential risk of a stratification of the material in the bottle due to different settling velocities. To avoid such a risk, the falling height was kept to a few centimetres. All the bottles were placed horizontally into the radio frequency (RF) head coil of the MR scanner and were imaged in one experiment.

### 2.3.2 Ni absorption experiment

The dynamic distribution of paramagnetic  $\text{Ni}^{2+}$  in glass bead porous media was investigated while being taken up by a layer of DGT gel (Diffusive Gradients in Thin films, DGT Research Ltd, Lancaster, UK). The DGT gel incorporates an ion-exchange resin that is separated from the solution by an ion-permeable gel. Mass transport through the gel is diffusion-controlled and thus well-defined (Davison & Zhang, 1994). Two stripes of DGT gel and resin, with dimensions of 42 x 130 x 0.7 mm, were attached to one of the vertical side walls of a plexiglas box, with a vertical gap of 16 mm from each other (Figure.2.1). Based on the results of the material-testing experiment, the box was filled gently with 0.4 – 1.0 mm porous glass beads, saturated with a  $\text{Ni}(\text{NO}_3)_2 \cdot 6\text{H}_2\text{O}$  solution at a  $\text{Ni}^{2+}$  concentration of 44.1 mg litre<sup>-1</sup> adjusted to a pH of 5.5. Since the glass beads were non-charged, we assumed that there was no chemical sorption of Ni.

The box was placed in the RF head coil of the MR scanner. Twenty minutes were needed for the deployment of the DGT resin, fixing the container in the machine, performing a survey experiment, setting the coordinate axes and adjusting the desired slices in the MRI images. Then the first measurement was carried out (at  $t = 20$  minutes) and measurements continued in regular intervals of 15 minutes during the following 4 hours. Using Inductively Coupled Plasma Optical Emission Spectrometry (ICP-OES), we measured the  $\text{Ni}^{2+}$  concentration of the solution, before the imaging started, and after the experiment we also measured the  $\text{Ni}^{2+}$  content of the DGT resin.

### 2.3.3 MRI techniques and data analysis

MRI experiments were performed on a Philips Intera whole-body system (Philips medical systems, Best, the Netherlands) with a static magnetic field of 1.5 Tesla that resulted in a proton resonance frequency of 63.8 MHz. The following three MRI methods were applied and evaluated during materials testing; Turbo Spin Echo (TSE), Gradient echo (GE; also called Fast Field Echo on Philips systems), and spoiled gradient echo (T1FFE).

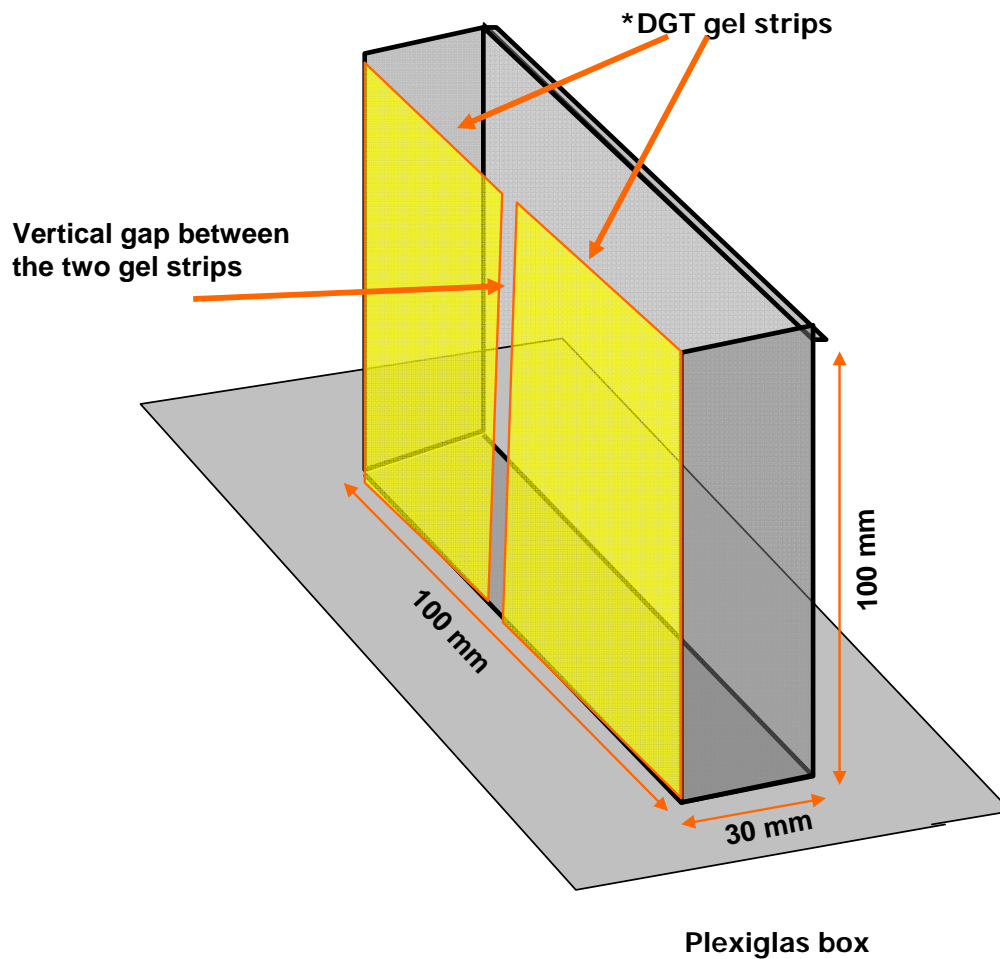


Figure 2.1: Setup of the uptake experiment; the 100 x 130 mm DGT layer was placed vertically attached to the wall of the 100 x 30 x 100 mm box and the box was filled with 0.4 – 1.0 mm porous glass beads saturated with 44.1 mg litre<sup>-1</sup> of Ni<sup>2+</sup> solution.

For the TSE images we used a slice thickness of 3 mm and a data matrix of 256 x 256 pixels. Unless otherwise stated, the repetition time was 1000 ms, the echo time ( $TE$ ) was 17 ms, the turbo factor was 10, and the flip angle was 90°. GE images were obtained using a flip angle of 10°, a repetition time of 105 ms, echo time of 2.2 ms, and the same data matrix and slice thickness as the TSE. For the T1FFE images, the flip angle was 20°, the  $TR$  was 15 ms, the  $TE$  was 5.29 ms, the turbo factor was 42, the slice thickness was 7 mm, and the data matrix was 256 x 256 pixels.

In addition two more methods were applied in the  $T_1$  mapping experiment; an Inversion Recovery (IR) sequence and a variable flip angle sequence. In the first step, IR-TSE was used to measure the  $T_1$  relaxation time in bottles filled with glass beads in the

presence of various  $\text{Ni}^{2+}$  concentrations (cf. Figure 2.5). The signal in the inversion recovery sequence was calculated based on Equation 1 (Bernstein *et al.*, 2004):

$$M(TI) = M_0[1 - 2\exp(-TI/T_1)] \quad , \quad (1)$$

where  $M$  is magnetization,  $TI$  is inversion time,  $T_1$  is longitudinal relaxation time, and  $M_0$  is equilibrium magnetization. Inversion times of 50, 150, 300, 500, 1000, 1500, and 3000 ms were used while keeping other parameters identical, to produce a series of images from the same bottles.  $T_1$  was calculated by plotting the pixel intensity as a function of  $TI$ . The  $TR$  was set to 8000 ms to avoid any signal saturation, effective  $TE$  was 60 ms, and the turbo factor was 17. For a 256 x 256 data matrix, the scan duration was 136 seconds per image. With a Field of View of 120 x 120 mm, this resulted in an in-plane spatial resolution of 0.47 x 0.47 mm.

Although inversion recovery and saturation recovery are the main methods for  $T_1$  mapping, they are handicapped by a long acquisition time. To overcome this limitation in the absorption experiment, with the particular aim of a time-resolved mapping of the changing nickel distribution, we used a method known as the variable flip angle method or variable nutation angle method (Fram *et al.*, 1987; Deoni *et al.*, 2003). This method calculates  $T_1$  with an accuracy similar to that achieved by the inversion recovery and saturation recovery techniques, but with a significantly shorter acquisition time (Deoni *et al.*, 2003). In this method, the steady state signal achieved for a sequence using phase alternated RF pulses can be calculated using Equation 2:

$$\frac{I(\theta)}{\sin(\theta)} = \exp(-TR/T_1) \frac{I(\theta)}{\tan(\theta)} + N(H)(1 - \exp(-TR/T_1))\exp(-TE/T_2^*), \quad (2)$$

where  $I$  is the signal intensity,  $N(H)$  is the proton density,  $\theta$  is the RF pulse flip angle,  $TE$  is the echo time, and  $T_2^*$  is the effective transverse relaxation time. According to Equation 2, a plot of  $I(\theta)/\sin(\theta)$  vs.  $I(\theta)/\tan(\theta)$  should yield a straight line with slope  $\exp(-TR/T_1)$ . Since this slope depends only on  $TR$ , the known repetition time, one can calculate  $T_1$  without prior knowledge of  $N(H)$  or  $T_2^*$ . We used a  $TE$  of 4.5 and  $TR$  of 9 ms.

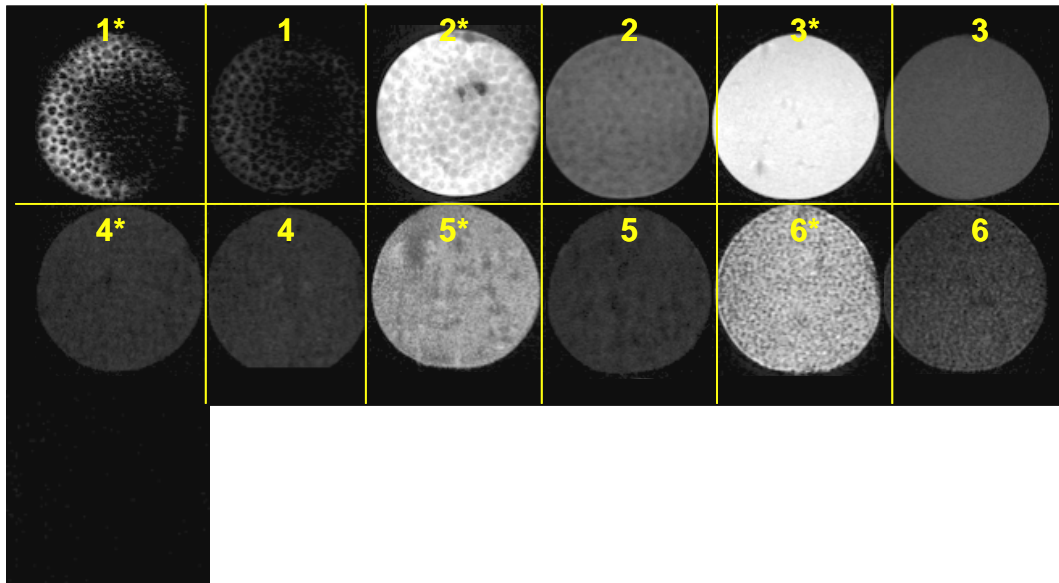
### 2.3.4 Modelling

Model simulations were carried out using the numerical code MIN3P (Mayer *et al.*, 2002), which simulates flow, transport and geochemical reactions in three-dimensional porous media. Recently, it has been used successfully to reproduce an analytical solution describing uptake of dissolved ions by a single root as well as the resulting concentration distribution around the root (Nowack *et al.*, 2006). Here, we used MIN3P to calculate the  $\text{Ni}^{2+}$  concentration distribution resulting from the uptake by the DGT resin in the three-dimensional mode. The uptake was modelled as an irreversible, fast process removing dissolved  $\text{Ni}^{2+}$  ions at the resin/gel boundary. The effective  $\text{Ni}^{2+}$  diffusion coefficient in the model was fitted to simulate the observed  $\text{Ni}^{2+}$  depletion. The other parameters were taken directly from the experiments. The total porosity of the glass beads was 65% by volume; the horizontal gap between the resin strips was 16 mm; and the initial  $\text{Ni}^{2+}$  concentration was  $44.1 \text{ mg litre}^{-1}$ . The grid resolution was set to correspond with the spatial resolution of the MRI. A grid refinement was applied in direct vicinity of the resin and in the gap area between the two resin strips, where the  $\text{Ni}^{2+}$  gradients exhibited a 2-D character.

## 2.4 Results and discussion

### 2.4.1 Testing porous materials by Turbo Spin Echo MRI

Figure 2.2 shows a turbo spin echo image of horizontal cross sections of a set of bottles filled with various sands, glass beads and a loamy soil. For all samples except the soil and the  $<0.5 \text{ mm}$  sand, there is a clear contrast between deionised water and  $300 \text{ mg litre}^{-1} \text{ Ni}^{2+}$  solution. The lack of contrast in the soil and sand may have been due to presence of paramagnetic or ferromagnetic impurities in the material. Ferromagnetic particles disturb the local magnetic field and thereby distort the MR images. Paramagnetic impurities shorten the proton relaxation times, which leads to loss of signal (Kinchesh *et al.*, 1994; Hall *et al.*, 1997; Nestle *et al.*, 2003a). This may explain why the loamy soil exhibited a complete loss of MRI signal. Among the materials tested here, the  $0.4 - 1.0 \text{ mm}$  porous glass beads gave the strongest signal in both deionised water and bottles with  $300 \text{ mg litre}^{-1} \text{ Ni}^{2+}$ . They also provided the strongest contrast between the two. Apart from being more homogeneous, the total porosity of these glass beads was 65%, as compared to 35% in non-porous glass beads, resulting in almost a doubling of the proton spin density and therefore a stronger signal. These findings were supported by measurements with other sequences, such as gradient echo (data not shown).



\* saturated with 300 mg litre<sup>-1</sup> Ni<sup>2+</sup> solution

Figure 2.2: Turbo spin echo image (1024 x 1024 pixels, TE = 40 ms, TR = 272.57 ms, turbo factor of 7) of horizontal cross sections of a set of bottles filled with different sands, glass beads and soil (material properties are listed in Table 2.1) saturated with deionised water or 300 mg litre<sup>-1</sup> Ni<sup>2+</sup> solution (indicated with stars). Porous glass beads with diameter of 0.4 – 1.0 mm gave the strongest signal and had the greatest contrast between deionised water and 300 mg litre<sup>-1</sup> Ni<sup>2+</sup> solution.

Air bubbles disturbed the local signal in preliminary experiment (data not shown), because of the sudden change in magnetic susceptibility among air-water interface, and thus caused signal loss. But filling the bottles under fully saturated conditions minimized the formation of air bubbles and the MRI images showed no evidence of any stratification.

#### 2.4.2 Testing the suitability of different MRI methods

Figure 2.3 shows images obtained by various imaging sequences from a set of bottles filled with 0.4 – 1.0 mm porous glass beads and saturated with a range of Ni<sup>2+</sup> concentrations. The brighter regions correspond to greater Ni<sup>2+</sup> concentrations. The turbo spin echo image (Figure 2.3A) reveals a clear contrast between bottles with 300, 150, and 75 mg litre<sup>-1</sup> Ni<sup>2+</sup>, yet hardly resolved 30 mg litre<sup>-1</sup> Ni<sup>2+</sup> from the background level. However, by collecting the signal from a number of acquisitions, it was possible to resolve weaker concentrations, although the standard error was large. Figure 2.3B shows an image of the same set of bottles obtained using gradient echo sequence. Unlike in the turbo spin echo sequence, a weak and

noisy contrast between bottles containing different  $\text{Ni}^{2+}$  concentrations, down to  $75 \text{ mg litre}^{-1}$   $\text{Ni}^{2+}$ , was obtained with this method. The benefit of the gradient echo sequence over turbo spin echo measurements is the shorter imaging time, because smaller flip angles, shorter echo times and shorter repetition times were used. But unlike the turbo spin echo sequence, gradient echo acquisition does not cancel field inhomogeneities, which act like a static, nonlinear gradient that dephases the water magnetization.

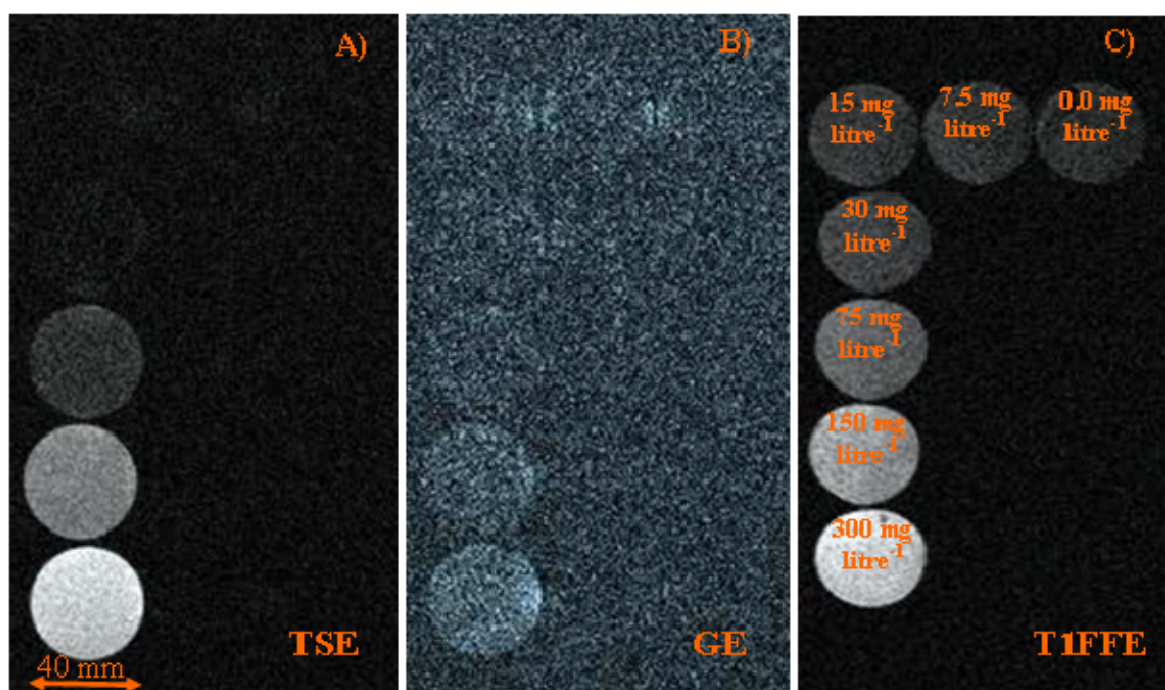


Figure 2.3: Turbo spin echo image (TSE) (A), gradient echo image (GE) (B), and spoiled gradient echo image (T1FFE) (C) of a set of bottles filled with porous glass beads,  $0.4 - 1.0 \text{ mm}$ , saturated in various concentrations of  $\text{Ni}^{2+}$ . While all three imaging protocols show a clearly enhanced signal intensity for the Ni-containing bottles compared to the de-ionized water, the signal intensity in the spoiled gradient echo image allows a much better differentiation of  $\text{Ni}^{2+}$  concentrations, especially for the smaller concentration range.

The best contrast was obtained with a spoiled gradient echo sequence, called T1FFE (Figure 2.3C). Unlike the turbo spin echo sequence, in which the signal intensity depends on both  $T_1$  and  $T_2$  relaxation times, the spoiled gradient echo sequence provided strongly  $T_1$ -weighted images of the samples when a short echo time was used. For both T1FFE and TSE, the signal increased with increasing  $\text{Ni}^{2+}$  concentrations.

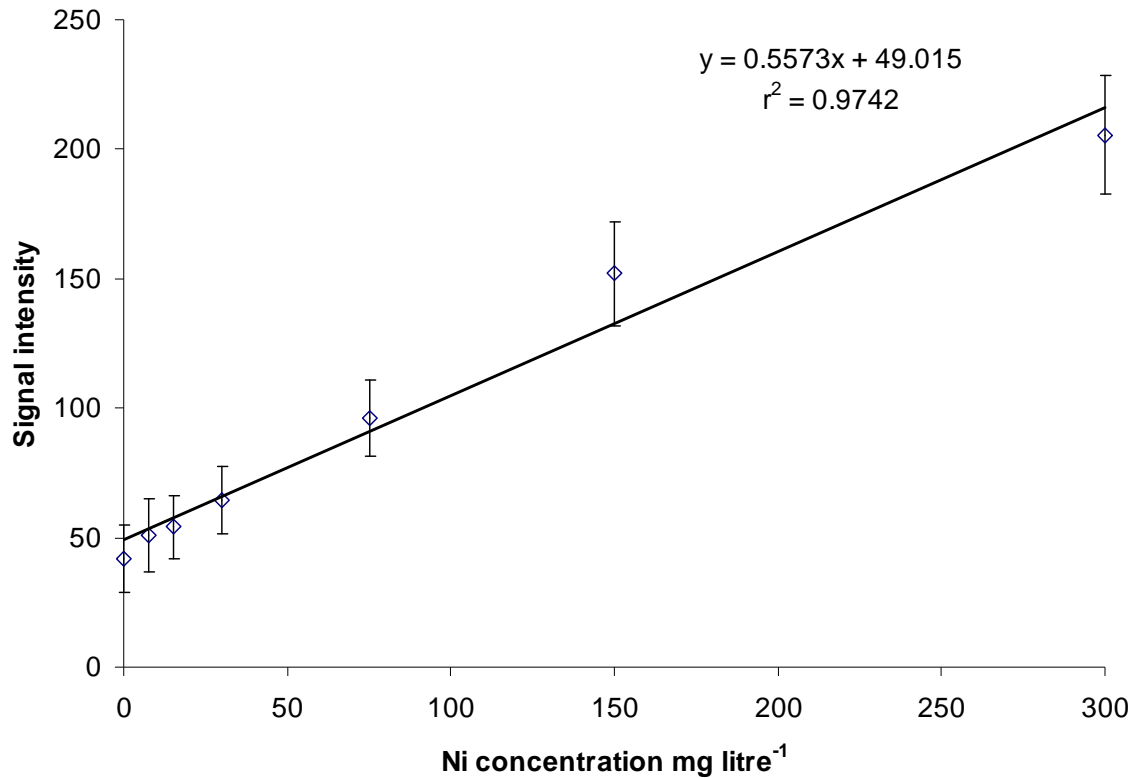


Figure 2.4: The calibration of signal intensity, obtained by spoiled gradient echo imaging, versus various  $\text{Ni}^{2+}$  concentration in 50 ml bottles containing porous glass beads (0.4 – 1.0 mm); bars represent standard deviations.

Figure 2.4 shows a correlation between the  $\text{Ni}^{2+}$  concentrations and the signal intensity obtained from T1FFE images. The data points show the mean value of the signal intensity obtained over the bottle cross-sections and error bars represent the standard deviation from the mean. The linearity was maintained over the whole concentration range studied, but the measurement contained a relatively large uncertainty. As is often the case, the relative error was larger at smaller concentrations. The advantageous of the T1FFE method was its great speed, allowing for qualitative investigations. Thus, the T1FFE method is suited for investigations where the concentrations are high and changes rather quick, but less for situations where concentrations are low and concentration differences small.

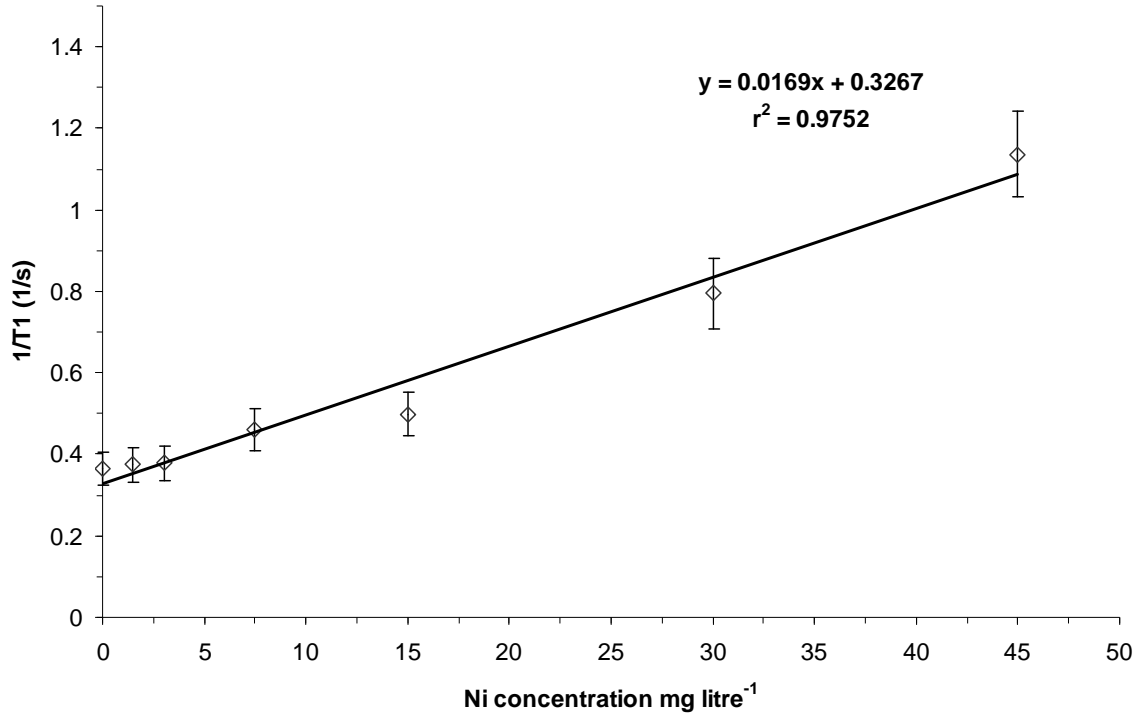


Figure. 2.5: Calculated  $1/T_1$  values from signals obtained by inversion recovery sequence for a range of  $\text{Ni}^{2+}$  concentrations in 50 ml bottles containing porous glass beads (0.4 – 1.0 mm);  $T_1$  values are averaged over the vertical cross section of the bottle and the bars represent the inter-pixel standard deviations.

For the latter case, the inversion recovery sequence (Equation 1) is much better suited than the T1FFE method. It is slower, but considerably more accurate and precise than the spoiled gradient echo method. The low uncertainty of this method not only refers to smaller standard deviations of the measurement, but also indicates that the particular  $T_1$  value is a characteristic of the system and dependent on the specific method, instrument, and measurement conditions. Regression analysis revealed a linear relation between the longitudinal relaxivity  $1/T_1$  and  $\text{Ni}^{2+}$  concentration in the range of 1 to 45 mg litre<sup>-1</sup>  $\text{Ni}^{2+}$  (Figure 2.5). Such high Ni concentrations are not unrealistic for contaminated soils with vegetation (Brooks, 1998).

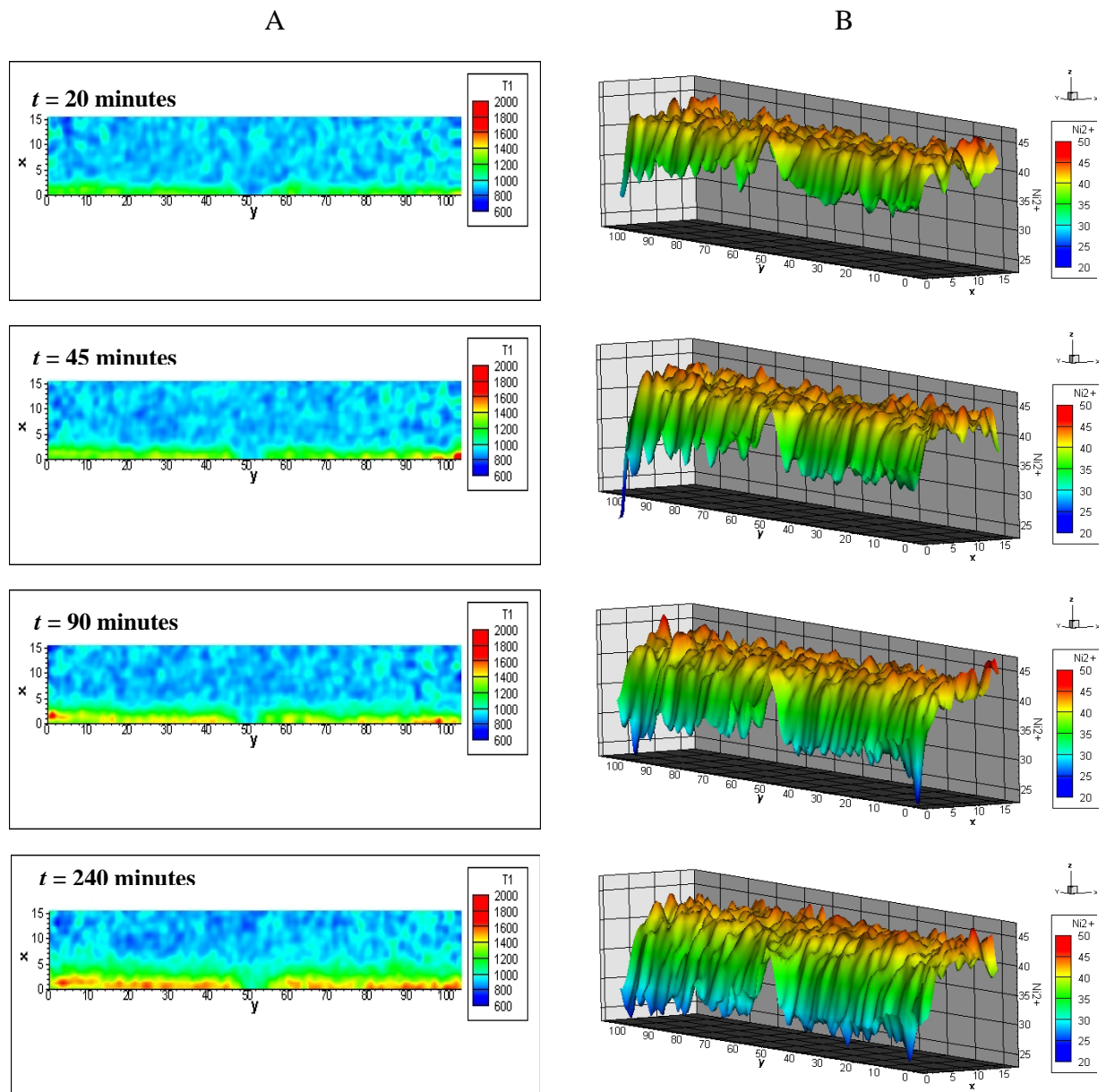


Figure 2.6: Time sequence of  $Ni^{2+}$  distribution induced by uptake of  $Ni^{2+}$  by the DGT resin, for times  $t = 20, 45, 90$  and  $240$  minutes (top to bottom); plotted values were smoothed to reduce the influence of noise. A)  $T_1$  maps ( $T_1$  unit is ms) obtained from the MRI experiment (x-axis shows distance from the DGT resin surface while the two resins are mounted along the y-axis with a gap of 16 mm). B) Inferred  $Ni^{2+}$  concentration distributions displayed as 2D surface colour plots, with the uptake resin be located exactly on the y-axis; x and y correspond to distance in mm and  $Ni^{2+}$  concentration unit is mg litre<sup>-1</sup>.

### 2.4.3 The absorption experiment

For the time-resolved imaging of the Ni absorption by the DGT resin, we needed a method that was much faster than inversion recovery. The later requires a long repetition time (8000 ms in our case) to prevent any signal saturation. Therefore, the variable flip angle method was used for  $T_1$  mapping of the system. This allowed monitoring the development of the  $\text{Ni}^{2+}$  gradient near the DGT gel surface in real-time. Six slices were obtained with a data matrix of 208 x 208 pixels. The slice thickness was 15 mm and the spatial in-plane resolution was calculated to be 0.58 x 0.58 mm<sup>2</sup>. The spatial and temporal change of the  $T_1$  values in the 5th slice is shown in Figure 2.6A. The  $T_1$  value was  $900.2 \pm 26.5$  ms for the background level and increased towards the gel surface, thus showing a depletion zone that increased over time in size and strength. Figure 2.6B shows the  $\text{Ni}^{2+}$  concentration calculated pixel by pixel from the corresponding  $T_1$  values by mean of the calibration curve shown in Figure 2.5. The background  $\text{Ni}^{2+}$  level corresponds to a  $\text{Ni}^{2+}$  concentration of  $42.3 \pm 0.4$  mg litre<sup>-1</sup>, which is only slightly smaller than the measured initial concentration (44.1 mg litre<sup>-1</sup>). The deviation falls inside the error margins of the  $1/T_1$  curve for large  $\text{Ni}^{2+}$  concentrations, in agreement with the assumption that Ni sorption by the glass beads was insignificant. The saw-edge shape in the plot might derive from local unsteadiness of the gel surface in vertical or horizontal directions. Since the gel had a great affinity for  $\text{Ni}^{2+}$  ions, 20 minutes was sufficient to create a depletion zone up to 1.7 mm from the gel surface. Four hours after the gel deployment, the depletion zone had broadened to 7.5 mm from the gel interface. The 16-mm gap between the two layers of the gel clearly appears in both the  $T_1$  and  $\text{Ni}^{2+}$  concentration plots (Figure 2.6A and B). The signal was obtained from voxels with dimensions of 0.58 x 0.58 x 15 mm. Considering the size of the glass beads (0.4 – 1.0 mm), beads with a diameter larger than 0.58 mm may lie inside or outside a voxel; however, a slice thickness of 15 mm in the vertical direction gives a signal that is composed of a random proportion of beads and pore water. The total amount of  $\text{Ni}^{2+}$  sorbed by the DGT resin was 23.6% greater than the  $\text{Ni}^{2+}$  deficit in the depletion zone calculated by integrating over the  $\text{Ni}^{2+}$  concentration.

The first slice was located above the glass bead surface within a large bulk of  $\text{Ni}^{2+}$  solution. Since the uptake was diffusion-limited and diffusion in free solution is faster than in a porous medium, the depletion zone in the first slice did not extend as far as in the other slices. Apart from the first slice, there were no significant differences between slices. Figure 2.7A shows the averaged  $\text{Ni}^{2+}$  distribution of slices 2-6. The two-dimensional nature of the  $\text{Ni}^{2+}$  distribution around the gap area is clearly visible, while the isolines away from the gap are nearly parallel to the gel surface, indicating a homogeneous depletion of  $\text{Ni}^{2+}$  along the

gel surface. Figure 2.7B shows the corresponding  $\text{Ni}^{2+}$  distribution simulated by means of the MIN3P model. The good agreement between the simulated and experimentally determined  $\text{Ni}^{2+}$  distribution shows the capability of the MRI method to determine the spatial distribution of Ni cations in the solution of porous media with a resolution sufficient to resolve local gradient over mm distances. The effective diffusion coefficient was calculated by MIN3P to be  $0.3 \times 10^{-9} \text{ m}^2 \text{ s}^{-1}$ , which is a reasonable value considering the tortuosity of the pore space and that the  $\text{Ni}^{2+}$  diffusion coefficient in free aqueous solution is  $1.25 \times 10^{-9} \text{ m}^2 \text{ s}^{-1}$ .

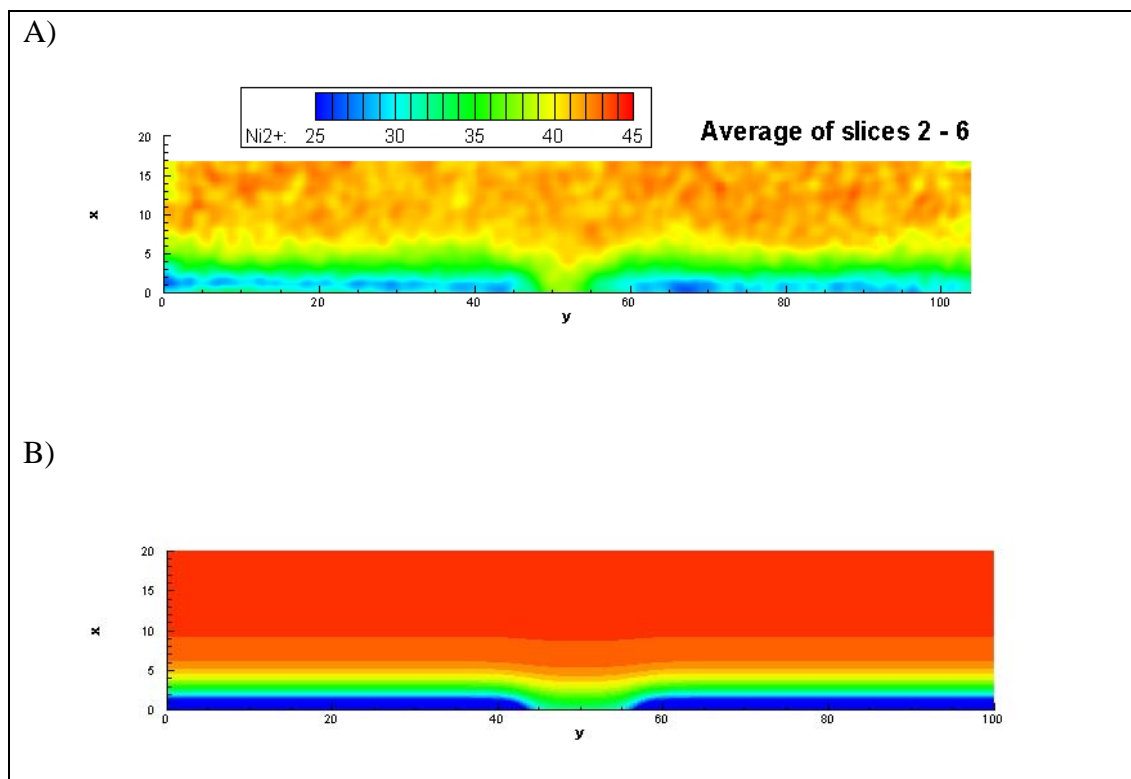


Figure 2.7: Averaged  $\text{Ni}^{2+}$  distribution (mean value of original slices 2-6) four hours after uptake of  $\text{Ni}^{2+}$  by DGT resin started: A) measured by MRI and B) simulated using model MIN3P;  $x$  and  $y$  show distance in mm and  $\text{Ni}^{2+}$  concentration unit is  $\text{mg litre}^{-1}$ .

## 2.5 Conclusions and applications

- 1) The presence of some ferromagnetic impurities and air bubbles limits to the application of MRI to soil.

- 2) Moderate  $T_1$  and  $T_2$ -weighted TSE images and strongly  $T_1$ -weighted spoiled gradient echo images of the samples resolved the distribution of paramagnetic  $\text{Ni}^{2+}$  ions down to a concentration of  $30 \text{ mg litre}^{-1}$ . The spoiled gradient echo images showed a better contrast.
- 3) For concentrations below  $30 \text{ mg litre}^{-1}$   $\text{Ni}^{2+}$ ,  $T_1$  was precisely measured with the sensitive IR sequence. As  $1/T_1$  was linearly correlated with the  $\text{Ni}^{2+}$  concentrations. In the pore water, we recommend  $T_1$  mapping for imaging paramagnetic species in porous media at environmentally relevant concentration ranges.
- 4) The dynamic distribution of paramagnetic ions can be measured with relatively great temporal resolution, less than a minute in our case, using fast  $T_1$  mapping methods, such as the variable flip angle method.
- 5) The resolution of the MRI images was sufficient to monitor development of concentration gradients on a spatial scale of less than 1 mm and a time scale of less than a minute. Such information is suitable for comparison with two- or three-dimensional numerical simulations.
- 6) These results suggest that processes such as diffusion, sorption and desorption, uptake by plant roots, and transport of paramagnetic compounds in the environment could potentially be studied in detail using MRI.

## 2.6 Acknowledgements

This study was funded by the Swiss National Science Foundation. We would like to thank Reto Treier (IBE, ETH Zurich) for his technical support on  $T_1$  calculations.

## 2.7 References

- Bernstein, M.A., King, K.F. & Zhou, X.J. 2004. *Handbook of MRI pulse sequences*. Elsevier Academic Press.
- Birchem, R., Sommer, H.E. & Brown, C.L. 1981. Scanning Electron-Microscopy of Shoot and Root Development in Sweetgum Callus-Tissue Culture. *Forest Science*, **27**, 206-212.
- Brown, J.M., Kramer, P.J., Cofer, G.P. & Johnson, G.A. 1990. Use of Nuclear-Magnetic-Resonance Microscopy for Noninvasive Observations of Root-Soil Water Relations. *Theoretical and Applied Climatology*, **42**, 229-236.
- Davison, W. & Zhang, H. 1994. In-Situ Speciation Measurements of Trace Components in Natural-Waters Using Thin-Film Gels. *Nature*, **367**, 546-548.

- Deoni, S.C.L., Rutt, B.K. & Peters, T.M. 2003. Rapid combined T-1 and T-2 mapping using gradient recalled acquisition in the steady state. *Magnetic Resonance in Medicine*, **49**, 515-526.
- Fischer, A.E. & Hall, L.D. 1996. Visualization of the diffusion of metal ions and organic molecules by magnetic resonance imaging of water. *Magnetic Resonance Imaging*, **14**, 779-783.
- Fischer, A.E., Balcom, B.J., Fordham, E.J., Carpenter, T.A. & Hall, L.D. 1995. A Fast Inversion-Recovery Nmr Imaging Technique for Mapping 2-Dimensional Tracer Diffusion and Dispersion in Heterogeneous Media. *Journal of Physics D-Applied Physics*, **28**, 384-397.
- Fram, E.K., Herfkens, R.J., Johnson, G.A., Glover, G.H., Karis, J.P., Shimakawa, A., Perkins, T.G. & Pelc, N.J. 1987. Rapid Calculation of T1 Using Variable Flip Angle Gradient Refocused Imaging. *Magnetic Resonance Imaging*, **5**, 201-208.
- Greiner, A., Schreiber, W., Brix, G. & Kinzelbach, W. 1997. Magnetic resonance imaging of paramagnetic tracers in porous media: Quantification of flow and transport parameters. *Water Resources Research*, **33**, 1461-1473.
- Haase, A., Frahm, J., Matthaei, D., Hanicke, W. & Merboldt, K.D. 1986. Flash Imaging - Rapid Nmr Imaging Using Low Flip-Angle Pulses. *Journal of Magnetic Resonance*, **67**, 258-266.
- Hall, L.D., Amin, M.H.G., Dougherty, E., Sanda, M., Votrubova, J., Richards, K.S., Chorley, R.J. & Cislerova, M. 1997. MR properties of water in saturated soils and resulting loss of MRI signal in water content detection at 2 tesla. *Geoderma*, **80**, 431-448.
- Hassanein, R., Meyer, H.O., Carminati, A., Estermann, M., Lehmann, E. & Vontobel, P. 2006. Investigation of water imbibition in porous stone by thermal neutron radiography. *Journal of Physics D-Applied Physics*, **39**, 4284-4291.
- Herrmann, K.H., Pohlmeier, A., Wiese, S., Shah, N.J., Nitzsche, O. & Vereecken, H. 2002. Three-dimensional nickel ion transport through porous media using magnetic resonance Imaging. *Journal of Environmental Quality*, **31**, 506-514.
- Heyes, J.A. & Clark, C.J. 2003. Magnetic resonance imaging of water movement through asparagus. *Functional Plant Biology*, **30**, 1089-1095.
- Jivan, A., Horsfield, M.A., Moody, A.R. & Cherryman, G.R. 1997. Dynamic T-1 measurement using snapshot-FLASH MRI. *Journal of Magnetic Resonance*, **127**, 65-72.
- Kinchesh, P., Randall, E.W. & Zick, K. 1994. Magnetic-Susceptibility Effects in Imaging - Distortion-Free Images of Plant-Tissue in Soil. *Magnetic Resonance Imaging*, **12**, 305-307.

- Kutsovsky, Y.E., Alvarado, V., Davis, H.T., Scriven, L.E. & Hammer, B.E. 1996. Dispersion of paramagnetic tracers in bead packs by T-1 mapping: Experiments and simulations. *Magnetic Resonance Imaging*, **14**, 833-839.
- Macfall, J.S., Johnson, G.A. & Kramer, P.J. 1991. Comparative Water-Uptake by Roots of Different Ages in Seedlings of Loblolly-Pine (*Pinus-Taeda* L). *New Phytologist*, **119**, 551-560.
- Mayer, K.U., Frind, E.O. & Blowes, D.W. 2002. Multicomponent reactive transport modeling in variably saturated porous media using a generalized formulation for kinetically controlled reactions. *Water Resources Research*, **38**.
- Moran, C.J., Pierret, A. & Stevenson, A.W. 2000. X-ray absorption and phase contrast imaging to study the interplay between plant roots and soil structure. *Plant and Soil*, **223**, 99-115.
- Naftel, S.J., Martin, R.R., Sham, T.K., Macfie, S.M. & Jones, K.W. 2001. Micro-synchrotron X-ray fluorescence of cadmium-challenged corn roots. *Journal of Electron Spectroscopy and Related Phenomena*, **119**, 235-239.
- Nakanishi, T.M., Okuni, Y., Hayashi, Y. & Nishiyama, H. 2005. Water gradient profiles at bean plant roots determined by neutron beam analysis. *Journal of Radioanalytical and Nuclear Chemistry*, **264**, 313-317.
- Nakashima, Y., Nakano, T., Nakamura, K., Uesugi, K., Tsuchiyama, A. & Ikeda, S. 2004. Three-dimensional diffusion of non-sorbing species in porous sandstone: computer simulation based on X-ray microtomography using synchrotron. *Journal of Contaminant Hydrology*, **74**, 253-264.
- Nestle, N., Baumann, T., Wunderlich, A. & Niessner, R. 2003a. MRI observation of heavy metal transport in aquifer matrices down to sub-mg quantities. *Magnetic Resonance Imaging*, **21**, 345-349.
- Nestle, N., Wunderlich, A., Niessner, R. & Baumann, T. 2003b. Spatial and temporal observations of adsorption and remobilization of heavy metal ions in a sandy aquifer matrix using magnetic resonance imaging. *Environmental Science & Technology*, **37**, 3972-3977.
- Nowack, B., Mayer, K.U., Oswald, S.E., van Beinum, W., Appelo, C.A.J., Jacques, D., Seuntjens, P., Gerard, F., Jaillard, B., Schnepf, A. & Roose, T. 2006. Verification and intercomparison of reactive transport codes to describe root-uptake. *Plant and Soil*, **285**, 305-321.
- Osuga, T. & Han, S. 2004. Proton magnetic resonance imaging of diffusion of high- and low molecular-weight contrast agents in opaque porous media saturated with water. *Magnetic Resonance Imaging*, **22**, 1039-1042.

- Oswald, S.E., Scheidegger, M.B. & Kinzelbach, W. 2002. Time-dependent measurement of strongly density-dependent flow in a porous medium via nuclear magnetic resonance imaging. *Transport in Porous Media*, **47**, 169-193.
- Pearl, Z., Magaritz, M. & Bendel, P. 1991. Measuring Diffusion-Coefficients of Solutes in Porous-Media by Nmr Imaging. *Journal of Magnetic Resonance*, **95**, 597-602.
- Pearl, Z., Magaritz, M. & Bendel, P. 1993. Nuclear-Magnetic-Resonance Imaging of Miscible Fingering in Porous-Media. *Transport in Porous Media*, **12**, 107-123.
- Pierret, A., Doussan, C., Garrigues, E. & Mc Kirby, J. 2003. Observing plant roots in their environment: current imaging options and specific contribution of two-dimensional approaches. *Agronomie*, **23**, 471-479.
- Randall, E.W., Mahieu, N. & Ivanova, G.I. 1997. NMR studies of soil, soil organic matter and nutrients: spectroscopy and imaging. *Geoderma*, **80**, 307-325.
- Stapf, S. & Song-I, H. (eds.) 2006. *NMR imaging in chemical engineering.*, Vol. Wiley-VCH, Weinheim, Germany
- Tollner, E.W., Verma, B.P., Malko, J.A., Shuman, L.M. & Cheshire, J.M. 1991. Effect of Soil Total Iron on Magnetic-Resonance Image Quality. *Communications in Soil Science and Plant Analysis*, **22**, 1941-1948.
- Van As, H. & van Dusschoten, D. 1997. NMR methods for imaging of transport processes in micro-porous systems. *Geoderma*, **80**, 389-403.

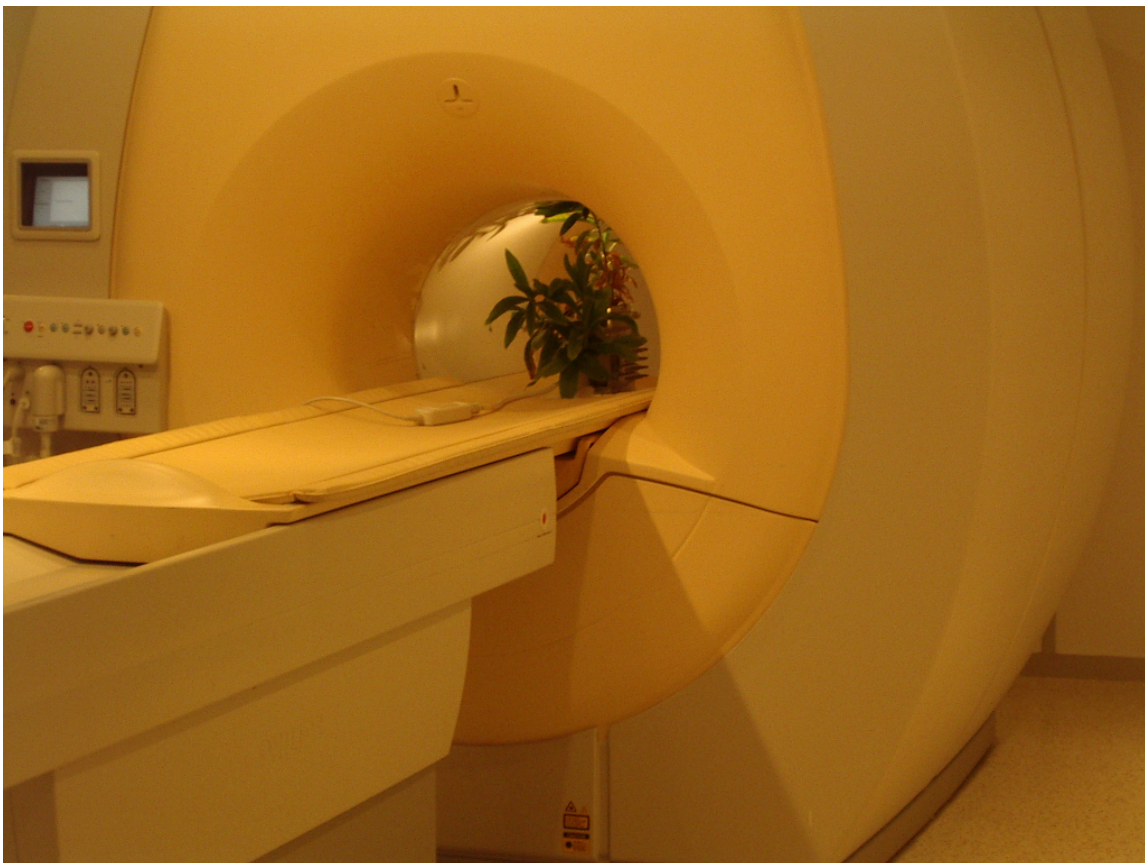
---

### **3 Analysis of nickel concentration profiles in the rhizosphere of the hyperaccumulator plant, *Berkheya coddii*, using MRI and numerical simulations**

---

*A. B. Moradi, S.E. Oswald, J. A. Massner, K. P. Pruessmann, B. H. Robinson, and R. Schulin*

*Submitted for publication in Environmental Science and Technology*



### 3.1 Abstract

Uptake of heavy metals by plant roots is a low-cost strategy to remove heavy metals from contaminated soils, but requires plant species providing high metal uptake rates. We show here how a non-destructive measurement technique can be used to investigate the uptake mechanism of the nickel hyperaccumulator plant *Berkheya coddii* in-situ, which is usually hampered by the difficult experimental accessibility of the rhizosphere. Magnetic Resonance Imaging (MRI) was applied to study the dynamics of the spatial distribution of nickel ( $\text{Ni}^{+2}$ ) in soil solution during water and solute uptake by roots. Special rhizoboxes were used in which a root monolayer had been grown, separated from an adjacent glass bead packing by a nylon membrane. After applying a  $\text{Ni}^{+2}$  solution of  $10 \text{ mg kg}^{-1}$ , the rhizobox was imaged repeatedly using MRI. The obtained temporal sequence of 2-dimensional  $\text{Ni}^{+2}$  maps in the rhizosphere showed that  $\text{Ni}^{+2}$  concentrations increased towards the root plane, revealing an exclusion pattern. Numerical modelling supported the  $\text{Ni}^{+2}$  distributions to result from advective water flow driven by transpiration and diffusion in the opposite direction tending to eliminate the concentration gradient. With the model, it could be studied how the exclusion pattern transforms into a depletion pattern depending on transpiration rates and solute uptake rates.

**Keywords:** *Berkheya coddii*, concentration gradient, hyperaccumulator, magnetic resonance imaging (MRI), modelling, nickel, uptake

### 3.2 Introduction

While rhizosphere processes were first studied with an emphasis on plant nutrients (Clark, 1949; Tan & Nopamornbodi, 1979; Cushman, 1980), the focus has recently been shifted more to the fate of soil pollutants such as heavy metals. This is a consequence of increasing awareness of soil pollution problems and the attempts to control the pollutants and to remediate contaminated soils (Wenzel, 2005). One heavy metal of concern is nickel, and soils containing high concentrations of Ni occur worldwide. Nickel in soil can be of geogenic origin, as in ultramafic (serpentine) soils (Robinson *et al.*, 1999), or may arise from anthropogenic pollution due to mining, stainless steel and alloy production (Brooks, 1998), or deposition of sewage sludge (Ashworth & Alloway, 2004; Kashem & Singh, 2007). Nickel hyperaccumulator plants growing on serpentine soils are able to accumulate  $> 1000 \text{ mg kg}^{-1}$  Ni (dry weight) in their shoots. This is at least 10 times more than other plant species growing in the same environment (Brooks *et al.*, 1977). Therefore, hyperaccumulator plants may offer a sustainable treatment option for the remediation of metal-contaminated sites, but also an opportunity to mine naturally metal-rich soils by phytomining (Brooks *et al.*, 1998; Angle *et al.*, 2001; Li *et al.*, 2003). An attractive plant for phytoextraction of Ni is *Berkheya coddii* Roessler, a perennial plant belonging to the Asteraceae family. Its extraordinary phytoextraction potential results from the combination of high biomass ( $22 \text{ t ha}^{-1}$ ), and high capacity of Ni accumulation in its above-ground biomass (up to 1% w:w) (Robinson *et al.*, 1997). Most plant species have only one of these two requirements for an efficient phytoextraction practice. Despite this, little is known about the mechanism of Ni hyperaccumulation and root-soil interactions of *Berkheya coddii* as well as of other Ni accumulator plants. Understanding these mechanisms and interactions could help improving methods for the phytoextraction of Ni from contaminated soils and also phytomining (McNear *et al.*, 2005).

However, investigating rhizosphere processes and root-soil interactions such as the uptake of nutrients and water by roots is challenging. It requires a high resolution in the analysis of the spatial distribution of solutes because these processes and interactions create substantial differences in concentrations over distances of a few millimetres from root surfaces. The three-dimensional geometry of the root systems further complicates the problem. Many rhizosphere processes are dynamic (Darrah, 1993; Gregory & Hinsinger, 1999; Wenzel *et al.*, 2001; Hinsinger *et al.*, 2006), therefore a non-destructive, non-invasive method to observe rhizosphere processes resolved in space and time is desirable.

The uptake of most of the trace metals, such as nickel, by roots, is generally considered to occur via selective passages of the free ions through more or less specific membrane

transporters (Zhao *et al.*, 2002; Whiting *et al.*, 2003). If metal uptake is slow, metals taken up by roots from soil solution can be replenished by the displacement of sorbed metals from the bulk soil towards the roots. But if a metal is removed more rapidly from the rhizosphere by root uptake than it can be re-supplied, the metal will become depleted adjacent to the root surface (Tinker & Nye, 2000). In contrast, if the mass flow of a solute exceeds the uptake rate of the solute, then even a concentration gradient opposing the advection flux will develop. The resulting concentration profiles are further influenced by chemical reactions with other compounds in the rhizosphere and with the soil matrix. Although these interactions between plant roots and solutes in rhizosphere have been discovered earlier, it has never been observed *in situ* with sufficient temporal and spatial resolution due to technical difficulties. Combining new non-destructive measurement techniques such as MRI and numerical simulations can unravel some aspects of these complex processes in the rhizosphere.

Among other new techniques, Magnetic Resonance Imaging (MRI) has recently been proposed to assess the spatial distribution of water and ions in porous media (Brown *et al.*, 1990; Oswald *et al.*, 1997; Van As & van Dusschoten, 1997; Herrmann *et al.*, 2002; Nestle *et al.*, 2003; Pierret *et al.*, 2003; Valfouskaya *et al.*, 2005; Moradi *et al.*, 2008). MRI is a non-destructive method that can be used to simultaneously analyse structures and transport processes in real time (Van As & van Dusschoten, 1997). The presence of paramagnetic ions and molecules in a solution affects the relaxation times (longitudinal relaxation time  $T_1$  and transverse relaxation time  $T_2$ ) of protons ( $^1\text{H}$ ). The determination of these relaxation times provides opportunities to trace the movement and diffusion of dissolved paramagnetic compounds and ions such as  $\text{Ni}^{2+}$  in the porous media. However, applying MRI to soil-plant system has several limitations. The presence of ferromagnetic particles and other paramagnetic compounds in soils can distort the MRI images and cause severe signal loss. Therefore, at the present state, this technique mainly is applied only to carefully selected media such as pre-treated sand and soil, agar, and glass beads.

In a previous study we tested the capability of MRI to study the temporal development of the spatial distribution of dissolved  $\text{Ni}^{2+}$  ions in a porous medium comprised of glass beads and saturated with a Ni solution under the influence of absorption by an exchange resin (Moradi *et al.*, 2008). Here we showed that MRI can detect relevant concentration profiles and thus can be used to investigate Ni uptake by hyperaccumulator plants in a more complex system. We studied the 2-dimensional spatial and temporal distribution of  $\text{Ni}^{+2}$  in the rhizosphere of hyperaccumulator plant *Berkheya coddii* grown in a rhizobox in which the roots formed a planar monolayer. We also used numerical modelling to interpret the

measurements and to analyse the dependence of the  $\text{Ni}^{+2}$  gradient adjacent to the roots on transpiration rate, uptake rate and initial concentration of  $\text{Ni}^{+2}$ .

### 3.3 Materials and Methods

#### 3.3.1 Rhizobox setup and plant growth

The rhizoboxes used in this study (Figure 3.1) were a modified version of the rhizobox system developed and tested by Wenzel et al. (2001). We changed the frame of the rhizobox so that the MRI receiver coils could be installed close to the root plane on the transparent side of the rhizobox (an acrylic window for root visualization and root growth control) to obtain maximal coil sensitivity in the volume of interest. We sealed the rhizoboxes using rubber bands and silicon glue. The experiment started from a water-saturated condition, which gave the strongest MRI signals. We also redesigned the inlet and outlet ports and increased their number to 30 per box, arranged on one side of the box in 5 rows of 6 ports each, in order to improve the regulation of the nutrient solution in the main compartment of the rhizobox.



Figure 3.1: The rhizobox set up with a view of the outlet and inlet ports (left) and the root-only compartment (right)

Seeds of *Berkhey coddii* were pre-germinated in perlite and grown until they were two weeks old. The seedlings were transferred to the upper compartment of the rhizoboxes. The main compartment of each rhizobox was filled with porous glass beads (Sera Werke, Germany) of 0.4 – 1.0 mm-diameter. The total porosity of the packing was 65% v/v, and the bulk density was 0.46 g cm<sup>-3</sup>. Four rhizoboxes were prepared in total and four seedlings were planted per rhizobox. After transplanting, the rhizoboxes were kept for 8 weeks in a climate chamber with a daily light cycle of 16 h light/ 8 h darkness, constant humidity (75%) and controlled temperature (23/16°C day/night). The rhizoboxes were irrigated with Hoagland's nutrient solution (Hoagland & Arnon, 1938). A peristaltic pump was used to circulate the nutrient solution through the rhizoboxes at a rate of around 0.6 litre per day. The lower two rows of the ports were used as inlets for the nutrient solution and the ports of the uppermost row were used as outlets. Roots started to grow into the root-only compartment a week after transplanting. The root-only compartment contained no glass beads or soil. It consisted of a narrow slit separated from the glass beads by a nylon membrane with a mesh size of 20 µm. After 8 weeks of growth the MRI experiments were performed with the rhizobox showing the most uniform root plane.

### 3.3.2 MRI technique and data analysis

MRI was performed using a Philips Intera whole-body system (Philips medical systems, Best, the Netherlands) with a static magnetic field of 1.5 Tesla that results in a proton resonance frequency of 63.8 MHz. The  $T_1$  mapping technique proposed by Deoni et al. (2003) and Treier et al. (2007) was used for the quantification of  $T_1$ . This method calculates  $T_1$  with the same accuracy but with a significantly shorter acquisition time than standard  $T_1$  measurement sequences. We used an echo time of 4.5, a repetition time of 9 ms, slice thickness of 15 mm, and a data matrix of 512 x 512 pixels. Due to the limited spatial sensitivity of the receiver coil, the signal-to-noise ratio deteriorated with distance from the coil centre. This was especially pronounced in the corners and the rhizobox walls opposite to the root plane. Therefore we excluded a margin of 5 mm width from the images for further analysis. A median filter with dimensions of 3 x 3 pixels was applied to the  $T_1$  images to reduce noise. All the images were processed using Matlab. In the previous study without plants (Moradi *et al.*, 2008), we found a linear relationship between the longitudinal relaxivity,  $1/T_1$ , and the Ni<sup>+2</sup> concentrations in solution in the range of 1 – 45 mg l<sup>-1</sup> (Figure 3.2). Here, we used the same calibration curve for calculating Ni concentrations from  $T_1$  values.

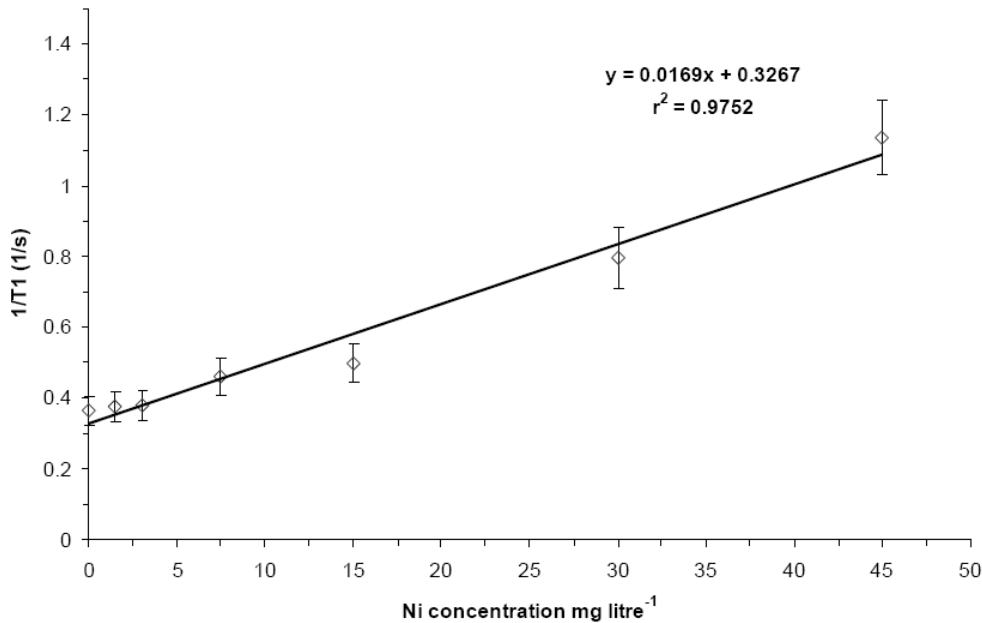


Figure 3.2: The calibration of  $1/T_1$  versus Ni concentration; bars represent standard deviations (after Moradi *et al.* 2008)

### 3.3.3 Ni uptake experiment

For the Ni uptake experiment, the main compartment of the rhizobox was washed with eight pore-volumes of  $\text{Ni}^{+2}$  solution with a concentration of 10 mg Litre<sup>-1</sup> to replace the Hoagland nutrient solution. We used the lower ports as inlets for ingoing Ni solution and let the solution overflow over the lateral walls of the rhizobox to ensure homogeneous initial Ni distribution in the system. This rather high concentration of Ni was used to stay clearly above the detection limit for  $\text{Ni}^{2+}$  of 1 mg litre<sup>-1</sup>. Although Ni concentrations are usually much lower in soils, such high Ni concentrations were found to occur in ultramafic soils where Ni hyperaccumulator plants are going (Robinson *et al.*, 1997). The rhizobox was put into the MRI scanner and a circular RF coil was installed on the root-plane side of the rhizobox close to the roots (Figure 3.3a). The first  $T_1$  measurement could be carried out 3 hours after the  $\text{Ni}^{+2}$  solution was applied to the rhizobox. The second and the third measurement were performed 5 and 11 hours after the application of  $\text{Ni}^{+2}$  solution, respectively. The rhizobox was kept at 16-19°C under fluorescent lighting (0.6 – 0.8 lumen cm<sup>-3</sup>) during the time between measurements. The amount of transpiration was measured by weighing the rhizobox before and after the experiment. We kept the upper compartment dry

before the MRI experiment, therefore, evaporation during the experiment and the transpiration from the upper compartment was considered negligible.

### 3.3.4 Modelling

Simulations were carried out using the numerical code MIN3P (Mayer *et al.*, 2001), which describes flow, transport and geochemical reactions in porous media including kinetic and equilibrium mass exchange with mineral phases and roots. MIN3P has been successfully used by Nowack *et al.* (2006) to simulate solute uptake by a single plant root. We used MIN3P to calculate the two-dimensional distribution of  $\text{Ni}^{2+}$  adjacent to the root plane in the rhizobox. The root plane was assumed to be a homogeneous sink for water and  $\text{Ni}^{2+}$ . Water was set to be taken up at a constant rate during the experiment. Nickel uptake was modeled following a volume-based Michaelis-Menten kinetics:

$$F_M = \frac{k_m c}{K_m + c} \quad , \quad (2)$$

where  $F_M$  is the effective root uptake rate per unit volume of the roots ( $\text{mol m}^{-3} \text{s}^{-1}$ ),  $k_m$  is the effective rate coefficient ( $\text{mol m}^{-3} \text{s}^{-1}$ ),  $K_m$  is the Michaelis-Menten's constant ( $\text{mol m}^{-3}$ ), and  $c$  is the  $\text{Ni}^{2+}$  concentration in solution, ( $\text{mol m}^{-3}$ ).

Sensitivity analysis showed that the most critical parameters were uptake rate, diffusion coefficient, and transpiration rate (data not shown here). The effective Ni uptake rate coefficient and the hydraulic parameters were fitted to yield the observed temporal evolution of the  $\text{Ni}^{2+}$  distribution. The Michaelis-Menten's constant was set to  $3.4 \times 10^{-4} \text{ mol m}^{-3}$  which is a reasonable value for a Ni hyperaccumulator plant and compared to the values reported for potassium and calcium (Barber, 1995; Nowack *et al.*, 2006). The other parameters were taken directly from the experiment. The dispersivity was set to  $9.0 \times 10^{-4} \text{ m}$ , and the initial  $\text{Ni}^{2+}$  concentration was  $10 \text{ mg litre}^{-1}$ . The glass beads were chemically inert, therefore no Ni was assumed to sorb to them. The grid resolution was set to correspond to the spatial resolution of the MRI, except that a finer grid was used in the direct vicinity of the roots.

## 3.4 Results and discussions

### 3.4.1 Temporal changes of $\text{Ni}^{2+}$ distribution

Figure 3.3b shows the distribution of roots in the root-only compartment before the Ni uptake experiment started. The horizontal sections, separated by the dashed line correspond to the slices into which the MRI signals were collected. There was a dense layer of roots in the first two slices, but the root density was lower in the bottom of the rhizobox. The root mat was composed of old and young roots in all slices. The root distribution was most homogeneous in the 3rd, 4<sup>th</sup> and 5<sup>th</sup> slice from the top.

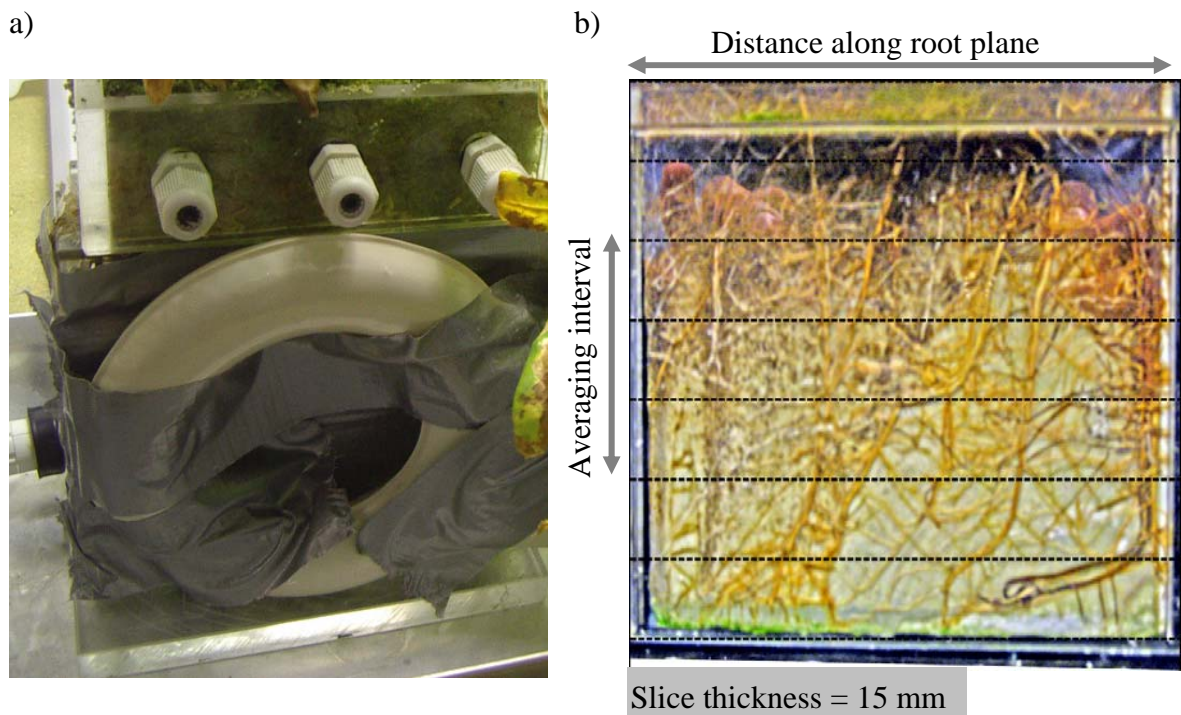


Figure 3.3: Root distribution pattern before the Ni uptake experiment, the broken lines indicate the imaging slices, which had a width of 15 mm (b) and a view of the receiver coil installation adjacent to the root plane (a)

The  $\text{Ni}^{+2}$  distribution map measured at various times after the application of Ni solution are shown in Figure 3.4. Each  $\text{Ni}^{+2}$  distribution map represents a pixel-wise average value of the slices 3, 4 and 5. Already at the first measurement, three hours after the start of the experiment (application of  $\text{Ni}^{+2}$  solution to the rhizobox), a gradient in the  $\text{Ni}^{+2}$  concentration was visible (Figure 3.4a). The  $\text{Ni}^{+2}$  concentration ranged from around 15 mg litre<sup>-1</sup> immediately adjacent to the root-plane to slightly above 10 mg litre<sup>-1</sup> at a distance of 20 mm away from the roots on the opposite side of the rhizobox. This indicates that the amount of Ni transported to the root surface via convection was greater than the amount of Ni taken up by the roots. The roots obviously excluded the  $\text{Ni}^{+2}$  to some degree and the

extent of the exclusion was greater in the middle of the root-plane than at the edges. This can be related to the variability due to the inhomogeneous distribution and activity of the roots. The area in blue at the corners of the rhizobox shows a heterogeneous pattern with  $\text{Ni}^{+2}$  concentrations below the initial concentration. The corners of the rhizobox were farthest away from the coil centre and showed a considerably higher variability in signal among pixels than in the centre of the rhizobox. This indicates that the reliability of the measurement decreased with distance from the coil centre due to a decline in coil sensitivity and a low signal-to-noise ratio. After 5 hours, the Ni accumulation zone extended to a distance of more than 20 mm away from the root surface in the middle of the root-plane (Figure 3.4b). The  $\text{Ni}^{+2}$  accumulation zone extended to the corners 11 hours after the experiment had started (Figure 3.4c), while the magnitude of the accumulation was still highest in the middle.

Figure 3.4d shows the average profiles of  $\text{Ni}^{+2}$  concentrations with distance from the root plane for each measurement time. As far as 15 mm from the root surface, the  $\text{Ni}^{+2}$  concentration continued to decrease without reaching the initial background concentration of  $10 \text{ mg litre}^{-1}$  3 hours after the start of the experiment. After 5 and 11 hours,  $\text{Ni}^{+2}$  concentrations were above 11 and  $12 \text{ mg litre}^{-1}$ , respectively, even at distances of more than 20 mm away from the root plane. The increase in  $\text{Ni}^{+2}$  concentration towards the root surface means that  $\text{Ni}^{+2}$  uptake by roots was not limited by diffusion at these relatively high soluble Ni concentrations. The enrichment of  $\text{Ni}^{+2}$  adjacent to the roots indicates that *Berkheya coddii* can hyperaccumulate Ni in ultramafic soils without solubilizing Ni in the root zone.

### 3.4.2 $\text{Ni}^{+2}$ concentration mapping at different soil water contents

As the plants transpired water, the water level in the rhizobox dropped and the upper part of the rhizobox became unsaturated. Figure 3.5a shows the Ni distribution in a vertical cross-section close to the roots and parallel to the root-plane at  $t = 11$  hours. With the decrease in water content, also the MRI signal decreased in the upper part of the rhizobox (shown in dark colour). Horizontal cross-sections through the rhizobox at an upper (unsaturated), middle (partly saturated), and lower level (saturated) are shown in Figures 3.5b, c, and d, respectively. In the unsaturated zone (Figure 3.5b), the MRI signal was much more heterogeneous and the signal-to-noise ratio was much poorer than in the saturated zone below. The red patches are likely due to entrapment of  $\text{Ni}^{+2}$  solution in pores or inside the porous beads due to loss of hydraulic continuity during drainage.

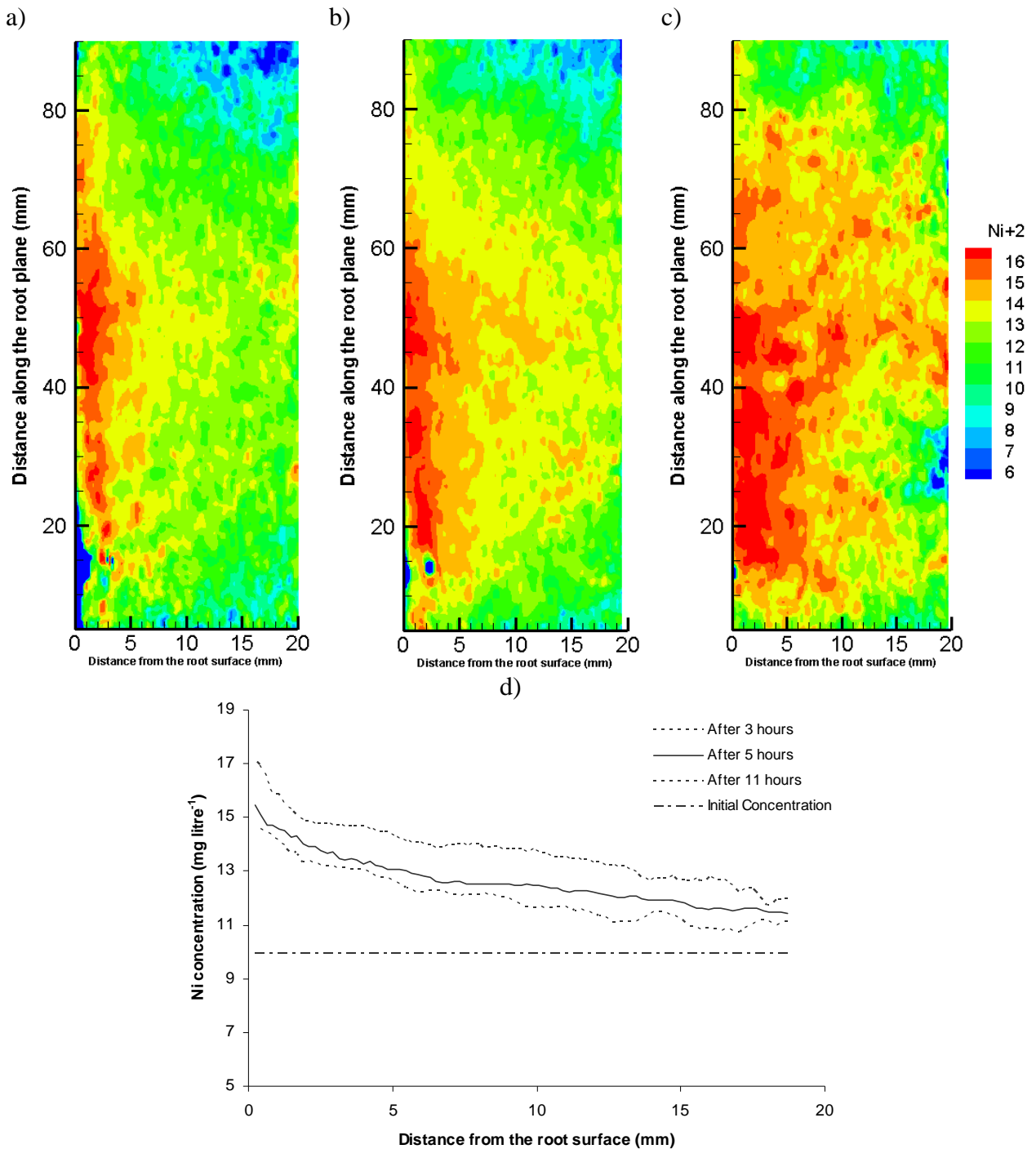


Figure 3.4: A horizontal two-dimensional map of the Ni<sup>2+</sup> distribution in the rhizosphere of *Berkheya coddii* 3 hours (a), 5 hours (b), and 11 hours (c) after Ni application to the rhizobox and the averaged Ni concentration profiles with distance from the root plane (d)

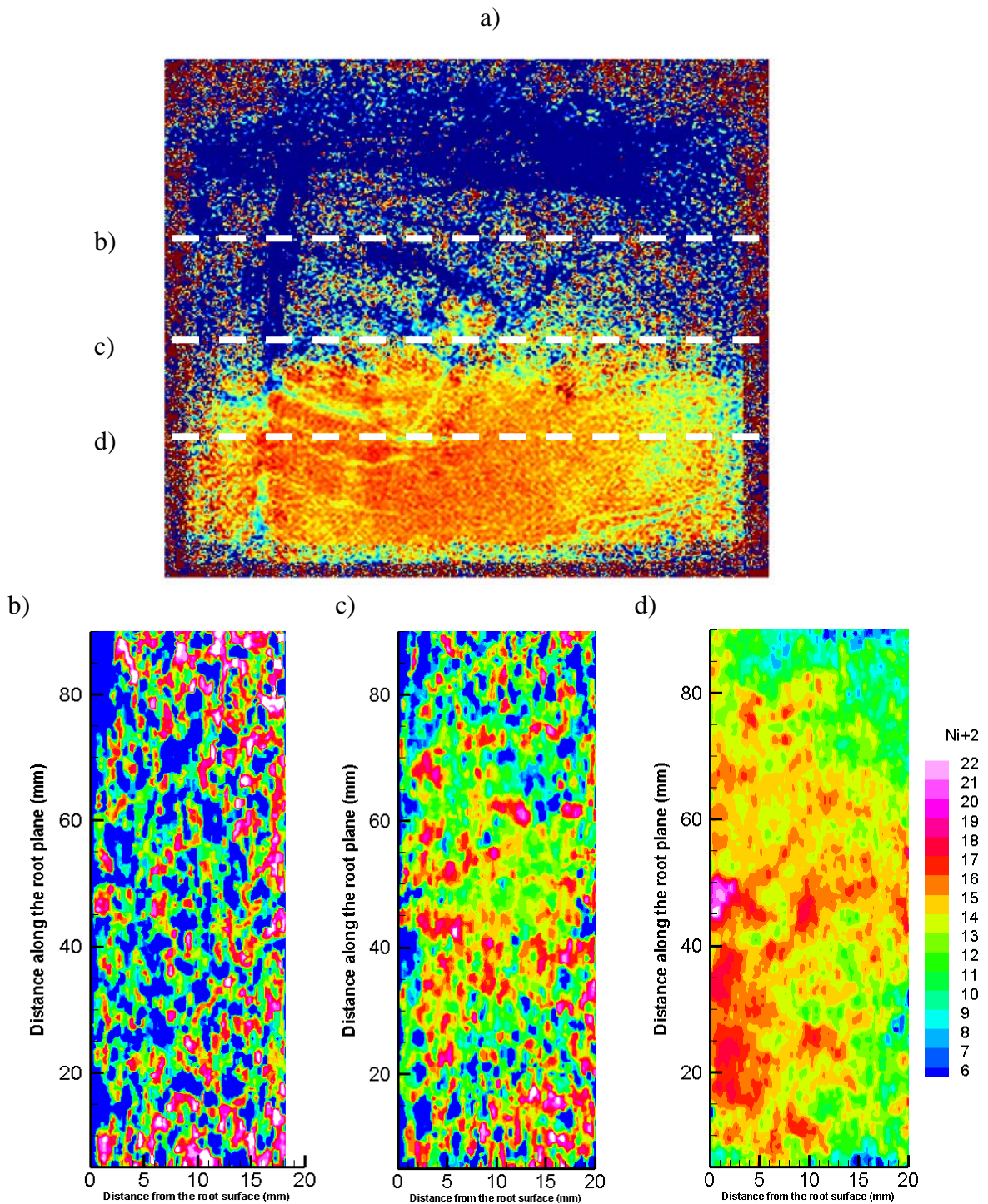


Figure 3.5: Vertical cross-section through the rhizobox system at a distance of 15 mm from the root plane at  $t = 11$  hours (a) and the maps of the  $\text{Ni}^{+2}$  distribution at three horizontal cross-sections along the broken lines shown in the vertical cross-section (b, c and d)

Our images had a spatial resolution of 0.21 x 0.21 mm, a slice thickness of 15 mm, and therefore, a voxel size of 0.21 x 0.21 x 15 mm. Considering the size of the glass beads (0.4–1.0 mm), the voxel's space is occupied by a combination of beads and pore space, and the particular distribution affects the signal intensity and relaxation behaviour. The resulting signal showed a considerable degree of random variability in unsaturated conditions, representing variations of water content but also water distribution in the pore space. Additionally, the variability of water saturation of the intra-grain pore space might affect the  $T_1$  relaxation behaviour. To correct for this, separate calibration curves would be needed for given water content and possibly also for different water distribution patterns in the pore space. However, since the main aim here was to visualize Ni concentrations close to the roots where full water saturation was persist during the experiments, only the location of the capillary fringe was monitored and MRI maps were not corrected for the desaturation effects. The signal-to-noise ratio increased in the middle of the rhizobox in the transition zone between saturated and unsaturated zone (Figure 3.5c) i.e. in the zone of capillary fringe above the water level, but the signal was considerably lower and more heterogeneous than in the fully saturated zone (Figure 3.5d).

The experimental set-up that we used here is a compromise between a MRI-suited medium and a realistic soil-root system. It proved to be useful to study the dynamics of Ni in the rhizosphere of hyperaccumulator plants. However, it suffered from fading of signal-to-noise ratio in unsaturated conditions.

### 3.4.3 Modelling $\text{Ni}^{+2}$ uptake

The best agreement between the simulated and MRI-measured Ni concentration profiles was obtained when the effective uptake rate was set to  $2.2 \times 10^{-3} \text{ mol m}^{-3} \text{ s}^{-1}$  (Figure 3.6). This value is comparable with published uptake rates for potassium and calcium (Barber, 1995; Nowack *et al.*, 2006). The simulation of the averaged  $\text{Ni}^{+2}$  profile at  $t = 3$  hours was the most satisfactory. The MRI-measured  $\text{Ni}^{+2}$  concentration was in good agreement with the simulated  $\text{Ni}^{+2}$  profile over the whole length from the root plane to the opposite wall. For  $t = 5$  and 11,  $\text{Ni}^{+2}$  concentration profiles were slightly overestimated adjacent to the root surface and underestimated at farther distances namely 5 – 15 mm from the roots. The MRI-measured  $\text{Ni}^{+2}$  profiles showed a gentler slope than the simulated ones. Our attempts to yield a better fit for all three measurement times did not result in a significant improvement unless we chosen an unrealistic diffusion coefficient in aqueous solutions for Ni.

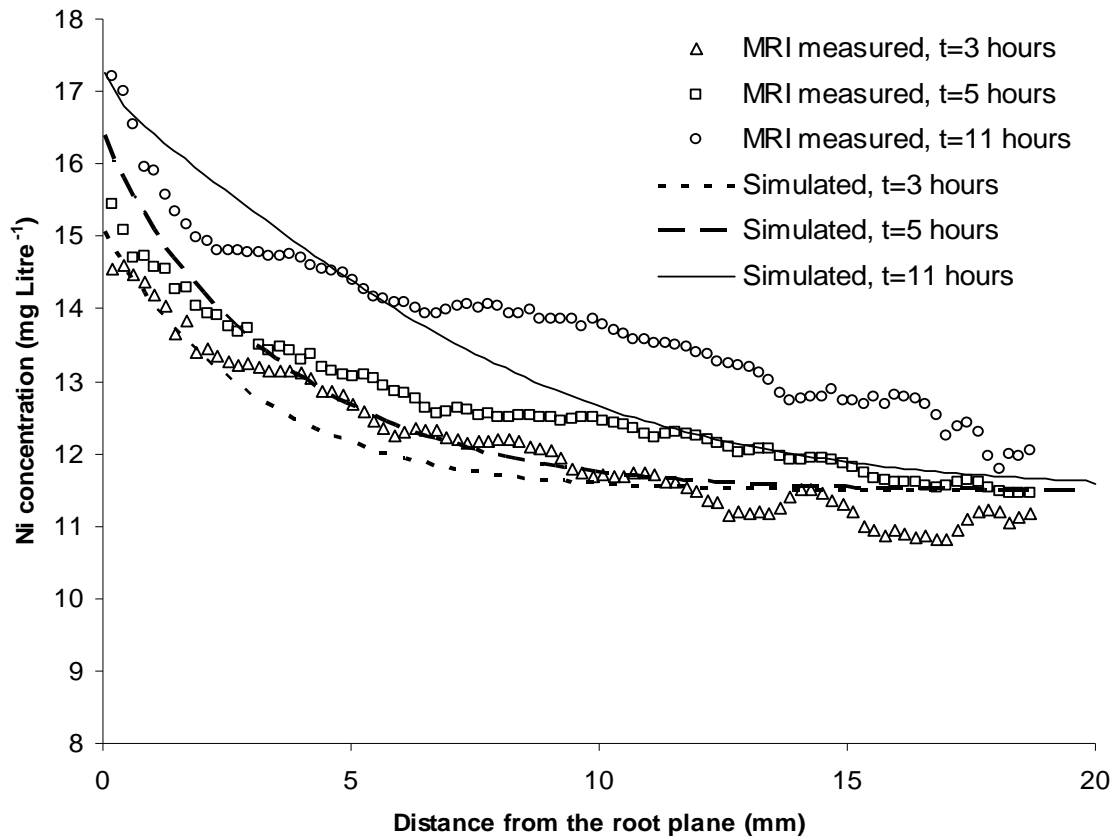


Figure 3.6: The MRI-measured and simulated  $\text{Ni}^{+2}$  concentration profiles as a function of distance from the root plane at 3, 5, and 11 hours after Ni application

#### 3.4.4 Effects of various parameters on $\text{Ni}^{+2}$ concentration profile

The magnitude and the sign of the  $\text{Ni}^{+2}$  gradient adjacent to the roots are essentially a function of Ni concentration in solution, the rate of  $\text{Ni}^{+2}$  uptake by the roots, and the transpiration rate. We performed a sensitivity analysis by varying these parameters in the model.

Figure 3.7 shows how transpiration rate affected the simulated  $\text{Ni}^{+2}$  concentration gradient. The transpiration rate was reduced by 40 and 80%, while all other parameters were kept constant. Reduction of the transpiration by 40% eliminated the gradient profile, while 80% reduction in transpiration resulted in a negative gradient towards the roots.

Varying the effective uptake rate had similar effects on the  $\text{Ni}^{+2}$  concentration profile. Increasing the uptake rate to  $3.1 \times 10^{-3}$  and  $4.6 \times 10^{-3} \text{ mol m}^{-3} \text{ s}^{-1}$  resulted in a zero gradient and a negative gradient of  $\text{Ni}^{2+}$ , respectively (data not shown here).

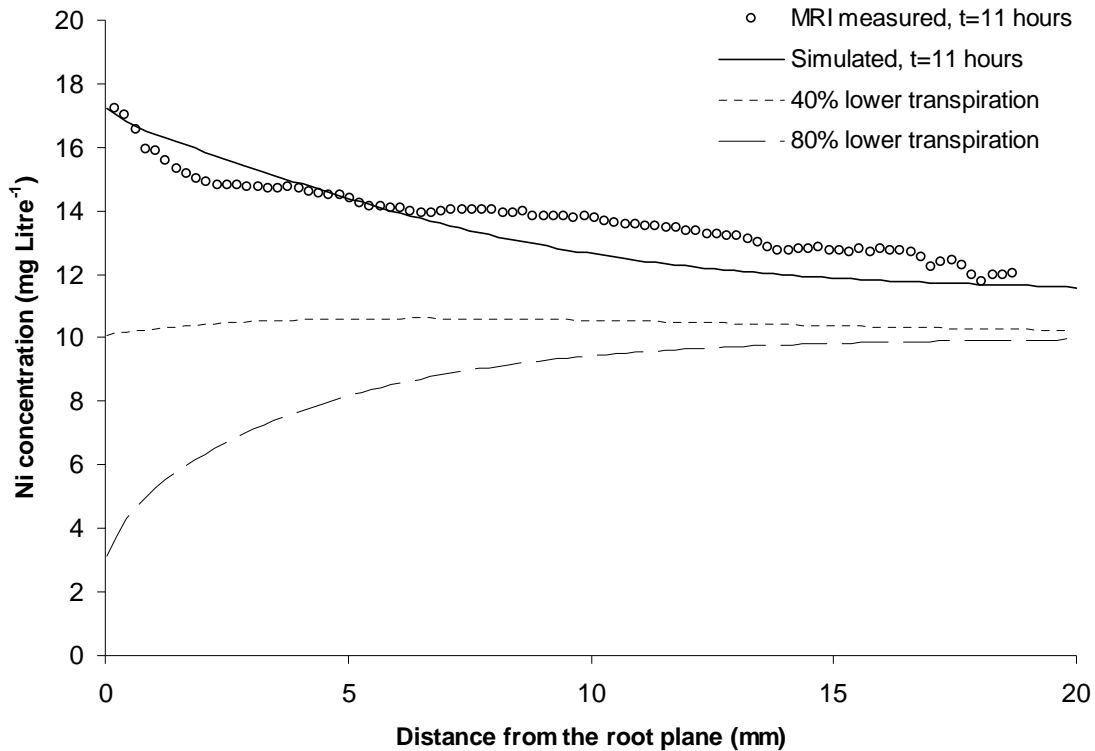


Figure 3.7: The MRI-measured and simulated  $\text{Ni}^{+2}$  concentration profile at  $t = 11$  hours and the simulation results assuming a transpiration rate of 40 and 80% of the measured transpiration

Dissolved Ni was found to reach concentrations up to  $12 \text{ mg litre}^{-1}$  in the soil solution of serpentine soils in *Berkheya coddii*'s native environment (Robinson *et al.*, 1997), while it is usually present in much lower concentrations in other soils. Figure 3.8 shows simulated  $\text{Ni}^{+2}$  profiles, assuming an initial  $\text{Ni}^{+2}$  concentration of  $0.1 \text{ mg litre}^{-1}$  for various uptake rates. Using a rate of  $2.2 \times 10^{-3} \text{ mol m}^{-3} \text{ s}^{-1}$  resulted in an extensive depletion of  $\text{Ni}^{+2}$  in the rhizosphere. To produce an accumulation pattern similar to the experimental ones but for an initial concentration of  $0.1 \text{ mg litre}^{-1}$ , a rate of  $1.5 \times 10^{-5} \text{ mol m}^{-3} \text{ s}^{-1}$  or less was needed. Using an uptake rate of  $3.1 \times 10^{-5} \text{ mol m}^{-3} \text{ s}^{-1}$  resulted in zero gradient profile.

Comparing Figures 3.6 and 3.8 reveals that using an effective uptake rate of  $2.2 \times 10^{-3} \text{ mol m}^{-3} \text{ s}^{-1}$  for an initial concentration of  $10 \text{ mg litre}^{-1}$  resulted in an accumulation pattern, while for an initial concentration of  $0.1 \text{ mg litre}^{-1}$  it resulted in an extensive depletion of Ni adjacent to the roots. This shows that a depletion of  $\text{Ni}^{+2}$  is expected at low dissolved concentration of  $\text{Ni}^{+2}$  in soil, if the effective uptake rate stays unchanged.

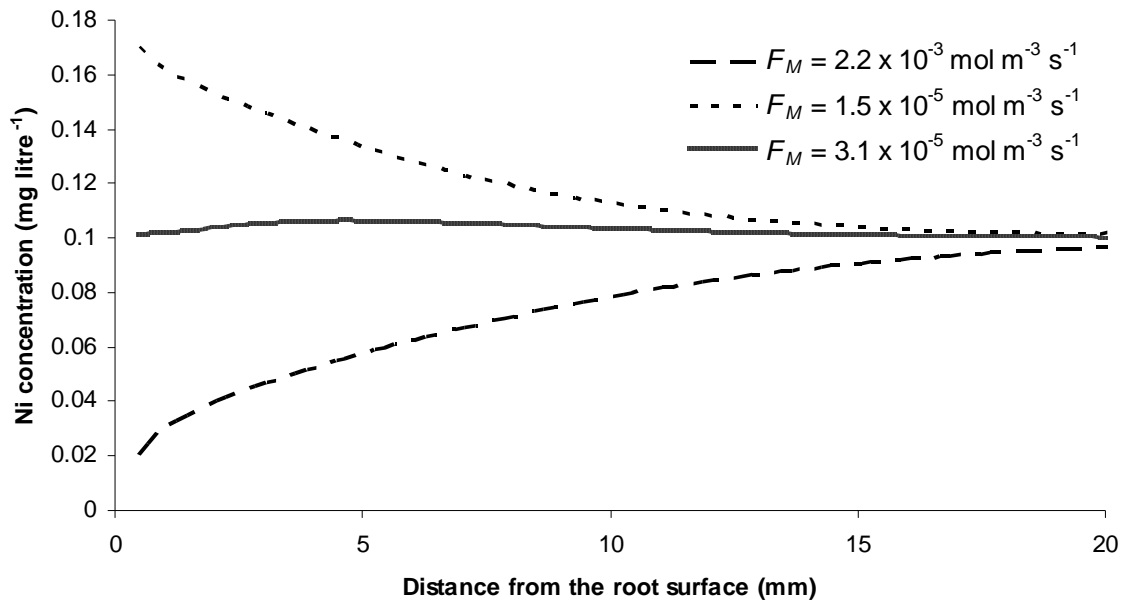


Figure 3.8: Simulated  $\text{Ni}^{+2}$  concentration profiles for three different uptake rates, assuming an initial  $\text{Ni}^{+2}$  concentration of  $0.1 \text{ mg litre}^{-1}$

### 3.5 Acknowledgements

This study was funded by the Swiss National Science Foundation. We would like to thank Reto Treier (IBE, ETH Zurich) for his technical support on  $T_1$  calculations.

### 3.6 References

- Angle, J.S., Chaney, R.L., Baker, A.J.M., Li, Y., Reeves, R., Volk, V., Roseberg, R., Brewer, E., Burke, S. & Nelkin, J. 2001. Developing commercial phytoextraction technologies: practical considerations. *South African Journal of Science*, **97**, 619-623.
- Ashworth, D.J. & Alloway, B.J. 2004. Soil mobility of sewage sludge-derived dissolved organic matter, copper, nickel and zinc. *Environmental Pollution*, **127**, 137-144.
- Barber, S.A. 1995. *Soil nutrient bioavailability: a mechanistic approach*. John Wiley & Sons, New York.
- Brooks, R.R. ed. 1998. *Plants that Hyperaccumulate Heavy Metals*. CAB International, Wallingford.

- Brooks, R.R., Chambers, M.F., Nicks, L.J. & Robinson, B.H. 1998. Phytomining. *Trends in Plant Science*, **3**, 359-362.
- Brooks, R.R., Lee, J., Reeves, R.D. & Jaffre, T. 1977. Detection of Nickeliferous Rocks by Analysis of Herbarium Specimens of Indicator Plants. *Journal of Geochemical Exploration*, **7**, 49-57.
- Brown, J.M., Kramer, P.J., Cofer, G.P. & Johnson, G.A. 1990. Use of Nuclear-Magnetic-Resonance Microscopy for Noninvasive Observations of Root-Soil Water Relations. *Theoretical and Applied Climatology*, **42**, 229-236.
- Clark, F.E. 1949. Soil Microorganisms and Plant Roots. *Advances in Agronomy*, **1**, 241-288.
- Cushman, J.H. 1980. Analytical Study of the Effect of Ion Depletion (Replenishment) Caused by Microbial Activity near a Root. *Soil Science*, **129**, 69-87.
- Darrah, P.R. 1993. The Rhizosphere and Plant Nutrition - a Quantitative Approach. *Plant and Soil*, **156**, 1-20.
- Deoni, S.C.L., Rutt, B.K. & Peters, T.M. 2003. Rapid combined T-1 and T-2 mapping using gradient recalled acquisition in the steady state. *Magnetic Resonance in Medicine*, **49**, 515-526.
- Gregory, P.J. & Hinsinger, P. 1999. New approaches to studying chemical and physical changes in the rhizosphere: an overview. *Plant and Soil*, **211**, 1-9.
- Herrmann, K.H., Pohlmeier, A., Wiese, S., Shah, N.J., Nitzsche, O. & Vereecken, H. 2002. Three-dimensional nickel ion transport through porous media using magnetic resonance Imaging. *Journal of Environmental Quality*, **31**, 506-514.
- Hinsinger, P., Plassard, C. & Jaillard, B. 2006. Rhizosphere: A new frontier for soil biogeochemistry. *Journal of Geochemical Exploration*, **88**, 210-213.
- Hoagland, D.R. & Arnon, D.I. 1938. The water culture method for growing plants without soil. *Calif. Agric. Exp. Stn*, **347**, 1-39.
- Kashem, A. & Singh, B.R. 2007. Soil amendment with city sewage sludge increases soil extractable cadmium, nickel and zinc more than tannery, pharmaceutical and paper mill wastes. *Acta Agriculturae Scandinavica Section B-Soil and Plant Science*, **57**, 134-139.
- Li, Y.M., Chaney, R., Brewer, E., Roseberg, R., Angle, J.S., Baker, A., Reeves, R. & Nelkin, J. 2003. Development of a technology for commercial phytoextraction of nickel: economic and technical considerations. *Plant and Soil*, **249**, 107-115.
- Mayer, K.U., Blowes, D.W. & Frind, E.O. 2001. Reactive transport modeling of an in situ reactive barrier for the treatment of hexavalent chromium and trichloroethylene in groundwater. *Water Resources Research*, **37**, 3091-3103.

- McNear, D.H., Peltier, E., Everhart, J., Chaney, R.L., Sutton, S., Newville, M., Rivers, M. & Sparks, D.L. 2005. Application of quantitative fluorescence and absorption-edge computed microtomography to image metal compartmentalization in *Alyssum murale*. *Environmental Science & Technology*, **39**, 2210-2218.
- Moradi, A.B., Oswald, S.E., Massner, J.A., Pruessmann, K.P., Robinson, B.H. & Schulin, R. 2008. Magnetic Resonance Imaging methods to reveal the real-time distribution of nickel in porous media. *European Journal of Soil Science*, **59**, 476-485.
- Nestle, N., Baumann, T., Wunderlich, A. & Niessner, R. 2003. MRI observation of heavy metal transport in aquifer matrices down to sub-mg quantities. *Magnetic Resonance Imaging*, **21**, 345-349.
- Nowack, B., Mayer, K.U., Oswald, S.E., van Beinum, W., Appelo, C.A.J., Jacques, D., Seuntjens, P., Gerard, F., Jaillard, B., Schnepf, A. & Roose, T. 2006. Verification and intercomparison of reactive transport codes to describe root-uptake. *Plant and Soil*, **285**, 305-321.
- Oswald, S., Kinzelbach, W., Greiner, A. & Brix, G. 1997. Observation of flow and transport processes in artificial porous media via magnetic resonance imaging in three dimensions. *Geoderma*, **80**, 417-429.
- Pierret, A., Doussan, C., Garrigues, E. & Mc Kirby, J. 2003. Observing plant roots in their environment: current imaging options and specific contribution of two-dimensional approaches. *Agronomie*, **23**, 471-479.
- Robinson, B.H., Brooks, R.R., Gregg, P.E.H. & Kirkman, J.H. 1999. The nickel phytoextraction potential of some ultramafic soils as determined by sequential extraction. *Geoderma*, **87**, 293-304.
- Robinson, B.H., Brooks, R.R., Howes, A.W., Kirkman, J.H. & Gregg, P.E.H. 1997. The potential of the high-biomass nickel hyperaccumulator *Berkheya coddii* for phytoremediation and phytomining. *Journal of Geochemical Exploration*, **60**, 115-126.
- Tan, K.H. & Nopamornbodi, O. 1979. Electron Microbeam Scanning of Element Distribution Zones in Soil Rhizosphere and Plant-Tissue. *Soil Science*, **127**, 235-241.
- Tinker, P.B. & Nye, P.H. 2000. *Solute movement in the rhizosphere*. New York : Oxford University Press.
- Treier, R., Steingoetter, A., Fried, M., Schwizer, W. & Boesiger, P. 2007. Optimized and combined T-1 and B-1 mapping technique for fast and accurate T-1 quantification in contrast-enhanced abdominal MRI. *Magnetic Resonance in Medicine*, **57**, 568-576.
- Valfouskaya, A., Adler, P.M., Thovert, J.F. & Fleury, M. 2005. Nuclear-magnetic-resonance diffusion simulations in porous media. *Journal of Applied Physics*, **97**.

- Van As, H. & van Dusschoten, D. 1997. NMR methods for imaging of transport processes in micro-porous systems. *Geoderma*, **80**, 389-403.
- Wenzel, W.W. 2005. Rhizosphere Conference. *Journal of Environmental Quality*, **34**, 2156-2156.
- Wenzel, W.W., Wieshammer, G., Fitz, W.J. & Puschenreiter, M. 2001. Novel rhizobox design to assess rhizosphere characteristics at high spatial resolution. *Plant and Soil*, **237**, 37-45.
- Whiting, S.N., Broadley, M.R. & White, P.J. 2003. Applying a solute transfer model to phytoextraction: Zinc acquisition by *Thlaspi caerulescens*. *Plant and Soil*, **249**, 45-56.
- Zhao, F.J., Hamon, R.E., Lombi, E., McLaughlin, M.J. & McGrath, S.P. 2002. Characteristics of cadmium uptake in two contrasting ecotypes of the hyperaccumulator *Thlaspi caerulescens*. *Journal of Experimental Botany*, **53**, 535-543.



---

## 4 Laser-ablation mapping of nickel in root cross-sections of the hyperaccumulator plant *Berkheya coddii*

---

*Ahmad B. Moradi, Siegfried Swoboda, Brett Robinson, Thomas Prohaska, Anders Kaestner, Sascha Oswald, Walter W. Wenzel, Rainer Schulin*

*Submitted for publication in Planta*



## 4.1 Abstract

Quantitative Studies of the distribution pattern of metals in plant tissues provide important information on the potential of metal-accumulator plants for the remediation and amelioration of contaminated soils. We used laser ablation combined with inductively coupled plasma mass spectrometry (LA-ICP-MS) as well as staining with dimethylglyoxime (DMG) to investigate the distribution of nickel (Ni) in the root cross-sections of the Ni-hyperaccumulator plant *Berkheya coddii*. Plants were grown in rhizoboxes containing soil with 125 mg kg<sup>-1</sup> Ni. Roots were embedded in resin and cut into sections for LA-ICP-MS analysis. For DMG-staining analysis, no embedding was used and fresh root cross-sections were prepared using microtome. Ni concentrations measured by LA-ICP-MS were compared with an analysis of soil and root samples using XRF and ICP-OES, respectively. LA-ICP-MS revealed higher Ni concentrations in the cortex (374 ± 66 mg kg<sup>-1</sup>) than in the stele (210 ± 48 mg kg<sup>-1</sup>) of the plant roots. The distribution pattern agreed well with those found by DMG-staining. In the control plants not exposed to elevated soil Ni, higher concentrations of Ni were found in the stele than in the cortex using both techniques. Our results indicate that an active uptake or ion selection mechanism exist for *Berkheya coddii* in absence of available Ni in the rhizosphere.

**Key words:** *Berkheya coddii*, cortex, dimethylglyoxime , laser ablation, nickel, root cross-section, stele

## 4.2 Introduction

Hyperaccumulator plants may offer a sustainable treatment option for the remediation of metal-contaminated sites (mining activity, refinery emissions, waste disposal, fossil fuel combustion, and agricultural application of pesticides and biosolids) and also an opportunity to mine naturally metal-rich soils i.e. phytomining of ultramafic soils (Brooks *et al.*, 1998; Angle *et al.*, 2001; Li *et al.*, 2003). *Berkheya coddii* Rossler is a Ni-hyperaccumulator plant that has attracted particular attention because of its high Ni concentration and rapid biomass production. Robinson *et al.* (1997) reported an annual biomass production of 22 t ha<sup>-1</sup> and up to 1% (w:w) Ni in the above-ground biomass. The combination of these two traits is rare and may make this plant suitable for the remediation of Ni-contaminated soils by means of phytoextraction. *Berkheya coddii* is an asteraceous summer-green perennial plant that is found on ultramafic (serpentine) soils in southern Africa (Morrey *et al.*, 1992).

A nickel hyperaccumulator plant is defined as a plant with Ni concentrations exceeding 1000 mg kg<sup>-1</sup> dry weight in the above-ground biomass (Brooks *et al.*, 1977). The mechanisms involved in metal hyperaccumulation by plants are poorly understood. This is exacerbated by a lack of methods for analysing metal distribution and localisation in plant tissues, cells and organelles.

Methods currently used for spatial localization of metals within biological tissues are primarily micro analytical techniques based on X-ray emission in response to irradiation with charged particles (Bhatia *et al.*, 2004), including micro-PIXE (micro proton-induced X-ray emission spectroscopy; also known as nuclear microprobe) and EDXS (energy dispersive X-ray spectroscopy). Both methods simultaneously measure and map elemental contents. While micro-PIXE gives higher analytical sensitivities than EDXS (Przybylowicz *et al.*, 2001), the application of micro-PIXE is limited by accessibility to a proton-beam facility.

Laser-Ablation combined with Inductively-Coupled-Plasma Mass-Spectrometry (LA-ICP-MS) determines a large number of elements with a relatively high spatial resolution (down to 1 µm) at detection limits in the µg kg<sup>-1</sup> range (Russo *et al.*, 2002; Hattendorf *et al.*, 2003; Kylander *et al.*, 2007). LA-ICP-MS has been used for high-resolution biological and physiological analysis of plants (Prohaska *et al.*, 1998; Hoffmann *et al.*, 2000; Polatajko *et al.*, 2007; Ulrich *et al.*, 2007).

On the other hand, histochemical staining methods are less accurate, but are low cost and do not require an expensive facility. In particular, dimethylglyoxime (DMG) has frequently been used as a histochemical stain for localisation of Ni within tissues of hyperaccumulator

plants (Heath *et al.*, 1997; Mizuno *et al.*, 2003; Bhatia *et al.*, 2004; Budka *et al.*, 2005). While this method has many potential applications, Bhatia *et al.* (2004) warned of the risk of artefacts due to the displacement of Ni with the solvent front during staining. However, these problems may be alleviated by strict preparation protocols (Gramlich *et al.*, 2007). Robinson *et al.* (2003) showed that up to 65% of the total Ni could be present in a water-soluble form in the leaves of *Berkheya coddii*. Such high amounts of soluble Ni could be easily redistributed within the cell during fixation or the substitution of water by other solvents (Budka *et al.*, 2004). Therefore any fixation, sectioning and drying should be performed under low temperature (Budka *et al.*, 2005). However, the risk of redistribution at the tissue level is less severe than at the sub-cellular level (Budka *et al.*, 2005).

The highest Ni concentration occur in the leaves of hyperaccumulators, therefore leaf tissue has been the subject of most previous investigations (Robinson *et al.*, 2003; Bhatia *et al.*, 2004; Budka *et al.*, 2005; Berazain *et al.*, 2007; de la Fuente *et al.*, 2007; Tappero *et al.*, 2007). Proton or nuclear microprobe analyses of *Berkheya coddii* collected from native South African ultramafic soils showed that Ni was concentrated in the mesophyll and epidermis of the leaves (Mesjasz-Przybylowicz *et al.*, 2001). Although roots are the prime site of uptake of metals, the distribution of Ni in root tissues of *Berkheya coddii* has not been investigated. Most research regarding Ni hyperaccumulation and uptake has been carried out on Ni hyperaccumulator plants of the family Brassicaceae and is unclear whether other hyperaccumulators have the same uptake mechanism and distribution pattern as Brassicaceae family (Robinson *et al.*, 2003).

In this study, we investigated the quantitative and qualitative spatial distribution of Ni in the roots cross-sections of the hyperaccumulator plant *Berkheya coddii* using LA-ICP-MS. The distribution pattern and the Ni concentrations determined by means of this technique were compared to the results of DMG-staining and ICP-OES measurements.

## **4.3 Materials and methods**

### **4.3.1 Rhizobox experiment and sampling**

We grew seedlings of *Berkheya coddii* three weeks in perlite and then transferred them to rhizoboxes with a height of 60 cm, a width of 15 cm and a breadth of 1 cm in the main rooting compartment. Dessureault-Rompere *et al.* (2006) gives a detailed description of these boxes. The narrow breadth facilitated sampling of undisturbed roots for the impregnation in resin. Three rhizoboxes were filled with sandy soil spiked with 125 mg kg<sup>-1</sup> Ni, and three with the same soil, unspiked, as a control. We sprayed nickel solution on the spiked soil and

stirred the soil well to mix the soil with Ni as homogeneous as possible. The rhizoboxes were irrigated with Hoagland's nutrient solution (Kramer *et al.*, 1996). The soil water content was maintained near field capacity (25 %) by adding 150-200 ml of solution per week. After transplanting, the rhizoboxes were kept in a climate chamber for 8 weeks with a daily light cycle of 16 h light/ 8 h darkness, and constant humidity (75%) and controlled temperature (16/ 23°C night/day).

In the 8<sup>th</sup> week, the boxes were carefully dismantled. First, undisturbed soil samples containing roots were taken using samplers with dimensions of 2 x 2 x 10 cm. These samples were impregnated in resin and analysed using LA-ICP-MS. We carefully separated the remaining roots from the soil and divided them into groups of the same age and diameter and used for ICP-OES analysis, DMG-staining as well as LA-ICP-MS analysis (impregnated in resin).

For LA-ICP-MS analysis, the soil samples containing undisturbed roots and also the root samples, separated from the soil and washed with deionised water, were first shock frozen using liquid nitrogen, freeze-dried and then impregnated under vacuum with an epoxy resin (LR White; London Resin Company Limited, Berkshire, GB). Heat curing under vacuum was used, with a temperature of 50°C for a period of 24 hours. Subsequently, the samples were cut into sections with height of 15 mm by means of a diamond saw (Accutom-50; Struers, Ballerup, DK). The surfaces were left unpolished to avoid smearing. Resin blanks were prepared and subsequently analyzed in the same way as the root cross-sections. We found no traces of Ni or other metals in the blank samples.

For the ICP-OES measurement, the roots were washed with deionised water and dried at 65°C for 48 hours, then digested with 15 ml HNO<sub>3</sub> (65%) at 150 °C for 1 hour in Teflon tubes on a heating block DigiPREP MS (SCP Science, QC, Canada). The digests were diluted to 20 ml with nanopure water and analysed for Ni, Ca, Mg, and Fe using ICP-OES (Vista-MPX Varian, Australia). For quality assurance, we digested and analysed certified reference material from the Community Bureau of Reference BCR (No. 62, *Olea europaea*). We obtained recoveries of 80% for Ni in the certified reference plant materials compared to the certified and reported values by the Community Bureau of Reference BCR. The detection limit in the extracts was established as 1 µg L<sup>-1</sup>.

Samples of the control and Ni-spiked soils were ground using a Retsch RS1 grinder with a tungsten carbide ball and ring, pressed into pellets and analysed by X-ray fluorescence (X-Lab 2000, Spectro, Kleve, Germany) for major elements, including Ca, Mg, Fe, and Ni. The analytical quality of the XRF measurements was routinely controlled by use of a certified standard sample (D133, MCACAL).

### 4.3.2 LA-ICP-MS analysis

The LA-ICP-MS system consisted of a 193 nm neodymium-doped yttrium aluminum garnet laser (New Wave Research, Huntingdon, UK) for sampling and a quadrupole inductively coupled plasma mass spectrometer (ICP-Q-MS, ELAN 6100 DRC-e, Perkin Elmer, Ontario, Canada), for analysing the ablated sample. The ablation cell was coupled via 50-cm PFA-tubing to the ICP-torch. Argon was used as carrier gas

The surfaces of the cross-sections were pre-ablated to eliminate possible contamination caused by the cutting process. For the pre-ablation, we used line scan mode (ablating along a line) with a laser beam diameter of 120  $\mu\text{m}$ , a laser energy of 15 % and a scan speed of 20  $\mu\text{m s}^{-1}$ . After pre-ablation, the samples were scanned using a laser energy of 65 %, a laser beam diameter of 75  $\mu\text{m}$  and a scan speed of 5  $\mu\text{m s}^{-1}$ . The frequency of the laser was kept at 10 Hz. Depending on the diameter of the root cross-section, each cross-section was ablated five or six times along parallel patterns to cover the entire root cross-section area.

An element with a known concentration which is homogeneously distributed in reference material and the samples is used for internal normalization of the signal to correct for any differences in ablation rates (Longerich *et al.*, 1996; 1997). Thus, a response factor (Cromwell & Arrowsmith, 1995; Motelica-Hieno & Donard, 2001; Resano *et al.*, 2005) for each analyte relative to the internal standard in the reference material can be calculated. The response factor reflects sensitivity differences between the analyte,  $E$ , and the element used as internal standard. Assuming that the response factor is the same for reference material and the sample, the concentration of an element  $E$  in the sample can be calculated as follows:

$$C_{Sam}(E) = \left( \frac{I_{ESam} C_{ERef}}{I_{ISSam} C_{ISRef}} \right) C_{ISSam} \left( \frac{I_{ISRef}}{I_{ERef}} \right) \quad , \quad (1)$$

where  $C_{ISSam}$  is the independently measured concentration of the internal standard in the sample,  $C_{ERef} / C_{ISRef}$  is the ratio of the concentrations of analyte  $E$  and internal standard  $IS$  in the certified reference material, and  $I_{ESam} / I_{ISSam}$  and  $I_{ISRef} / I_{ERef}$  are the intensity ratios measured in sample and reference material, respectively.

We used the response factor given in the Elan DRC-e software to calculate the concentrations in the samples. The concentration of analyte,  $E$ , is calculated using the relative sensitivity coefficient (RSC) from the ELAN DRC-e ICP-MS:

$$C_{Sam}(E) = \frac{\left( \frac{I_{ESam}}{I_{ISSam}} \right) C_{ISSam}}{RSC_{ICP-MS}} \quad (2)$$

More than one isotope was measured for each element to avoid any interference between the isotopes. Because the signal intensity of  $^{44}\text{Ca}$  was uniform over the cross-sections, we used this isotope as an internal standard to calculate the concentrations of Ni, Mg, and Fe. The second stable element was  $^{25}\text{Mg}$  and was used as internal standard to calculate concentration of Ca.

### 4.3.3 DMG Staining and image processing

The risk of artefacts from Ni redistribution in the course of the staining procedure depends on the solvent and the time between DMG application and imaging. We tested various solvents that previous studies have proposed, using equally prepared plant samples. Based on these preliminary tests, we selected a DMG solution containing 1 g DMG and 0.18 g KOH dissolved in 100 ml of 0.025 M  $\text{Na}_2\text{B}_4\text{O}_7 \cdot 10 \text{H}_2\text{O}$  solution (Merck, Darmstadt, Germany). This solution gave the best staining quality while preserving plant structure (Gramlich *et al.*, 2007). Comparing various sample preparation methods and immersion times, the procedure that gave the best results was as follows: A droplet of 30 $\mu\text{l}$  of the DMG solution was applied to freshly cut root cross sections of 150 $\mu\text{m}$  thickness. Immediately after adding the droplet, the cross section was imaged using light microscopy and photographed using a digital camera (Canon Power Shot A640).

The Karhunen-Loewe transform (Jain, 1989) was used to separate the signal originating from the dye (DMG-Ni stain) from the rest of the image. Inspection of collocation histograms for the color channel combinations Red-Green (RG), Red-Blue (RB), and Green-Blue (GB) showed that the RG combination was the best suited for this separation. The Karhunen-Loewe transform uses the eigenvector matrix derived from the covariance matrix of the two color channels as a linear transformation matrix for the two channels to obtain the independent basis images. The basis image corresponding to the greater eigenvalue contains the information of the DMG-Ni stain.

Image analysis was carried out using MATLAB. All statistical comparisons were done using analysis of variance ANOVA, while the confidence coefficient was set at 0.05.

a)

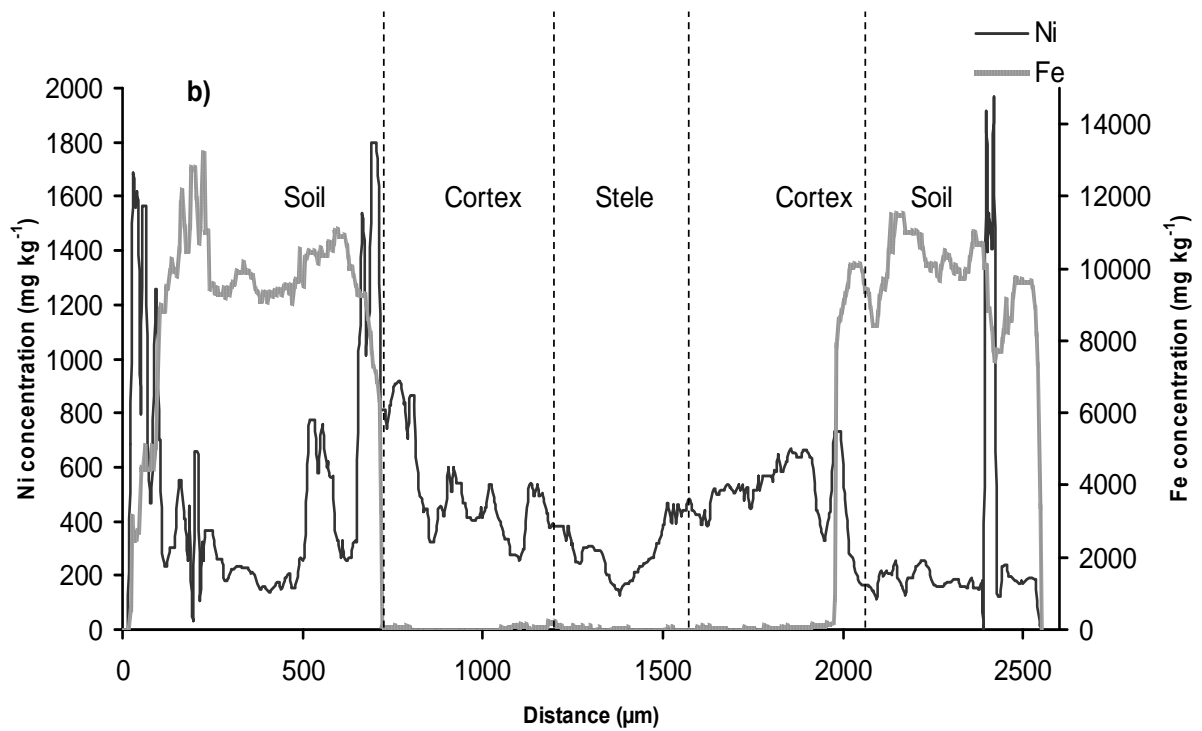


Figure 4.1: Laser image of a cross-section through a *Berkheya coddii* root and surrounding soil (a) and Ni and Fe concentration profiles along a scan line across the cross-section (b). The soil was spiked with  $125 \text{ mg kg}^{-1}$  Ni.

## 4.4 Results

### 4.4.1 Analysis of LA-ICP-MS line scans

Figure 4.1a shows a laser image with two laser line scans passing through the cross-section of a *Berkheya coddii* root grown in soil containing 125 mg kg<sup>-1</sup> Ni. The cortex and the stele of the root are clearly visible. The Ni concentration along one of the two laser lines is shown in Figure 4.1b. In the soil adjacent to the root, the nickel concentration varied from 100 to 1800 mg kg<sup>-1</sup> due to the heterogeneous distribution of soil particles and pores. Inside the roots, the concentration was higher and less variable than in the soil. We used the Fe: Ni ratio to locate the epidermis. Inside the root, the iron concentration dropped to a value below 100 mg kg<sup>-1</sup>, while the Ni concentration increased across the root surface. In addition, there was an increase of the Fe concentration near the epidermis before it started to decline inside the root. Similar Fe-concentration peaks occurred near the epidermis of the roots that had been washed in deionised water before embedding in resin. This can be attributed to soil particles attached to the root's surface. Although the roots were washed carefully, some soil particles could not be removed because of the roughness of the root surface and also because some remained trapped in the root fractures while growing (Tinker & Nye, 2000). The minimum Ni concentration within the root occurred in the stele in the centre of the root. The Ni concentration averaged around 500 mg kg<sup>-1</sup> in the cortex and less than 200 mg kg<sup>-1</sup> in the stele.

### 4.4.2 Analysis of DMG-stained root cross-sections

Figure 4.2 shows a cross-section of a root grown in soil containing 125 mg kg<sup>-1</sup> Ni, with almost the same diameter as the root in Figure 4.1. The root in Figure 4.2a was stained with DMG. The red area shows where the Ni-DMG complexes were located in the root. Figure 4.2a shows that the cortex was more intensively stained than the stele. Within the cortex, the red intensity was higher in the apoplastic space within and around the cell walls than in the cytoplasm. Transformation of the image by Karhunen-Loewe transform resulted in Figure 4.2b. In this image, the red intensity corresponds to the intensity of Ni-DMG complex. As Figure 4.2c shows, the pattern of Ni along a transect through the cross-section was similar to the pattern observed in the laser-scanned cross-section. The stele had the lowest red intensity while the epidermis had the highest red intensity. In contrast to the laser-scanned pattern, the difference between the red intensity of the cortex and the stele was more pronounced.

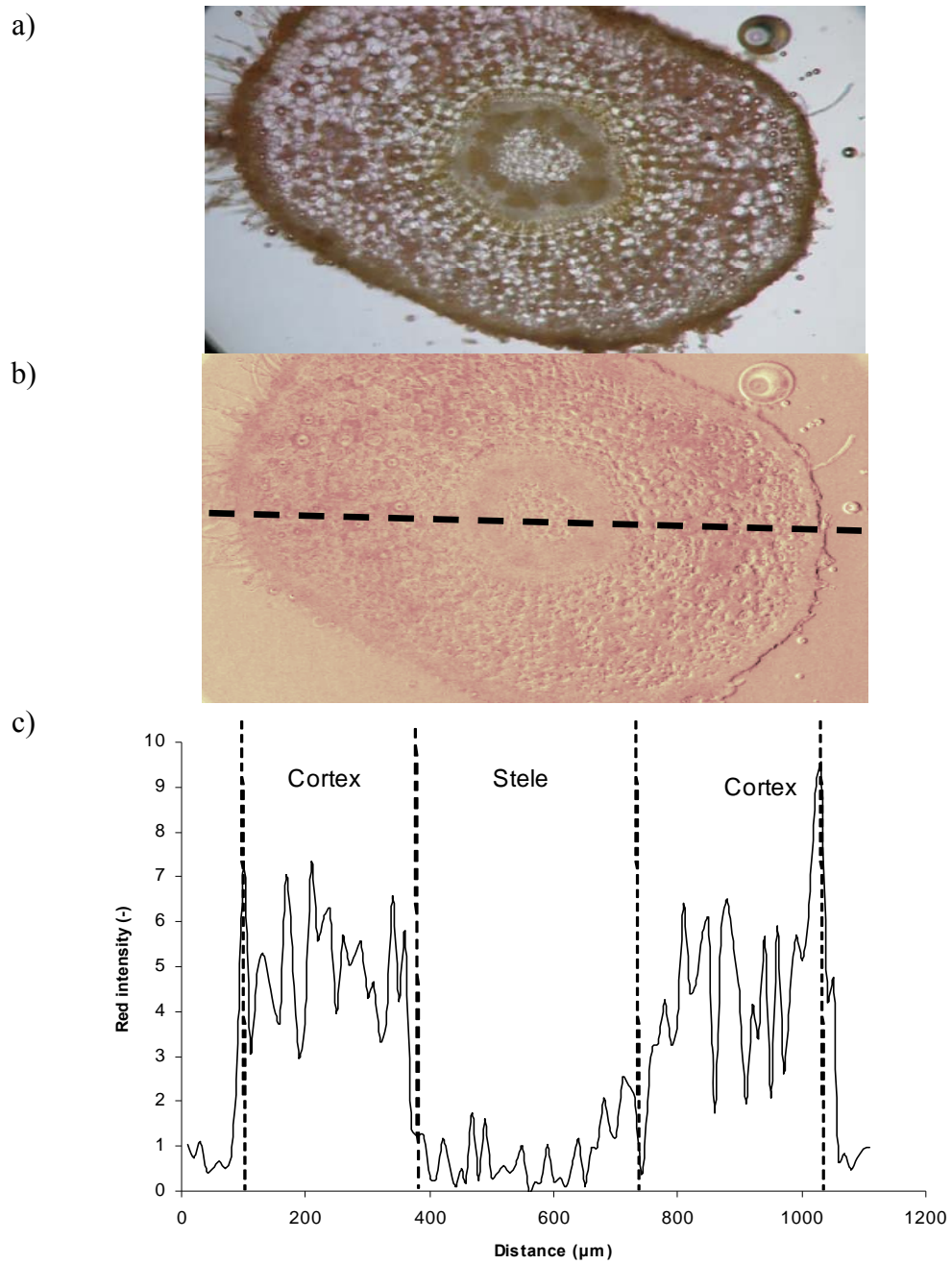


Figure 4.2: Microscopic image of a root cross-section of Ni-hyperaccumulator plant *Berkheya coddii* grown in Ni-spiked soil and stained with DMG solution (a), the same image after processing using Karhunen-Loeve transform to separate the dye signal from the rest of the image (b) and the resulting red intensity profile along the root cross-section. The red intensity results from the DMG-NI complex.

#### 4.4.3 Two-dimensional map of Ni in root cross-section

Seven parallel laser line-scans were recorded from a root cross-section of the 125 mg Ni kg<sup>-1</sup> Ni treatment to cover the entire root cross-section area. Figure 4.3 shows the 2-dimensional map of the Ni concentration of the root cross-section calculated from these scan lines. The nickel concentrations varied from 100 - 500 mg kg<sup>-1</sup>. The highest concentrations of Ni occurred in small spots that were distributed heterogeneously over the cortex. The stele showed a more homogenous distribution of Ni than the cortex.

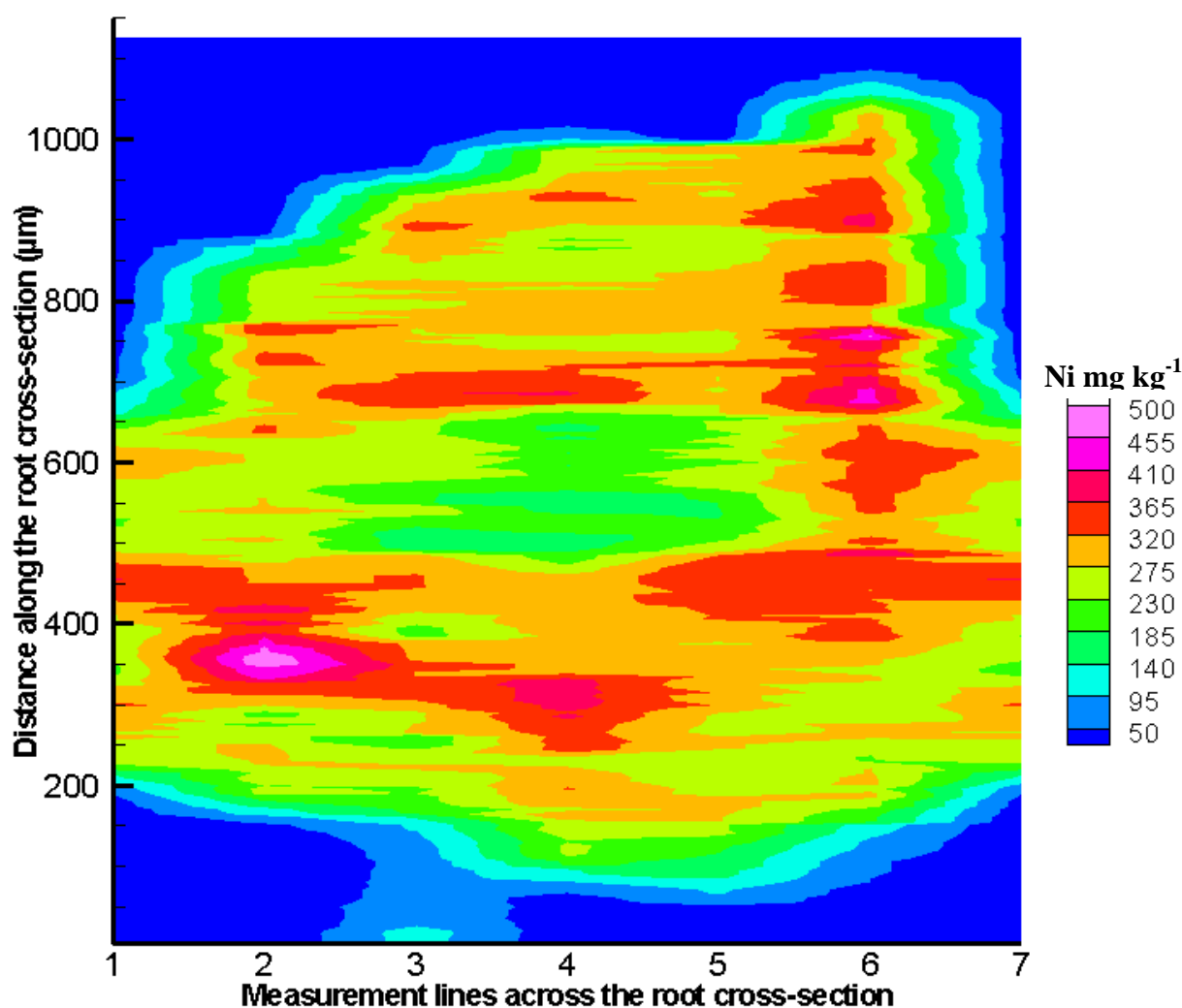


Figure 4.3: Quantitative Ni map of the root cross-section of Ni-hyperaccumulator plant *Berkheya coddii* grown on soil spiked with 125 mg Ni per kg

Likewise, six laser scan-lines were recorded from a cross-section of a root grown in the control soil. The resulting 2-D map of Ni concentration is shown in Figure 4.4. Unlike the roots in the spiked soil, the greatest concentration of Ni occurred in the stele. Here the Ni concentration averaged around  $50 \text{ mg kg}^{-1}$ , while it averaged around  $22 \text{ mg kg}^{-1}$  in the cortex.

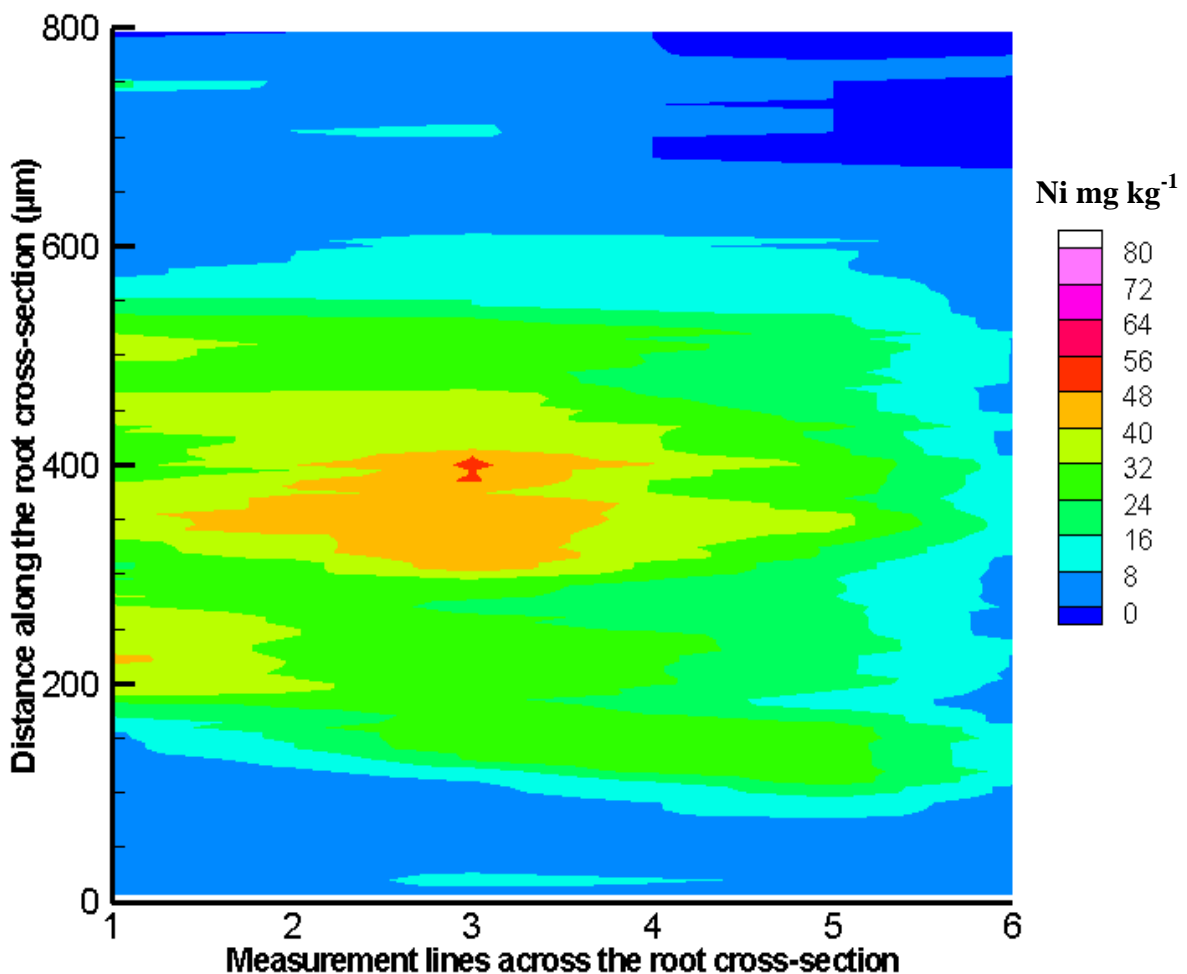


Figure 4.4: Quantitative Ni map of the root cross-section of Ni-hyperaccumulator plant *Berkheya coddii* grown on control soil

#### 4.4.4 Comparing LA-ICP-MS and DMG staining results

Figure 4.5 shows a comparison between the Ni concentrations measured by means of LA-ICP-MS and the red intensities of the DMG-staining for both control and Ni-treated roots.

Five replicates for each treatment were used to calculate the average and standard deviation of the Ni concentration and red intensity of various tissues of the roots. The cortex was divided equally into the outer and inner cortex, while the overall average of the stele was calculated. The background refers to either the resin around the roots in laser ablation experiment or an open area without any sample in DMG-staining experiment. The root diameters were in the range of 1 to 1.5 mm.

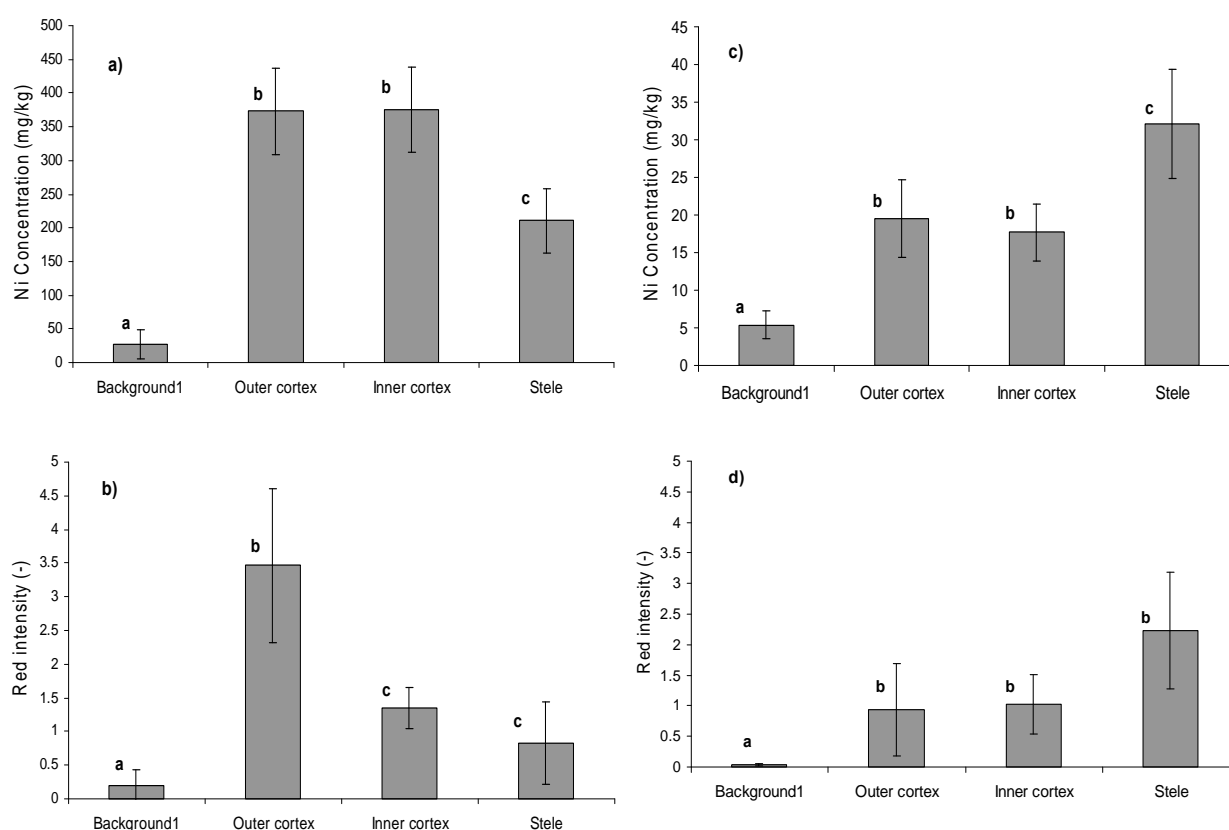


Figure 4.5: Average Ni concentrations (measured using LA-ICP-MS) and the red intensity of DMG staining in different root tissues of the Ni-hyperaccumulator *Berkheya coddii* grown on soil spiked with 125 mg Ni per kg (a and b) and uncontaminated soil (c and d). The error bars represent standard deviations, bars with different letters were significantly different at the 0.05 level.

In the LA-ICP-MS measured roots of the Ni-spiked treatment (Figure 4.5a), there was no significant difference (based on analysis of variance, ANOVA) between the outer and inner cortex ( $373 \pm 63$  and  $375 \pm 70$  mg kg<sup>-1</sup> respectively), while the Ni concentrations of the stele

was significantly lower ( $210 \pm 48 \text{ mg kg}^{-1}$ ). In the DMG-stained roots of the same treatment (Figure 4.5b), however, the red intensity decreased from the outer to the inner cortex. While there was no significant difference between the inner cortex and the stele, they both had significant lower intensities than the outer cortex. Again, the stele had larger intensities than the background.

*Table 4.1: Elemental concentrations ( $\text{mg kg}^{-1}$ ) of the roots and soil using various techniques.*

*The number following the  $\pm$  represents the standard deviation.*

			XRF	ICP-OES	LA-ICP-MS*
Ni	Control	Soil	$18.6 \pm 4.3$		$8.7 \pm 7.2$
		Root		$29.2 \pm 27$	$22.2 \pm 5.4$
Ni-spiked		Soil	$113.8 \pm 29$		$205.5 \pm 44$
		Root		$465.1 \pm 70.1$	$333.2 \pm 60$
Fe	Control	Soil	$14180 \pm 548$		$9067 \pm 490$
		Root		$143.6 \pm 38$	$24.2 \pm 44$
Ni-spiked		Soil	$14330 \pm 320$		$8821 \pm 441$
		Root		$80.3 \pm 67$	$32.3 \pm 53.7$
Mg	Control	Soil	$4260 \pm 170$		$5302 \pm 403$
		Root		$1954.5 \pm 841$	$2243 \pm 393$
Ni-spiked		Soil	$4560 \pm 216$		$4889 \pm 367$
		Root		$2115.3 \pm 1121$	$2940 \pm 270$
Ca	Control	Soil	$6596 \pm 348$		$11549 \pm 4700$
		Root		$9144 \pm 1117$	$12050 \pm 5393$
Ni-spiked		Soil	$5742 \pm 288$		$10048 \pm 5117$
		Root		$5876 \pm 421$	$12420 \pm 5521$

*Averages were calculated based on the area contribution of each tissue for roots.*

In contrast to the Ni-spiked treatment, the roots grown in the control soil (Figure 4.5c), had higher Ni concentrations in the stele ( $32 \pm 7 \text{ mg kg}^{-1}$ ) than in the cortex, while there was no significant difference between the outer and inner cortex ( $19 \pm 5$  and  $17 \pm 3 \text{ mg kg}^{-1}$

respectively). For the red intensity in the DMG-stained roots from the control soil, there was no significant difference between the cortex and the stele; however, they had significantly higher red intensities than the background (Figure 4.5d). There was more Ni in the resin (background) of the Ni-spiked soil than in the control soil ( $5 \pm 2$  and  $27 \pm 22$  mg kg<sup>-1</sup> respectively). This was probably due to Ni in the soil particles attached to the roots.

#### **4.4.5 Comparison of LA-ICP-MS with ICP-OES and XRF results**

Table 4.1 summarizes the results of the elemental analysis of the soil and roots using XRF and ICP-OES and compares them to the concentrations determined from the LA-ICP-MS. The values obtained by LA-ICP-MS, were weighted by the area contribution of each tissue to the root cross-section area. The values given for soil represent average concentrations along the scan lines outside of the root area. . There was no significant difference (ANOVA at 0.05 level) between the Ni values for control soil measured by the three different techniques. However the root ICP-OES results were extremely variable ( $29.2 \pm 27$ ), which could be due to unsatisfactory separation of soil particles from the roots prior to the digestion. Contradictory to the control samples, there was poorer agreement among the three techniques in measuring the Ni values of the Ni-spiked samples. There was no significant difference between the LA-ICP-MS and the ICP-OES values for the Ni-spiked root (ANOVA at 0.05 level), however the LA-ICP-MS values for the Ni-spiked soil were significantly larger than the XRF value. For Fe, the LA-ICP-MS technique always gave significantly smaller values than the other techniques. Interferences by the carrier gas (e.g. Argon), which is common in LA-ICP-MS analysis, might explain this differences. In case of the root, this may be due to incomplete separation of soil particles from the roots, so that soil particles may have been digested with the root samples for measurement with ICP-OES. The LA-ICP-MS values for Fe inside the roots were low. For both Mg and Ca, the LA-ICP-MS analysis gave significantly higher values than the other two techniques. This may be because the signal intensity of the internal standard, Ca, was more heterogeneous in the soil than in the root cross-section.

### **4.5 Discussion**

We obtained a similar pattern of Ni distribution in the root tissue using two independent techniques. This indicates that either redistribution did not greatly affect our results, or the redistribution was the same for both methods (unlikely). Bhatia et al. (2004) reported that DMG application lead to Ni redistribution inside the plant tissue. The staining procedure

they used involved soaking the plant tissue in DMG solution (1% solution in 95% ethanol) over night. Ethanol is very damaging to the tissue and increases the risk of Ni redistribution especially if applied for a rather long time. Our procedure included no ethanol and the time given to the DMG solution to react with Ni in the tissue was less than half a minute until the image was taken (Gramlich *et al.*, 2007). Therefore, we could reduce the redistribution risk to a degree that was found insignificant at the tissue level.

LA-ICP-MS method provided semi-quantitative data on the distribution of metals within the root cross-sections of *Berkheya coddii*. The spatial resolution of the data was sufficient for root studies at tissue level. The laser scan lines had a width of 75  $\mu\text{m}$  and a readout speed of 5  $\mu\text{m s}^{-1}$ ; which gave a resolution of 75 x 5  $\mu\text{m}$ . The spatial resolution was fine in the direction of the line scan, but coarse in the perpendicular direction because of the scan width. The resolution could be improved by choosing a narrower scan line width. Staining the root cross-section with DMG revealed a similar pattern of Ni distribution in the root cross-sections (compare Figures 4.1 and 4.2). Although the DMG-staining had a higher spatial resolution in all directions than LA-ICP-MS, it provided only qualitative information. Both techniques showed that the Ni concentration was higher in the cortex of roots grown in Ni-spiked soil than in the stele. None of these methods provided information regarding the chemistry of Ni in the root tissues. We assume that the measured Ni concentrations represent total Ni concentration. The DMG-staining experiment revealed that the Ni was mainly concentrated in the apoplastic area than in the cytoplasm, as supported by Gramlich *et al.* (2007) as well. This information could not be obtained by LA-ICP-MS because of the spatial resolution we chose and the physical shrinkage of the tissue that resulted from the sample preparation.

Presence of Ni in the rhizosphere, free movement in the apoplastic pathway and mass flow of water can explain high concentration of Ni in the cortex. Considering the Ni content of ultramafic soils, where *Berkheya coddii* is native (Morrey *et al.*, 1992), this is likely to be the case in its native environment. On the other hand, Ni concentration was found to be higher in the stele than in the cortex of the roots in control soil with low Ni concentration. The difference in Ni concentration of cortex and stele indicates active uptake or at least a selection mechanism for Ni ions in the latter case, since the uptake occurred against the concentration gradient. Therefore, nickel needs to pass through ion pumps or selective channels, which requires metabolic energy.

## 4.6 Conclusions

Quantitative two-dimensional Ni distribution pattern in the root cross-sections of the Ni hyperaccumulator plant *Berkheya coddii* obtained using LA-ICP-MS method was supported qualitatively by DMG-staining technique. Obtaining similar Ni distribution patterns using two independent methods indicates that the possible artefacts due to redistribution of Ni within the root tissue during sample preparation were inconsequence. Although a destructive method, LA-ICP-MS can measure simultaneous concentrations of elements with a spatial resolution well suited to tissue analysis. DMG-staining was a fast and low-cost method for qualitative studying of Ni in plant tissues. Both methods, LA-ICP-MS and DMG-staining, showed a greater concentration of Ni in the cortex of the Ni-spiked roots than in the stele, while the opposite pattern was observed for the control roots. A better understanding of the Ni concentration gradient in the rhizosphere of *Berkheya coddii* could unravel more information regarding uptake of Ni and its distribution inside the roots.

#### **4.7 Acknowledgements**

We would like to thank Jakob Frommer for his technical help for embedding and preparing the root samples. This study was funded by the Swiss National Science Foundation.

#### **4.8 References**

- Angle, J.S., Chaney, R.L., Baker, A.J.M., Li, Y., Reeves, R., Volk, V., Roseberg, R., Brewer, E., Burke, S. & Nelkin, J. 2001. Developing commercial phytoextraction technologies: practical considerations. *South African Journal of Science*, **97**, 619-623.
- Berazain, R., de la Fuente, V., Rufo, L., Rodriguez, N., Amils, R., Diez-Garretas, B., Sanchez-Mata, D. & Asensi, A. 2007. Nickel localization in tissues of different hyperaccumulator species of Euphorbiaceae from ultramafic areas of Cuba. *Plant and Soil*, **293**, 99-106.
- Bhatia, N.P., Walsh, K.B., Orlic, I., Siegele, R., Ashwath, N. & Baker, A.J.M. 2004. Studies on spatial distribution of nickel in leaves and stems of the metal hyperaccumulator *Stackhousia tryonii* using nuclear microprobe (micro-PIXE) and EDXS techniques. *Functional Plant Biology*, **31**, 1061-1074.
- Brooks, R.R., Chambers, M.F., Nicks, L.J. & Robinson, B.H. 1998. Phytomining. *Trends in Plant Science*, **3**, 359-362.

- Brooks, R.R., Lee, J., Reeves, R.D. & Jaffre, T. 1977. Detection of Nickeliferous Rocks by Analysis of Herbarium Specimens of Indicator Plants. *Journal of Geochemical Exploration*, **7**, 49-57.
- Budka, D., Mesjasz-Przybylowicz, J. & Przybylowicz, W.J. 2004. Micro-PIXE analysis: importance of biological sample preparation techniques. *Radiation Physics and Chemistry*, **71**, 785-786.
- Budka, D., Mesjasz-Przybylowicz, J., Tylko, G. & Przybylowicz, W.J. 2005. Freeze-substitution methods for Ni localization and quantitative analysis in *Berkheya coddii* leaves by means of PIXE. *Nuclear Instruments & Methods in Physics Research Section B-Beam Interactions with Materials and Atoms*, **231**, 338-344.
- Cromwell, E.F. & Arrowsmith, P. 1995. Semiquantitative Analysis with Laser-Ablation Inductively-Coupled Plasma-Mass Spectrometry. *Analytical Chemistry*, **67**, 131-138.
- de la Fuente, V., Rodriguez, N., Diez-Garretas, B., Rufo, L., Asensi, A. & Amils, R. 2007. Nickel distribution in the hyperaccumulator *Alyssum serpyllifolium* Desf. spp. from the Iberian Peninsula. *Plant Biosystems*, **141**, 170-180.
- Dessureault-Romppe, J., Nowack, B., Schulin, R. & Luster, J. 2006. Modified micro suction cup/rhizobox approach for the in-situ detection of organic acids in rhizosphere soil solution. *Plant and Soil*, **286**, 99-107.
- Gramlich, A.M., Moradi, A.B., Robinson, B.H., Kaesner, A. & Schulin, R. 2007. The semi-quantitative distribution of Ni in plant tissues using DMG staining and image processing. *Submitted to the Journal of Structural Biology*.
- Hattendorf, B., Latkoczy, C. & Gunther, D. 2003. Laser ablation-ICPMS. *Analytical Chemistry*, **75**, 341A-347A.
- Heath, S.M., Southworth, D. & Dallura, J.A. 1997. Localization of nickel in epidermal subsidiary cells of leaves of *Thlaspi montanum* var *siskiyouense* (Brassicaceae) using energy-dispersive x-ray microanalysis. *International Journal of Plant Sciences*, **158**, 184-188.
- Hoffmann, E., Ludke, C., Skole, J., Stephanowitz, H., Ullrich, E. & Colditz, D. 2000. Spatial determination of elements in green leaves of oak trees (*Quercus robur*) by laser ablation-ICP-MS. *Fresenius Journal of Analytical Chemistry*, **367**, 579-585.
- Jain, A. 1989. *Fundamentals of digital image processing*. Englewood Cliffs, NJ : Prentice Hall.

- Kramer, U., CotterHowells, J.D., Charnock, J.M., Baker, A.J.M. & Smith, J.A.C. 1996. Free histidine as a metal chelator in plants that accumulate nickel. *Nature*, **379**, 635-638.
- Kylander, M.E., Weiss, D.J., Jeffries, T.E., Kober, B., Dolgoplova, A., Garcia-Sanchez, R. & Coles, B.J. 2007. A rapid and reliable method for Pb isotopic analysis of peat and lichens by laser ablation-quadrupole-inductively coupled plasma-mass spectrometry for biomonitoring and sample screening. *Analytica Chimica Acta*, **582**, 116-124.
- Li, Y.M., Chaney, R., Brewer, E., Roseberg, R., Angle, J.S., Baker, A., Reeves, R. & Nelkin, J. 2003. Development of a technology for commercial phytoextraction of nickel: economic and technical considerations. *Plant and Soil*, **249**, 107-115.
- Longerich, H.P., Jackson, S.E. & Gunther, D. 1996. Laser ablation inductively coupled plasma mass spectrometric transient signal data acquisition and analyte concentration calculation. *Journal of Analytical Atomic Spectrometry*, **11**, 899-904.
- Longerich, H.P., Jackson, S.E. & Gunther, D. 1997. Laser ablation inductively coupled plasma mass spectrometric transient signal data acquisition and analyte concentration calculation (vol 11, pg 899, 1996). *Journal of Analytical Atomic Spectrometry*, **12**, 391-391.
- Mesjasz-Przybylowicz, J., Przybylowicz, W.J. & Pineda, C.A. 2001. Nuclear microprobe studies of elemental distribution in apical leaves of the Ni hyperaccumulator *Berkheya coddii*. *South African Journal of Science*, **97**, 591-593.
- Mizuno, N., Nosaka, S., Mizuno, T., Horie, K. & Obata, H. 2003. Distribution of Ni and Zn in the leaves of *Thlaspi japonicum* growing on ultramafic soil. *Soil Science and Plant Nutrition*, **49**, 93-97.
- Morrey, D.R., Balkwill, K., Balkwill, M.J. & Williamson, S. 1992. A review of some studies of the serpentine flora of Southern Africa. In: *The Vegetation of ultramafic (serpentine) soils* (eds. Baker, A.J.M., Procter, J. & Reeves, R.D.), pp. 147–158. Intercept. Andover.
- Motelica-Hieno, M. & Donard, O.F.X. 2001. Comparison of UV and IR laser ablation ICP-MS on silicate reference materials and implementation of normalisation factors for quantitative measurements. *Geostandards Newsletter-the Journal of Geostandards and Geoanalysis*, **25**, 345-359.
- Polatajko, A., Azzolini, M., Feldmann, I., Stuezel, T. & Jakubowski, N. 2007. Laser ablation-ICP-MS assay development for detecting Cd- and Zn-binding proteins in Cd-exposed *Spinacia oleracea* L. *Journal of Analytical Atomic Spectrometry*, **22**, 878-887.

- Prohaska, T., Stadlbauer, C., Wimmer, R., Stingeder, G., Latkoczy, C., Hoffmann, E. & Stephanowitz, H. 1998. Investigation of element variability in tree rings of young Norway spruce by laser-ablation-ICPMS. *Science of the Total Environment*, **219**, 29-39.
- Przybylowicz, W.J., Mesjasz-Przybylowicz, J., Pineda, C.A., Churms, C.L., Ryan, C.G., Prozesky, V.M., Frei, R., Slabbert, J.P., Padayachee, J. & Reimold, W.U. 2001. Elemental mapping using proton-induced x-rays. *X-Ray Spectrometry*, **30**, 156-163.
- Resano, M., Perez-Arantegui, J., Garcia-Ruiz, E. & Vanhaecke, F. 2005. Laser ablation-inductively coupled plasma mass spectrometry for the fast and direct characterization of antique glazed ceramics. *Journal of Analytical Atomic Spectrometry*, **20**, 508-514.
- Robinson, B.H., Brooks, R.R., Howes, A.W., Kirkman, J.H. & Gregg, P.E.H. 1997. The potential of the high-biomass nickel hyperaccumulator *Berkheya coddii* for phytoremediation and phytomining. *Journal of Geochemical Exploration*, **60**, 115-126.
- Robinson, B.H., Lombi, E., Zhao, F.J. & McGrath, S.P. 2003. Uptake and distribution of nickel and other metals in the hyperaccumulator *Berkheya coddii*. *New Phytologist*, **158**, 279-285.
- Russo, R.E., Mao, X.L., Liu, H.C., Gonzalez, J. & Mao, S.S. 2002. Laser ablation in analytical chemistry - a review. *Talanta*, **57**, 425-451.
- Tappero, R., Peltier, E., Grafe, M., Heidel, K., Ginder-Vogel, M., Livi, K.J.T., Rivers, M.L., Marcus, M.A., Chaney, R.L. & Sparks, D.L. 2007. Hyperaccumulator *Alyssum murale* relies on a different metal storage mechanism for cobalt than for nickel. *New Phytologist*, **175**, 641-654.
- Tinker, P.B. & Nye, P.H. 2000. *Solute movement in the rhizosphere*. New York : Oxford University Press.
- Ulrich, A., Barrelet, T. & Krahenbuhl, U. 2007. Spatially resolved plant physiological analysis using LA-HR-ICP-MS. *Chimia*, **61**, 111-111.

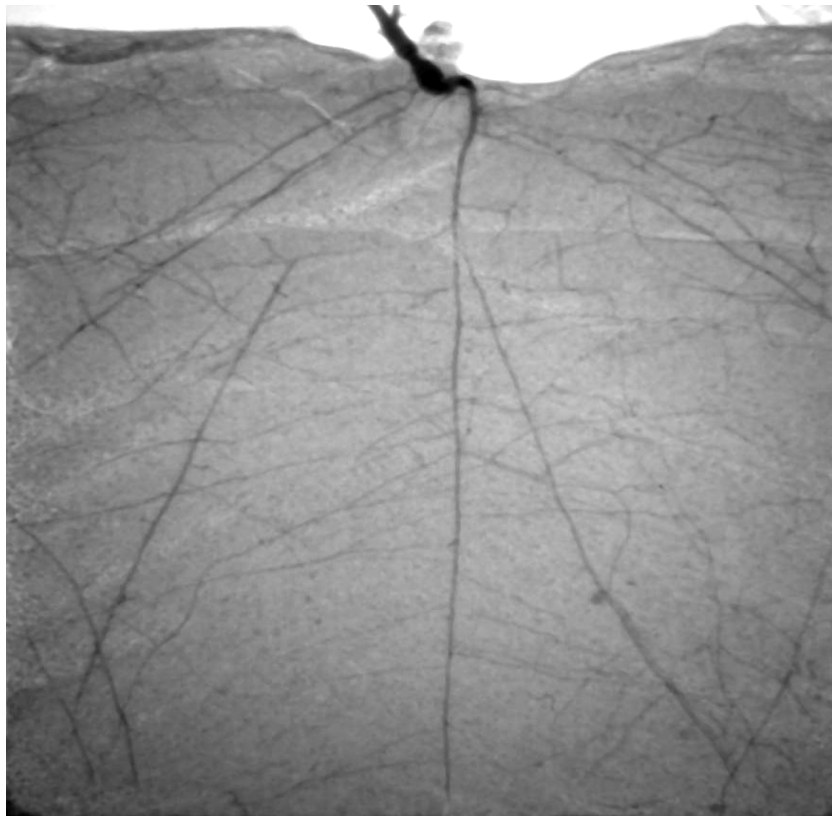
---

## **5 Neutron radiography as a tool for revealing root development in soil: capabilities and limitations**

---

*Ahmad B. Moradi, Héctor M. Conesa, Brett Robinson, Eberhard Lehmann, Guido Kuehne,  
Anders Kaestner, Sascha Oswald, Rainer Schulin*

*Submitted for publication in Plant and Soil*



## 5.1 Abstract

Neutron Radiography (NR) is a valuable non-invasive tool to study in situ root development in soil. However, there is a lacuna of quantitative information on its capabilities and limitations. We combined neutron radiography with image analysis techniques to quantify the neutron absorption coefficients ( $\Sigma$ ) of various root-growth media for a range of water contents ( $\theta$ ) in the presence and absence of plant roots. Three different plant species with different rooting systems were grown in aluminium containers (150 x 150 x 12 mm) and were imaged using NR, as well as X-ray radiography and an optical scanner in order to assess and compare NR capabilities in detecting roots with other methods. Sandy soil was the best medium for NR because it supported plant growth at  $\theta$  that gave a good contrast for root visualisation. After correction for neutron scattering, we obtained a linear correlation between  $\Sigma$  and soil  $\theta$ . The minimum detectable root thickness in neutron radiographs was found to be 0.2 mm in these containers. Combining NR with X-Ray radiography could provide information on soil structure in addition to revealing root structure and development.

**Key words:** neutron radiography, neutron attenuation coefficient, neutron scattering, plant roots, soil water content, X-ray radiography

## 5.2 Introduction

Neutron Radiography (NR) is one of the few non-destructive techniques available to image living plant roots in situ (Menon *et al.*, 2007). Roots grow in a heterogeneous, porous, semi-compressible medium compound of solid, liquid and gaseous phases, known as soil. It is difficult to observe tightly enmeshed roots in an opaque soil matrix without disturbance. Better understanding of root behaviour in heterogeneous soil, requires efficient non-invasive techniques to analyze root and soil structure in situ (Whalley *et al.*, 2000; Fitz *et al.*, 2005; Pierret *et al.*, 2005).

Current non-invasive and non-destructive methods for studying roots include minirhizotrons which are transparent plastic tubes inserted into the ground to view the roots using a camera (Kuchenbuch & Ingram, 2002), magnetic resonance imaging (Bottomley *et al.*, 1993; Doussan *et al.*, 2003; Heyes & Clark, 2003), neutron radiography and tomography (Willatt *et al.*, 1978; Willatt & Struss, 1979; Bois & Couchat, 1983; Nakanishi *et al.*, 2005; Menon *et al.*, 2007) as well as X-Ray imaging and tomography (Moran *et al.*, 2000; Naftel *et al.*, 2001; Gregory *et al.*, 2003). Root observation using minirhizotrons is non-destructive. However, they have an invasive component that may perturb root development and water flux (Majdi, 1996). Ferromagnetic materials hinder magnetic resonance imaging (Hall *et al.*, 1997), thus limiting this technique to carefully selected media such as pre-treated sand and soil, agar, and glass beads. NR provides images similar to X-Ray radiography. Neutrons interact with the nuclei of atoms while X-Rays interact with electrons. Whereas X-Ray attenuation depends on element's atomic number  $Z$ , the neutron attenuation coefficient is independent of  $Z$  and only a few elements such as hydrogen strongly attenuate neutrons. Therefore, H-rich, organic materials and water are clearly visible in neutron radiographs, while many soil components and structural materials such as Si, Ca and Al are nearly transparent. This permits *in situ* investigations of specimens housed in various types of experimental apparatus. Such housings often impair or prevent X-Ray imaging because of their high X-Ray cross sections. However the neutron cross section of these elements is moderately low, allowing the neutrons to pass through undisturbed.

NR is a valuable tool for studying root behaviour in soil since the difference in gravimetric water content ( $\theta$ ) of roots and the surrounding soil provides enough contrast to visualize the roots. Nakanishi *et al.* (2005) showed how soil  $\theta$  changes along a vertical distance from the root surface using thermal neutron beam analysis. Microscopic movement of water around the roots of soybean seedlings was studied by Furukawa *et al.* (1999). Menon *et al.* (2007) visualized the root growth of lupin plants over a period of 3 weeks and revealed how

heterogeneous soil can affect root growth. Fine roots (< 2mm) are particularly important for the uptake of water and nutrient by plants (Sutton & Tinus, 1983; Waisel *et al.*, 2002). While it is widely recognized that the total length of the fine roots is generally larger than that of the coarse roots of a plant, it is also acknowledged that the amount of fine roots is often underestimated because of the lack of reliable measurement techniques, their small size and near transparency (Vogt *et al.*, 1998; Costa *et al.*, 2001; Pierret *et al.*, 2003). Root visibility in NR is proportional to root thickness and inversely proportional to soil moisture content (Furukawa *et al.*, 1999; Nakanishi *et al.*, 2003; Matsushima *et al.*, 2005; Nakanishi *et al.*, 2005; Menon *et al.*, 2007). These authors used either thin containers ( as thin as 2 mm) or artificial plant growth media (quartz sand or silt). There is a lacuna of information on the performance of NR in other systems, for example with topsoils, and more realistic growing containers. The effects of root thickness, soil type and the water content of the surrounding soil on the contrast between soil and roots in NR images has not been quantified and the capability of NR has not yet been evaluated in visualizing fine roots with various thickness in various soil types and water contents.

The quantitative analysis of a neutron radiograph requires corrections for interactions between neutron beam and the sample other than adsorption, which can be significant. These types of interactions can be coherent, incoherent, elastic and inelastic scattering. Calibrating of the  $\theta$  against neutron transmission usually may not give a satisfactory result, especially at higher  $\theta$  where transmission decreases and multiple neutron scattering becomes important leading to a considerable deviation from the exponential law of attenuation (Hassanein, 2006). While neutron scattering is used to measure various properties of materials (Bailey, 2003), it needs to be corrected for studying water and hydrogen rich organic materials, such as roots, in soil.

We aimed to assess the capabilities and limitations of NR combined with image analysis tools for studying non-destructively root development in soil with particular attention to the quantitative effects of neutron scattering, soil type, soil  $\theta$  and root thickness on the root visibility in soil. Specifically, we sought to quantify the effects of soil type, soil moisture, and container dimensions and size on the ability to visualise roots and determine the detection limits for NR under realistic conditions for plant growth. Furthermore, we aimed to develop NR as a tool to quantify the water content of soil in the rhizosphere.

## **5.3 Materials and methods**

### **5.3.1 Neutron and X-ray radiography systems**

The Beer-Lambert law describes the attenuation of both neutron and X-ray (Kasperl & Vontobel, 2005) , assuming that the neutron detector records only the uncollided flux component and that the neutrons are mono-energetic or have a small wavelength bandwidth:

$$I = I_0 \cdot e^{-\Sigma d} \quad (\text{Eq. 1})$$

where  $I$  is the detected neutron flux ( $\text{cm}^{-2} \text{s}^{-1}$ ) after an incident neutron flux,  $I_0$ , passes through material of thickness  $d$  (cm) with a neutron attenuation coefficient of  $\Sigma$  ( $\text{cm}^{-1}$ ), which is a bulk physical property of the material. The material may be crystalline, polymorphic, or, as in our case, a porous media.

*Table 5.1: Physical properties of the plant-growth media used for neutron radiography*

	Particle size (mm)	Bulk density ( $\text{g cm}^{-3}$ )	Porosity (% v/v)	Water holding capacity at 1 bar ( $\text{cm}^3/\text{cm}^3$ )	Provenience
Perlite	<2	0.125	97	0.91	Samen Mauser, Switzerland
Porous glass beads	1.5 2.5	0.49	71	0.16	Schott, Germany
Mine tailing soil	<2	1.4	35	0.08	Southeast, Spain
Loamy soil	<2	1.2	49	0.17	Mattenweg, Switzerland
Organic soil	<2	0.58	88	0.09	Migros, Switzerland
Sandy soil	<2	1.3	36	0.09	Eiken, Switzerland
Fine quartz sand	0.1-0.7	1.5	19	0.01	Carlo, Switzerland
Coarse quartz sand	0.7-1.5	1.45	26	0.01	Carlo, Switzerland

The experiments were performed at the neutron and X-ray radiography facilities at Paul Scherrer Institut (PSI), Villigen, Switzerland. The PSI has two neutron imaging facilities in operation; NEUTRA for thermal neutrons (Lehmann *et al.*, 1999), and ICON for imaging with cold neutrons (Kuhne *et al.*, 2005). Both facilities consist of the neutron source (the spallation neutron source SINQ), a special collimator, and a two-dimensional image detector. The neutron-generating source is based on the spallation principle in a lead (Pb) target that is bombarded with high-energy protons (590 MeV). Scattering processes in a heavy water moderator slow down the high-energy neutrons that are produced by the decay of Pb nuclei, until they reach thermal equilibrium with the heavy water. For a thermal spectrum, the moderator is kept at about room temperature ( $\sim 300$  K), which yields neutron energies of around 25 meV and velocities of around 2200 m/s. For a cold spectrum, liquid deuterium is used as an additional moderator at around 25° K, yielding neutron energies of around 5.7 meV and velocities of about 1000 m/s. The collimator is a beam-forming assembly that determines the geometric properties of the beam and contains filters that reduce the intensity of accompanying gamma rays. The image resolution depends on the collimator geometry and is expressed by the collimation ratio  $L/D$ , where  $L$  is the collimator length and  $D$  is the diameter of the inlet aperture of the collimator on the side facing the source. In our study, a neutron flux of  $4.2 \times 10^6 \text{ cm}^{-2} \text{ s}^{-1}$  with a mean energy of 25 meV and a collimation ratio of  $L/D = 550$ , was used for NEUTRA while for ICON a neutron flux of  $2.8 \times 10^6 \text{ cm}^{-2} \text{ s}^{-1}$ , a mean energy of 5.7 meV, and a collimation ratio of  $L/D = 605$ . The beam was transmitted through the sample and an area position-sensitive detector recorded the resulting image, which is integrated in the beam direction over the thickness,  $d$ . This detector records a two-dimensional image that is a projection of the object on the detector plane. We used a CCD camera detector with an array of  $1024 \times 1024$  pixels in conjunction with a neutron-sensitive  $^6\text{Li}$  based scintillator screen (Applied scintillation technologies, UK), giving a resolution of 110-170  $\mu\text{m}$  in the digital images.

The X-ray radiography facility at PSI consists of an X-ray tube with a maximal voltage of 320 kV. Using the focal spot at the tungsten target of about 3 mm, which corresponds to arrangement of the tube just in front of the outer collimator close to the target block wall, we obtained about the same  $L/D$  ratio as with the neutron beam. The X-ray tube delivered a continuous energy spectrum of photons up to a voltage limit, at which the mean photon energy was about half of that voltage value (e.g. 160 keV). Although the distance between the source and the CCD detector was relatively high (about 7 m), the intensity of the beam

was high enough to enable transmission images within a few seconds, comparable to the neutron conditions. A scintillator screen made of Gadolinium-oxy-sulfide (Gadox) was used for X-ray imaging.

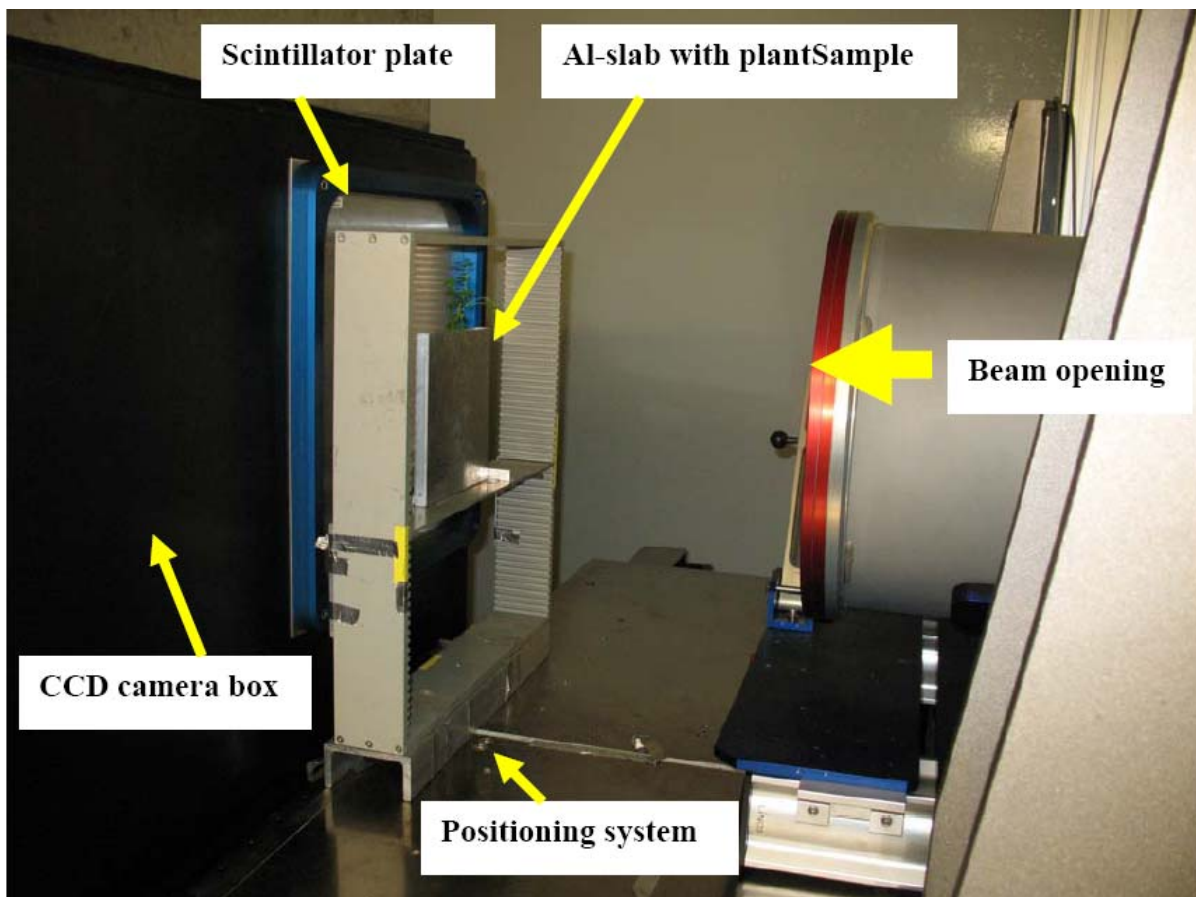


*Figure 5.1: The cold-neutron imaging set-up (ICON) at PSI*

### **5.3.2 Materials testing**

We chose a variety of materials that could be potentially used as root growth media (Table 5.1). The materials were air-dried and packed into the plant growth containers and were imaged the same way as the plant roots. We used containers with inner dimensions of 0.17 x 0.15 x 0.012 m. The containers were made of aluminum because of its low neutron attenuation and therefore high transparency.

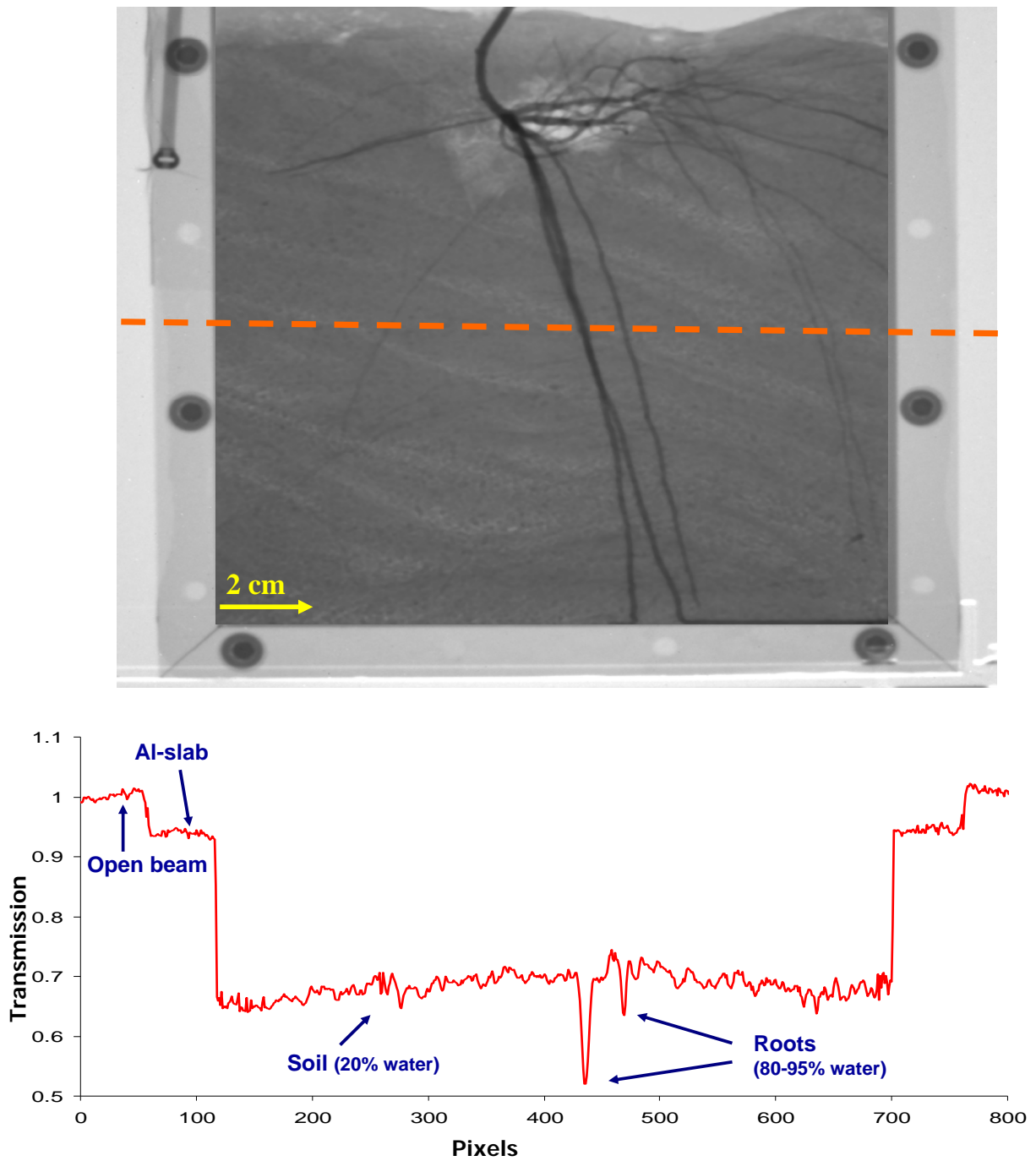


Figure 5.2: Neutron radiograph of *Berkheya coddii* roots in an aluminium container filled with soil. The graph shows the transmission values of the pixels along the cross-section in the image.

### 5.3.3 Calibration for soil water content

The NR image is a projection of the object (in our case a container with a thickness of 12 mm) in the direction of the container thickness. Thus both soil water and water residing in the roots contribute to the neutron attenuation coefficients calculated pixel-wise in each image. The contrast in the NR images comes from difference in water content of the roots and the surrounding soil. Calibrating neutron attenuation coefficients against soil water is needed to calculate the contribution of root water to the  $\Sigma$ , knowing the root diameter. To calibrate neutron transmission and  $\Sigma$  against soil  $\theta$ , three containers were filled with the sandy soil (Table 5.1) in the same way as described above. The soils were saturated with water, then left to dry for 2 weeks at room temperature by opening one side of the container. The containers were imaged seven times during the drying period. Before each imaging, the total water content of the soil was measured gravimetrically.

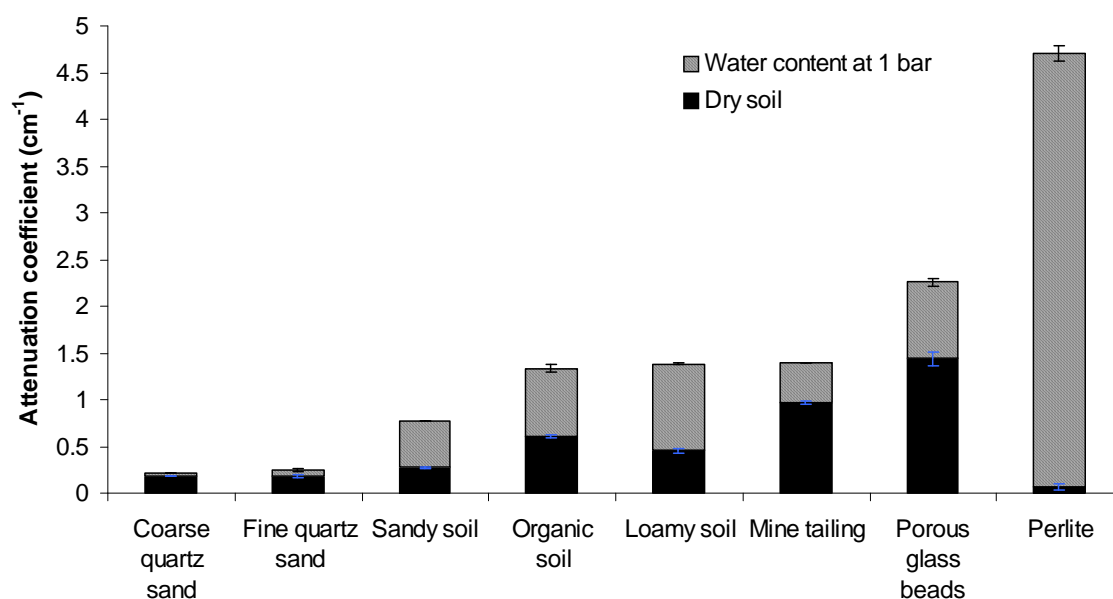


Figure 5.3: Cold-neutron attenuation coefficients of various root-growth materials, both dry and with a water content in equilibrium with -1 bar.

### 5.3.4 Plant growth

Three plant species, with three different rooting systems were selected for this study; garden tomato (*Lycopersicon esculentum* Mill.) with a fibrous root system of fine roots,

chickpea (*Cicer arietinum* L.) with strong tap root system and *Berkheya coddii* Roessl with a fibrous root system of both fine and coarse roots. We filled 12 containers with the sandy loam described in Table 5.1. There were four treatments, each with three replicates: the three aforementioned plants and an unplanted treatment. The average bulk density of the packed soil was  $1.3 \text{ g cm}^{-3}$ . The seeds of the plants were sown directly onto the soil surface at the centre of the containers except for *Berkheya coddii*, where seedlings were transplanted into the containers. The plants were grown for 7 weeks before the imaging in a controlled environment chamber at 16-19°C and a daily photoperiod of 16 hours generated by fluorescent lighting ( $0.4 - 0.6 \text{ lumen cm}^{-2}$ ). Plants were irrigated with Hoagland's nutrient solution (Hoagland & Arnon, 1938) to maintain soil  $\theta$  of around 20%. Irrigation was stopped 3 days before imaging. Neutron and X-ray radiographs were taken on the same day. After imaging, we opened one side of the containers and scanned the soil surface using a conventional photo scanner with a pixel array of 2250 x 2250. Soil in the containers was subdivided into sections. Each section was weighted and the roots were carefully separated from the soil. The dry mass of the roots as well as the moisture content of the soil in each section were determined by weighing.

### 5.3.5 Imaging procedure

All containers were imaged in exactly the same position using an automated positioning table in front of the beam line with a distance of 10 cm from the scintillator plane in the ICON setup and 15 cm in the NEUTRA and X-ray setups (Figure 5.1). We used exposure times of 45, 15 and 10 seconds for ICON, NEUTRA and X-ray images respectively. These exposure times gave the best signal to noise ratio and therefore the best contrast between the roots and the soil. X-ray images used a voltage of 120 kV at 10 mA. To correct for spatial variations in beam intensity, we collected open beam images and dark current images. The field of view was 19 x 17 cm which left a margin (area without sample) of 1cm. This was used to normalise the images and to correct for any fluctuations in beam intensity.

### 5.3.6 Image analysis

The transmission images were first corrected for beam variation and camera noise using a flat field correction. The corrected image ( $I'$ ) was calculated as:

$$I' = f_{OB} \cdot \frac{I_{raw}^{(x,y)} - I_{dark}^{(x,y)}}{I_{OB}^{(x,y)} - I_{dark}^{(x,y)}} \quad (\text{Eq. 2})$$

where  $I_{raw}(x,y)$  is the raw image,  $I_{dark}(x,y)$  is the image with neither beam nor sample,  $I_{OB}(x,y)$  is the open beam image containing the spatial variation of the beam without the sample, and  $f_{OB}$  is a scaling factor. The calculations were performed pixelwise and  $x$  and  $y$  are the coordinates. The value for  $f_{OB}$  was chosen so that the mean transmission in the regions of the image without the sample was 1. Based on Eq. 1 the negative logarithm of the corrected image,  $I'(x,y)$ , yields the attenuation coefficient  $\Sigma(x,y)$  of the material summed over the sample thickness  $d$ . The corrected transmission image shows a consistent contrast between different substances in the image. For example, roots appear darker than the surrounding soil because of their lower transmission due to the higher  $\Sigma$ .

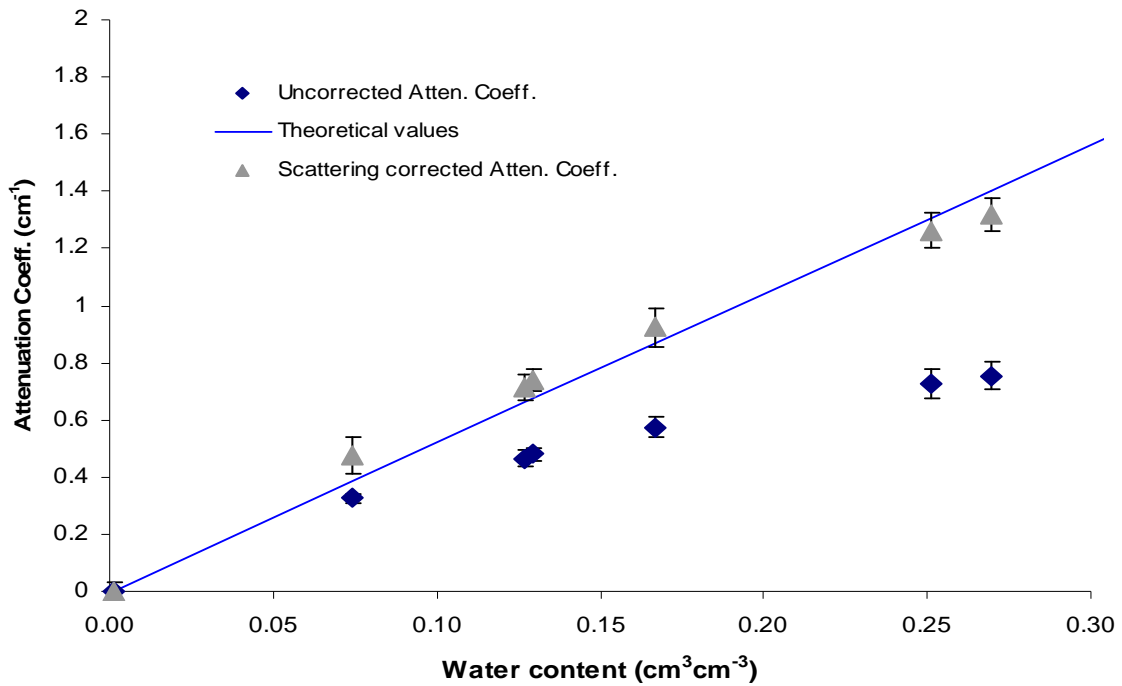


Figure 5.4: Cold-neutron attenuation coefficients of water in soil for a range of soil water contents. The scattering corrected and uncorrected attenuation coefficients are compared with the theoretical values. The error bars show standard deviation of the mean.

The distinction between absorbed and scattered neutrons is critical for quantitative NR analysis. Some scattered neutrons collide with the detector plate and thus cause deviations from the exponential law of attenuation (Eq. 1). The scattering component increases image intensity and may lead to an underestimation of the neutron attenuation or density of the materials. Surrounding objects, such as the camera box or neutron shielding can scatter neutrons into the detector. Since these neutrons would have otherwise missed the objective, the scattering causes an extra intensity. Hydrogen, the main neutron-opaque component of the root-soil system, scatters a relatively high number of neutrons. Further deviations from the exponential law of attenuation are due to beam hardening and the energy dependency of the detector efficiency. We used the Quantitative Neutron Imaging algorithm (QNI) to correct for scattering and beam hardening (Hassanein *et al.*, 2005). The correction is based on the iterative reconstruction of the measured image by overlapping point scattered functions calculated by means of Monte-Carlo simulation (Hassanein, 2006).

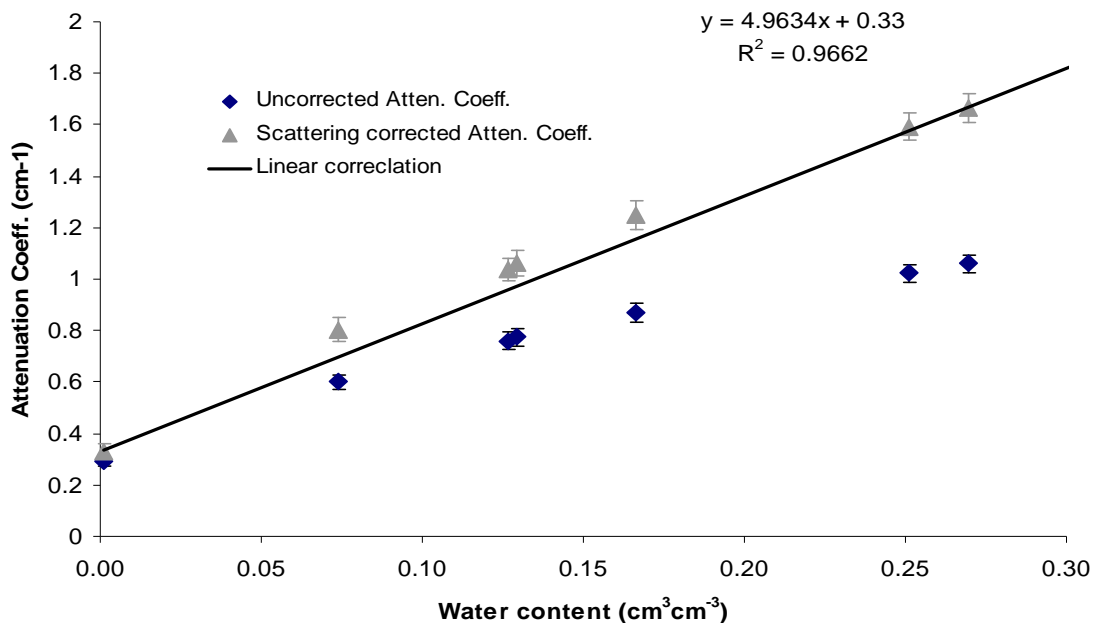


Figure 5.5: Scattering corrected and uncorrected total cold-neutron attenuation coefficients of water and soil materials for a range of soil water contents and a linear regression between the corrected attenuation coefficient and the soil water content ( $R^2 = 0.966$ , Pearson confidence level  $>0.99$ ). The error bars show standard deviation of the mean.

For samples compound of different substances; such as an aluminium container with soil, roots, and water, the total  $\Sigma$  is then sum of the individual components:

$$\Sigma_{total}(x,y) = (\Sigma_{Soil}(x,y) + \Sigma_{Aluminium}(x,y) + \Sigma_{Water}(x,y)) = \frac{\ln\left(\frac{I_0}{I}\right)}{d} \quad (\text{Eq. 3})$$

The component accounting for the water in the system,  $\Sigma_{water}$ , comprises both soil and root water. If the root thickness and the soil water content are known, the total  $\Sigma$  of water can be calculated from the water residing in the soil and water in the roots:

$$\Sigma_{Water} \cdot d = (\Sigma_{rootwater} \cdot x) + (\Sigma_{soilwater} \cdot (d - x)) \quad (\text{Eq.4})$$

where  $d$  is the container thickness filled with soil and  $x$  is the root thickness.

We used the same method as Menon et al (2007) for detecting root thickness and segmentation. All other calculations above apart from the neutron scattering correction were carried out using Matlab.

## 5.4 Results and discussions

### 5.4.1 Analysis of neutron radiographs

Figure 5.2 shows a NR image of a root system grown in an aluminium container filled with soil together with the transmission values along a cross-section through the image. There was a clear contrast between the soil and the roots, although the signal from the soil was heterogeneous due to the differences in the soil moisture content and the soil-filling patterns. Normalizing the image set a mean transmission value of 1 for the open beam area, while the sample area had different transmission based on its  $\Sigma$ . The aluminium frame of the container with a thickness of 16 mm absorbed only 5% of the incident neutrons resulting in a transmission value of 0.95. The aluminium side-walls of the container had a thickness of 3 mm and therefore a mean transmission value of 0.99. The contrast between the roots and the soil was due to their different  $\theta$ . While soil contains typically less than 50% water by mass (in our case 20%), the  $\theta$  of roots usually is in the range of 80-95%. Therefore, roots are best seen in soils with a low  $\theta$ , low intrinsic  $\Sigma$  (meaning low concentrations of high neutron-absorbing elements), and low heterogeneity.

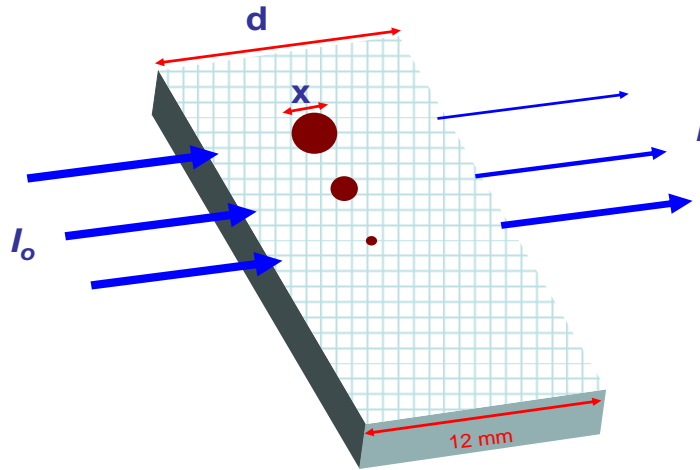


Figure 5.6: Effect of root thickness on the contrast between the attenuation coefficient of the roots and the surrounding soil. The thicker the roots are the more neutrons they absorb or scatter and the higher the contrast is to the surrounding soil in the 12 mm thick container.

#### 5.4.2 Factors affecting root contrast in NR

Figure 5.3 shows the cold-neutron  $\Sigma$  value of tested plant-growth media. The dry porous glass beads (Schott, Germany) used in this study had the highest  $\Sigma$  ( $1.44 \text{ cm}^{-1}$ ) and thus the lowest transmittance. This is because the glass beads contained high concentrations of boron, which strongly absorbs neutrons. Perlite gave the lowest  $\Sigma$  ( $0.07 \text{ cm}^{-1}$ ), which can be attributed to its low bulk density. In the sand and sandy-soils, the neutron absorption increased in proportion to the concentration of fine materials, in particular clay. The  $\Sigma$  increased in the sequence sand < sandy soil < loamy soil. The high attenuation neutrons in the organic soil and the mine tailings can be attributed to their high concentrations in hydrogen and iron, respectively.

For most plants, the optimal soil moisture for growth is between field capacity (ca -0.33 bars) and a water potential of -1 bar (Allen *et al.*, 1998). Reducing the soil  $\theta$  improves contrast. Therefore, the optimal soil moisture for imaging roots by NR is at a soil water potential at the dry end of this range (-1 bar). Plotting the  $\Sigma$  of the plant growth media containing their corresponding  $\theta$  at -1 bar changed the trend completely. While dry perlite had the lowest  $\Sigma$ , perlite had the highest  $\theta$  and therefore also the highest  $\Sigma$  at -1 bar (Table 5.1).

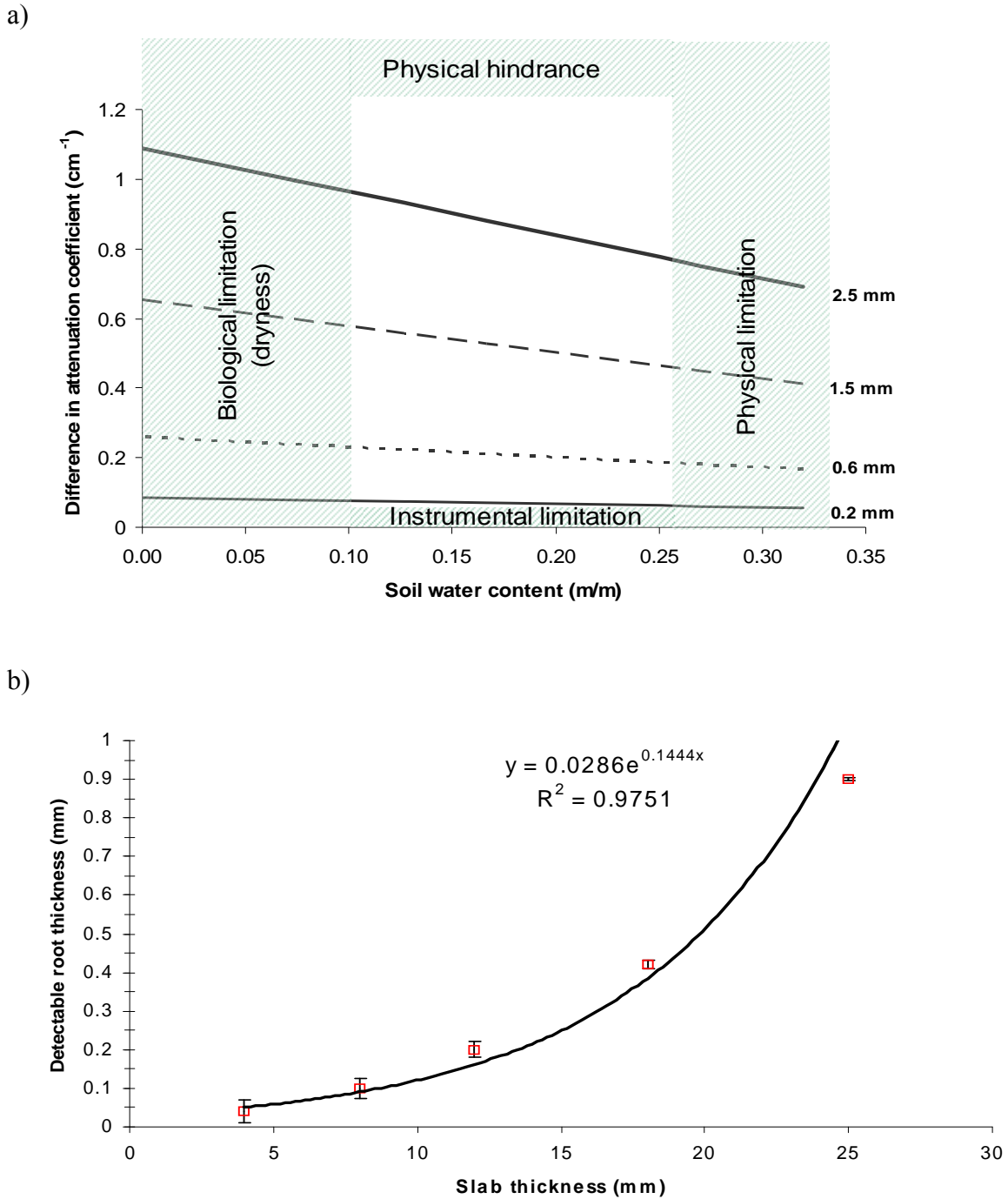


Figure 5.7: Calculated contrast in attenuation coefficient between roots of various thicknesses and surrounding soil as a function of water contents (a). The associated limitations are shown and minimum detectable root thicknesses are calculated for various container thicknesses (b). The error bars show the variation in detectable root thickness over the range of optimal water contents for root imaging ( $\theta = 0.12 - 0.18$ ).

An ideal plant growth medium for neutron imaging should provide enough contrast with roots, i.e. the lowest possible  $\Sigma$ , while providing a satisfactory environment for plant growth. The sandy soil was the best medium since it had a relatively low  $\Sigma$  and still supported plant growth without water stress. Although fine and coarse quartz sands had lower  $\Sigma$  than the sandy soil, mechanical resistance to root penetration due to high bulk density can be a problem for root growth (Menon *et al.*, 2007).

### 5.4.3 Relationship between $\Sigma$ and $\theta$

Figure 5.4 shows the cold-neutron  $\Sigma$  of water in soil over a range of soil  $\theta$ . The relationship between the uncorrected  $\Sigma$  became non-linear at soil  $\theta$  above 0.1, due to the decreasing slope of the curve, resulting in a loss of sensitivity. There was a 46% deviation from linearity at a soil  $\theta$  of 0.07 and an 80% deviation at a soil  $\theta$  of 0.25. Thus scattering had a large effect on radiographs taken within the range of soil  $\theta$  that are optimum for root growth in most of the soils. Correcting for neutron scattering, the neutron attenuation coefficient of soil water showed a linear relationship with the water content of the soil. This result was in good agreement with the theoretical values for the neutron attenuation coefficient of a water layer calculated from the exponential law of attenuation. A similar relationship was observed between the thermal-neutron  $\Sigma$  and soil  $\theta$ , except that the change of  $\Sigma$  over soil  $\theta$  and the slope of the curve were smaller than those obtained using cold neutrons (data not shown). The thermal-neutrons curve thus displayed lower sensitivity than the one for cold neutrons. Therefore we used the cold-neutron calibration curve for the rest of the analysis.

The total cold-neutron  $\Sigma$  (sum of soil and soil water  $\Sigma$ ) followed the same trend as the neutron  $\Sigma$  of water (Figure 5.5). The intercept was equal to the  $\Sigma$  of the dry soil ( $0.33 \text{ cm}^{-1}$ ). The relationship between the scattering-corrected total neutron  $\Sigma$  and soil  $\theta$  was linear ( $R^2 = 0.966$ , Pearson confidence level  $>0.99$ ). Such linearity greatly improves the reliability and sensitivity (up to 80%) of the calibration curve and simplifies the use of the calibration curve for relating water content to the attenuation coefficient which is crucial for quantitative analysis of roots and water distribution in soil by means of NR.

### 5.4.4 Root detection

The ease of root detection in neutron radiographs increases in proportion to their  $\theta$  and thickness. Coarser roots absorb or scatter more neutrons passing through the sample than

fine roots. Therefore they create a better contrast with the surrounding soil (Figure 5.6). Figure 5.7a shows the contrast between roots and the surrounding soil (difference in  $\Sigma$ ) for different root diameters over a range of soil  $\theta$ . These calculations are based on equations 3 and 4 assuming a container thickness of 12 mm and an average root  $\theta$  of 85%. Contrast increased with increasing root diameter and also with decreasing soil water content for each root diameter. The minimum diameter for root detection using our experimental setup was 0.2 mm. The pixel size of 110-170  $\mu\text{m}$  and background noise arising from soil heterogeneity prevented the detection of finer roots. Roots were detectable when there was at least a 10% difference in  $\Sigma$  to the surrounding soil. At lower differences in  $\Sigma$ , measurement errors and background noise from soil heterogeneity prevented quantification.

At a soil  $\theta$  below 0.1, the roots started dehydrating, which reduced contract and inhibited plant growth. The flux of transmitted neutrons decreased at a soil  $\theta$  above 0.25 due to high neutron scattering by soil water. This negatively affected the scattering correction and reduced contrast.

#### **5.4.5 Minimum detectable root diameter as a function of container thickness**

Our container had an inner width of 12 mm in the direction of the neutron beam in order to provide enough space for the roots to grow. Others have used root-growth boxes that varied in thickness from 6 mm to more than 30 mm (Furukawa *et al.*, 1999; Kuchenbuch & Ingram, 2002; Nakanishi *et al.*, 2003). Figure 5.7b shows how the minimum diameter of detectable roots depended on container thickness. This calculation was based on our results for the sandy soil using equations 3 and 4, assuming root  $\theta$  of 85%, a soil  $\theta$  of 0.12-0.18, a contrast threshold of 10% and no limitation in pixel size. With a container thickness of 4 mm, roots with a diameter of 0.04 mm could be resolved. The detectable root thickness increased exponentially with increasing the container width. With a container width of 25 mm, only roots thicker than 0.9 mm could be detected. The error bars show the variation in detectable root thickness over the range of optimal water contents for root imaging ( $\theta = 0.12 - 0.18$ ). As the container thickness increased, the error bars became smaller which means that the influence of soil  $\theta$  on root detection decreased

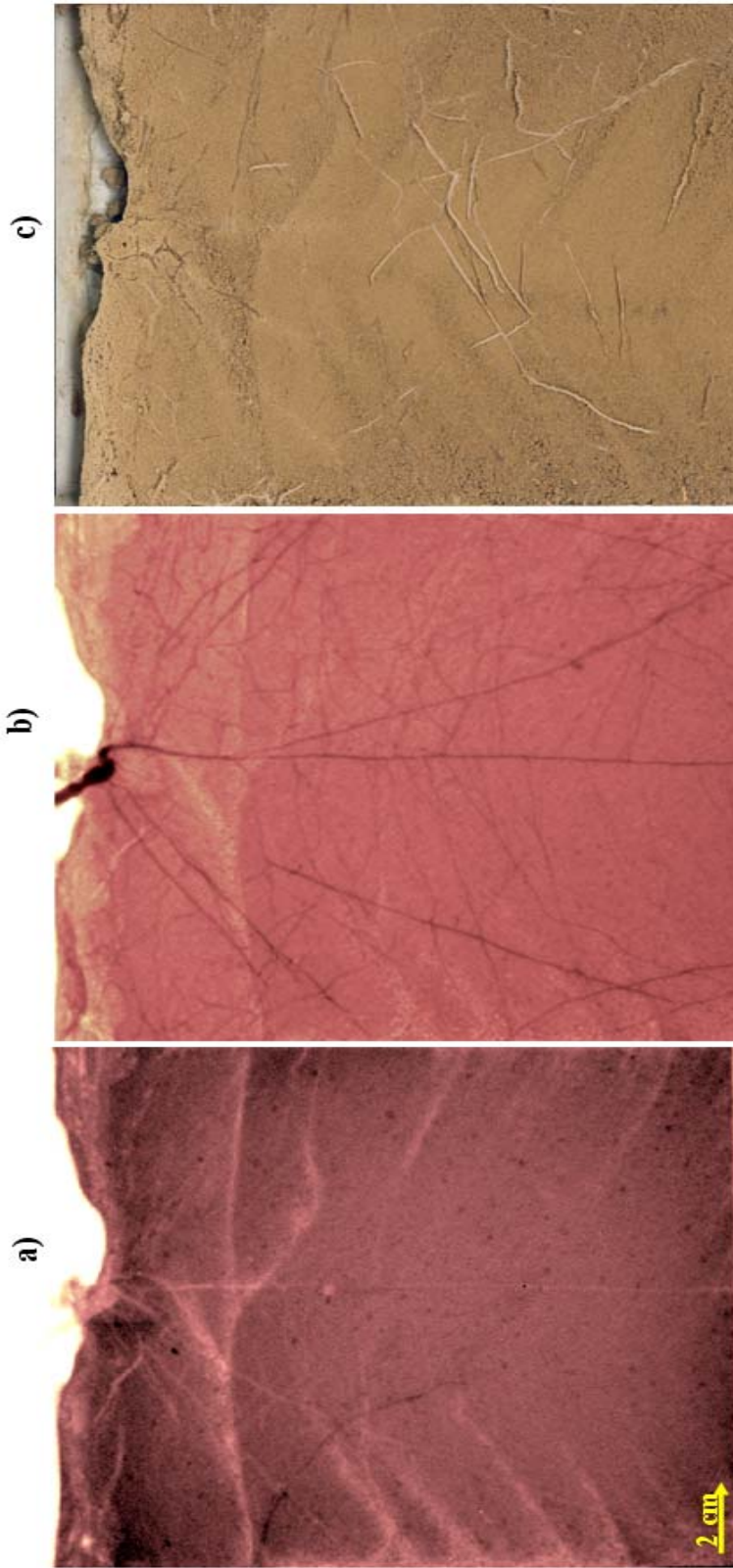


Figure 5.8: Comparison of X-ray (a), cold-neutron (b), and scan (c) images of a 7 weeks old chickpea (*Cicer arietinum* L.) plant taken on the same day. While the X-ray and scan image show only the main roots and the roots on the surface respectively, the neutron image reveals both fine roots and roots within the soil.

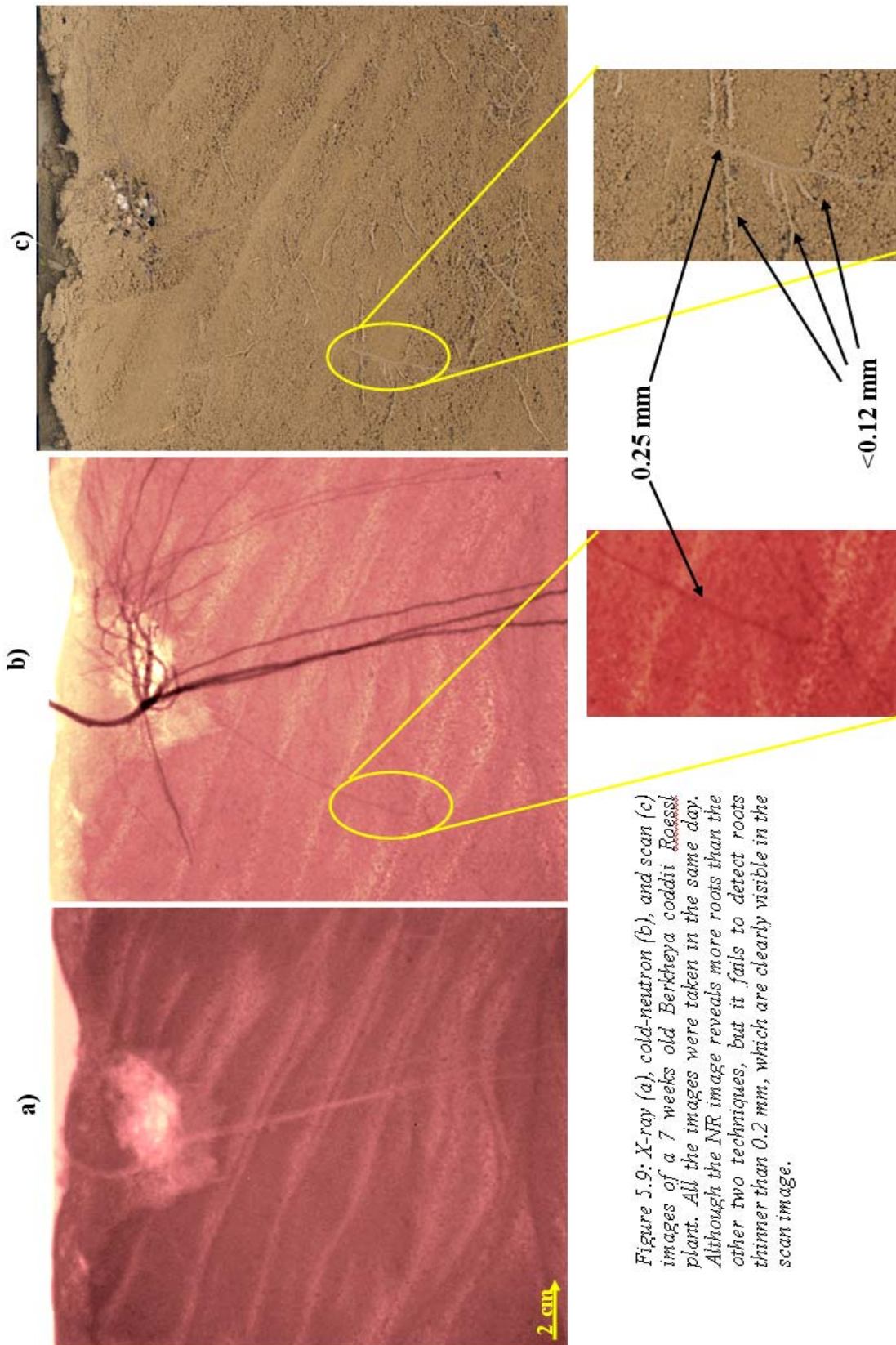


Figure 5.9: X-ray (a), cold-neutron (b), and scan (c) images of a 7 weeks old *Berkheya coddii* Roessler plant. All the images were taken in the same day. Although the NR image reveals more roots than the other two techniques, but it fails to detect roots thinner than 0.2 mm, which are clearly visible in the scan image.

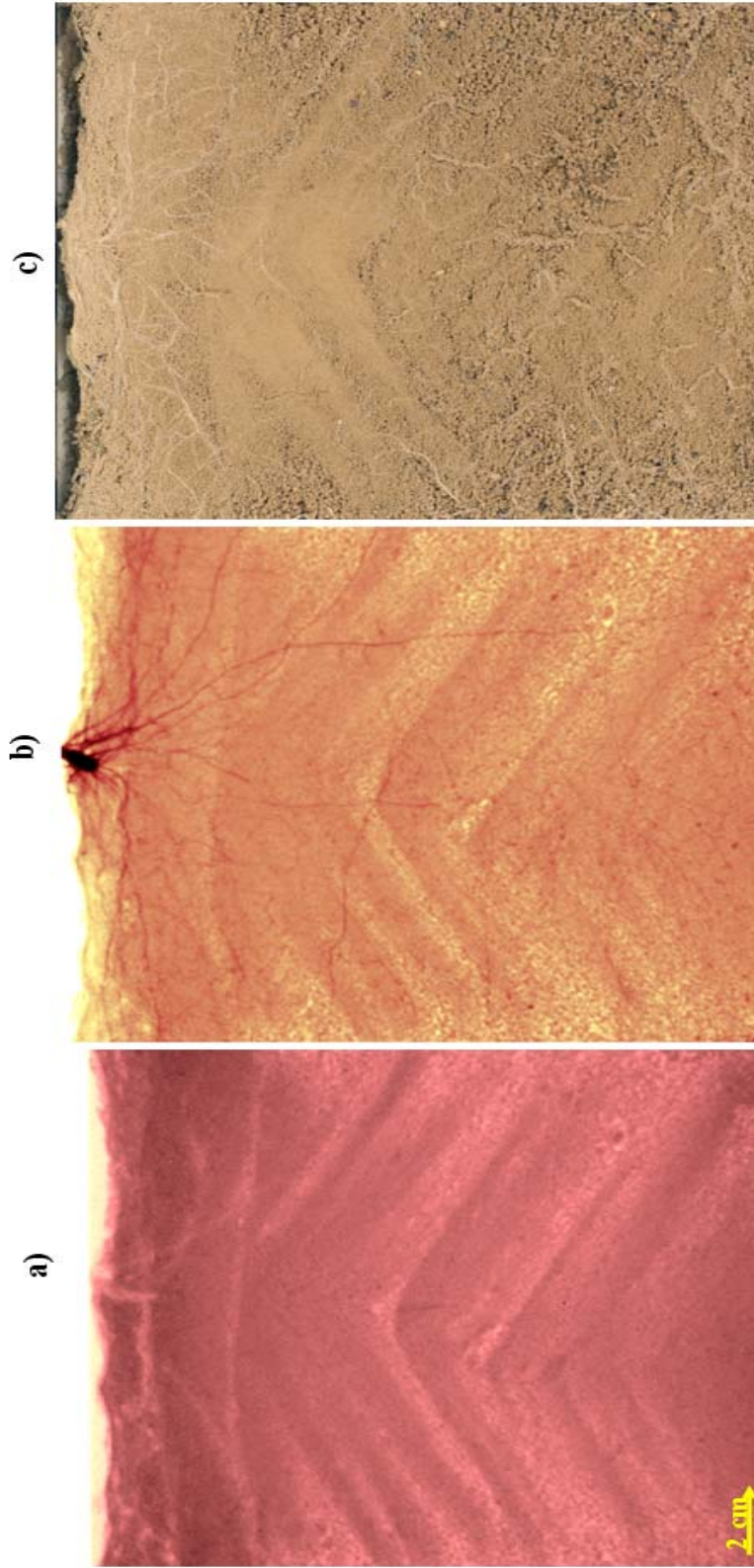


Figure 5.10: Comparison of X-ray (a), cold-neutron (b), and scan (c) images of a 7 weeks old tomato (*Lycopersicon sculentum Mill*) taken on the same day. No roots are visible in the X-ray image and the neutron image fails to reveal the fine roots especially in the bottom of the slab (which is clearly visible in the scan image) although it reveals the thicker roots in the upper part of the slab.

#### 5.4.6 Comparing NR with X-ray radiography and soil scanning

Figure 5.8 shows X-ray, cold-neutron, and scan images of a 7 weeks old *Cicer arietinum* plant taken on the same day. Due to the weak contrast between soil and plant roots in the X-ray image, (Figure 5.8a), only major roots with a diameter of at least 1.5 mm could be seen. Roots had a lower X-ray  $\Sigma$  and appeared brighter than the surrounding soil because of their lower density and composition of light elements. Thus, most roots were veiled in the soil background. However, X-ray images provided detailed information on the soil structure: textural layers created by the filling process and the cracks in the soil were clearly visible. Neutron radiography provided a much higher contrast between the roots and the soil (Figure 5.8b). Using microfocus X-ray sources could improve the spatial resolution but does not necessarily improve the contrast between roots and the surrounding soil. The roots appeared darker than the surrounding soil in neutron radiograph due to their higher neutron attenuation coefficient than the soil. Not only main roots, but also lateral roots were also clearly visible. Figure 5.8c shows a scan of the soil surface after opening one side of the container. This method only showed roots on the surface and could not give a picture of roots enmeshed in the opaque soil. But scan images could be useful to estimate the proportion of roots with a diameter of  $< 2$  mm, which were not detectable using NR. These very fine roots are mostly lost when roots are physically separated from soil. In fact almost all the fine roots sampled after the imaging by separating roots manually from soil had a diameter larger than 0.2 mm.

The X-ray and cold-neutron images of *Berkheya coddii* (Figure 5.9a and b) had similar characteristics as the respective images of *Cicer arietinum*. Because *Berkheya coddii* also produces fine roots ( $< 2$  mm in diameter) in addition to the coarse main roots, the scan of the opened side of the soil (Figure 5.9c) revealed many roots that were not visible in the neutron radiograph. The enlargement in Figure 5.9c shows roots with thickness of 0.12 mm that could not be seen in the neutron radiograph because it was below the root-detection limit (0.2 mm). However, the root with thickness of 0.25 mm was clearly visible in both images.

*Lycopersicon esculentum* produces a fibrous rooting system of which most of the roots are in the range of 0.2 mm and thinner. Comparing the scanned image (Figure 5.10c) with the neutron radiograph (Figure 5.10b) revealed many fine roots that were only visible in the scanned image. These roots were mostly located at the bottom part of the container. In the X-ray radiograph (Figure 5.10a) of this plant, no roots were visible except for the main root which had a thickness of more than 7 mm and was clearly visible.

#### **5.4.7 Advantages and limitations of NR for the visualisation of plant roots**

With respect to quantitative root system analysis, NR is currently still limited at high soil  $\theta$  due to high neutron scattering, the biological limitations at low soil  $\theta$ , due to root dehydration. Improvements in instrumentation, in particular, higher resolution detector systems, will permit the visualisation of roots with a diameter of  $<0.2$  mm. Nevertheless, NR can image roots with a thickness of  $\geq 0.2$  mm and in a range of soil  $\theta$  (0.1-0.25) that is well suited for plant growth. Using thermal neutrons with higher energy and, therefore higher penetration, permits the visualisation of root growth at soil  $\theta > 0.25$  (data not shown), although the contrast is reduced.

### **5.5 Conclusions**

- The choice of the plant growth medium is of overriding importance for root quantification with NR. The medium should support plant growth and have a low neutron  $\Sigma$  at a soil water potential of -1 bar.
- Quantitative analysis of soil water and root distribution using NR requires scattering correction, especially when high concentrations of hydrogen are present in the system.
- The scattering corrected neutron  $\Sigma$  of soil and water was linearly related with the soil  $\theta$ , while the uncorrected one deviated from the linearity as soil  $\theta$  increase.
- At present, NR is limited to measuring roots with diameters of  $>0.2$  mm. However, it reveals more roots than X-ray radiographs or scanned images of the soil surface.
- The minimum detectable root thickness in our experiment was calculated to be 0.2 mm, although it could be improved using a thinner root-growth containers or improving the spatial resolution of the detection system.

### **5.6 Acknowledgements**

This study was funded by the Swiss National Science Foundation

## 5.7 References

- Allen, R.G., Pererira, L.S., Raes, D. & Smith, M. 1998. *Crop Evapotranspiration. Guidelines for Computing Crop Water Requirements*. FAO, Rome.
- Bailey, I.F. 2003. A review of sample environments in neutron scattering. *Zeitschrift Fur Kristallographie*, **218**, 84-95.
- Bois, J.F. & Couchat, P. 1983. Comparison of the Effects of Water-Stress on the Root Systems of 2 Cultivars of Upland Rice (*Oryza-Sativa-L*). *Annals of Botany*, **52**, 479-487.
- Bottomley, P.A., Rogers, H.H. & Prior, S.A. 1993. Nmr Imaging of Root Water Distribution in Intact Vicia-Faba L Plants in Elevated Atmospheric Co<sub>2</sub>. *Plant Cell and Environment*, **16**, 335-338.
- Costa, C., Dwyer, L.M., Hamel, C., Muamba, D.F., Wang, X.L., Nantais, L. & Smith, D.L. 2001. Root contrast enhancement for measurement with optical scanner-based image analysis. *Canadian Journal of Botany-Revue Canadienne De Botanique*, **79**, 23-29.
- Doussan, C., Pages, L. & Pierret, A. 2003. Soil exploration and resource acquisition by plant roots: an architectural and modelling point of view. *Agronomie*, **23**, 419-431.
- Fitz, W., Puschenreiter, M., Schweiger, P. & Wenzel, W.W. 2005. Novel tools for investigating rhizosphere processes. *Abstracts of Papers of the American Chemical Society*, **230**, U1789-U1790.
- Furukawa, J., Nakanishi, T.M. & Matsubayashi, H. 1999. Neutron radiography of a root growing in soil with vanadium. *Nuclear Instruments & Methods in Physics Research Section a-Accelerators Spectrometers Detectors and Associated Equipment*, **424**, 116-121.
- Gregory, P.J., Hutchison, D.J., Read, D.B., Jenneson, P.M., Gilboy, W.B. & Morton, E.J. 2003. Non-invasive imaging of roots with high resolution X-ray micro-tomography. *Plant and Soil*, **255**, 351-359.
- Hall, L.D., Amin, M.H.G., Dougherty, E., Sanda, M., Votrubova, J., Richards, K.S., Chorley, R.J. & Cislerova, M. 1997. MR properties of water in saturated soils and resulting loss of MRI signal in water content detection at 2 tesla. *Geoderma*, **80**, 431-448.
- Hassanein, R., Lehmann, E. & Vontobel, P. 2005. Methods of scattering corrections for quantitative neutron radiography. *Nuclear Instruments & Methods in Physics Research Section a-Accelerators Spectrometers Detectors and Associated Equipment*, **542**, 353-360.
- Hassanein, R.K. 2006. *Correction methods for the quantitative evaluation of thermal neutron tomography*. Doctoral Diss. ETH No. 16809, ETH Zurich, Switzerland.
- Heyes, J.A. & Clark, C.J. 2003. Magnetic resonance imaging of water movement through asparagus. *Functional Plant Biology*, **30**, 1089-1095.

- Hoagland, D.R. & Arnon, D.I. 1938. The water culture method for growing plants without soil. *Calif. Agric. Exp. Stn*, **347**, 1–39.
- Kasperl, S. & Vontobel, P. 2005. Application of an iterative artefact reduction method to neutron tomography. *Nuclear Instruments & Methods in Physics Research Section a-Accelerators Spectrometers Detectors and Associated Equipment*, **542**, 392-398.
- Kuchenbuch, R.O. & Ingram, K.T. 2002. Image analysis for non-destructive and non-invasive quantification of root growth and soil water content in rhizotrons. *Journal of Plant Nutrition and Soil Science-Zeitschrift Fur Pflanzenernahrung Und Bodenkunde*, **165**, 573-581.
- Kuhne, G., Frei, G., Lehmann, E. & Vontobel, P. 2005. CNR - the new beamline for cold neutron imaging at the Swiss spallation neutron source SINQ. *Nuclear Instruments & Methods in Physics Research Section a-Accelerators Spectrometers Detectors and Associated Equipment*, **542**, 264-270.
- Lehmann, E., Pleinert, H., Williams, T. & Pralong, C. 1999. Application of new radiation detection techniques at the Paul Scherrer Institut, especially at the spallation neutron source. *Nuclear Instruments & Methods in Physics Research Section a-Accelerators Spectrometers Detectors and Associated Equipment*, **424**, 158-164.
- Majdi, H. 1996. Root sampling methods - Applications and limitations of the minirhizotron technique. *Plant and Soil*, **185**, 255-258.
- Matsushima, U., Kawabata, Y., Hino, M., Geltenbort, P. & Nicolai, B.M. 2005. Measurement of changes in water thickness in plant materials using very low-energy neutron radiography. *Nuclear Instruments & Methods in Physics Research Section a-Accelerators Spectrometers Detectors and Associated Equipment*, **542**, 76-80.
- Menon, M., Robinson, B., Oswald, S.E., Kaestner, A., Abbaspour, K.C., Lehmann, E. & Schulin, R. 2007. Visualization of root growth in heterogeneously contaminated soil using neutron radiography. *European Journal of Soil Science*, **58**, 802-810.
- Moran, C.J., Pierret, A. & Stevenson, A.W. 2000. X-ray absorption and phase contrast imaging to study the interplay between plant roots and soil structure. *Plant and Soil*, **223**, 99-115.
- Naftel, S.J., Martin, R.R., Sham, T.K., Macfie, S.M. & Jones, K.W. 2001. Micro-synchrotron X-ray fluorescence of cadmium-challenged corn roots. *Journal of Electron Spectroscopy and Related Phenomena*, **119**, 235-239.
- Nakanishi, T.M., Okuni, Y., Furukawa, J., Tanoi, K., Yokota, H., Ikeue, N., Matsubayashi, M., Uchida, H. & Tsiji, A. 2003. Water movement in a plant sample by neutron beam analysis as well as positron emission tracer imaging system. *Journal of Radioanalytical and Nuclear Chemistry*, **255**, 149-153.

- Nakanishi, T.M., Okuni, Y., Hayashi, Y. & Nishiyama, H. 2005. Water gradient profiles at bean plant roots determined by neutron beam analysis. *Journal of Radioanalytical and Nuclear Chemistry*, **264**, 313-317.
- Pierret, A., Doussan, C., Garrigues, E. & Mc Kirby, J. 2003. Observing plant roots in their environment: current imaging options and specific contribution of two-dimensional approaches. *Agronomie*, **23**, 471-479.
- Pierret, A., Moran, C.J. & Doussan, C. 2005. Conventional detection methodology is limiting our ability to understand the roles and functions of fine roots. *New Phytologist*, **166**, 967-980.
- Sutton, R.F. & Tinus, R.W. 1983. Root and root system terminology. *Forest Science Monograph*, **24**, pp 137.
- Vogt, K.A., Vogt, D.J. & Bloomfield, J. 1998. Analysis of some direct and indirect methods for estimating root biomass and production of forests at an ecosystem level. *Plant and Soil*, **200**, 71-89.
- Waisel, Y., Eshel, A. & Kafkafi, Z. eds. 2002. *Plant Roots: The Hidden Half*. Marcel Dekker, New York.
- Whalley, W.R., Lipiec, J., Stepniewski, W. & Tardieu, F. 2000. *Control and measurement of the physical environment in root growth experiments*. In: Smit, A.L., Bengough, A.G., Engels, C., Noordwijk, M., Pellerin, S., van de Geijn, S. (Eds.), *Root Methods: A Handbook*. Springer, Berlin, pp. 75-112.
- Willatt, S.T. & Struss, R.G. 1979. Germination and Early Growth of Plants Studied Using Neutron Radiography. *Annals of Botany*, **43**, 415-&.
- Willatt, S.T., Struss, R.G. & Taylor, H.M. 1978. Insitu Root Studies Using Neutron Radiography. *Agronomy Journal*, **70**, 581-586.



---

## 6 Conclusions

---

New non-destructive techniques with high spatial and temporal resolutions are needed to study the dynamic interactions of plant roots and soil. The objectives of this study were to: (i) develop, adapt and apply MRI to map distribution of Ni in porous media, (ii) develop and apply a method to map Ni distribution within the root cross-sections, (iii) develop a quantitative approach to monitor root development and growth in soil, and (iv) study the dynamics of Ni concentration in the rhizosphere.

### 6.1 MRI to study dynamics of Ni

MRI signals were found to be sensitive to the presence of ferromagnetic and paramagnetic components, which occur naturally in soils. Quartz sand is a suitable replacement for soil in rhizosphere studies. However, the best porous medium for MRI purpose was found to be porous glass beads. A limitation regarding the application of MRI to porous media is the presence of air bubbles. Abrupt changes of magnetic susceptibility across the phase boundaries disturb the MRI images. Another limitation of MRI was found to be the loss of signal-to-noise ratio with decreasing water saturation. Since hydrogen is the signal bearing component, low water contents result in poor signal to noise ratios. While Ni usually occurs in soil in two major forms of soluble and sorbed on the solid particle, MRI is not able yet to differentiate different forms of Ni.

Although MRI suffers from the above-mentioned drawbacks, it is a valuable technique to monitor paramagnetic ions in porous media. Among the various MRI sequences, T1FFE was shown to resolve Ni concentrations down to 30 mg litre<sup>-1</sup>, while the T<sub>1</sub> mapping we adapted and used here was able to detect Ni concentrations down to 1.5 mg litre<sup>-1</sup>. The T<sub>1</sub> mapping method was successfully used to map variations in Ni concentration with a spatial resolution of 0.21 mm and a temporal resolution of less than a minute.

## 6.2 LA-ICP-MS and DMG-staining to study Ni distribution in root cross-sections

LA-ICP-MS has an important advantage. It allows simultaneous multi-elemental analysis of a sample, provides a suitable spatial resolution at tissue level, and offers the possibility of mapping the spatial distribution of elements in 2 or even 3-dimensions. The main disadvantage is the need to fix the sample and as it consumes the material during analysis it is a destructive method.

DMG-staining was found to be a quick, low-cost, and simple method for the qualitative evaluation of Ni distribution in plant tissues. This method can be further developed and has the potential to become a semi-quantitative method.

There is generally a risk of redistribution of elements in a sample during preparation. We found very similar patterns of Ni distribution in the root cross-sections of *Berkheya coddii* using the two methods, LA-ICP-MS and DMG-staining (Chapter 4). This suggests that using a suitable preparation procedure, the risk of redistribution is not severe at the tissue level.

## 6.3 Neutron radiography to monitor root development in soil

NR gave much better images of developing root system than X-ray and scan images. Image analysis is of crucial importance for the discrimination of roots from other structures in the soil and to perform quantitative analysis of the images. Neutron scattering corrections greatly improved the relationship between the neutron attenuation coefficient and the water content of soil or roots, which is essential for root detection. The minimum detectable root thickness could be improved by using thinner root-growth containers.

The main drawback of NR is the still limited availability of neutron beam lines and the cost of the infrastructure to run a beam line. However, this was also the case with many other techniques that in the mean-time have become more and more available to scientists at decreasing cost. Nuclear magnetic resonance imaging (NMRI), synchrotron X-ray, and X-ray absorption fine structure (XAFS) are such examples.

## 6.4 Ni dynamic in the rhizosphere of *Berkheya coddii*

Using MRI (Chapter 3) we found that Ni was excluded by *Berkheya coddii* roots at the high concentrations used in the experiment. Although the solution Ni concentration that was used here (10 mg litre<sup>-1</sup>) was high compared to Ni concentrations found in usual soils, such concentrations do occur in serpentine soils where most Ni accumulator plants have evolved.

The distribution patterns of Ni in root cross-sections of *Berkheya coddii* (Chapter 4) suggest that the uptake was selective. Using numerical simulations we showed that the gradient in Ni adjacent to the roots was determined by the rate of transpirational water flow towards the roots, the rate of Ni uptake rate by the roots and the rate of Ni diffusion down the concentration gradient in the rhizosphere adjacent to the roots.

## 6.5 Outlook

In this study, new techniques were developed, adapted and applied to the rhizosphere of *Berkheya coddii*. The results suggest that future research should focus on the following aspects:

- MRI has the potential for answering specific questions on rhizosphere processes by developing new imaging sequences. Combining two different sequences to measure  $T_1$  and water content at the same time can give a better understanding of Ni uptake and distribution under unsaturated conditions. There is also the possibility of improving the Ni detection limit down to concentrations of less than  $1 \text{ mg litre}^{-1}$  by increasing the measurement time or at the expense of spatial resolution. This could reveal root-Ni interactions also at lower dissolved Ni concentrations than found in highly contaminated soils.
- Neutron radiographs provide information regarding water distribution in soil, while X-ray images give details of the soil particles itself. Combining the two types of images can give a more comprehensive picture of the whole system.
- Additional information on the physiological Ni translocation mechanisms in *Berkheya coddii* is needed to get a better understanding of Ni hyperaccumulation in this plant.

In conclusion, there are numerous newly developed techniques in various disciplines that can be further developed or adapted to rhizosphere studies and can ease the difficulties in this field of research. This study disclosed some possibilities in this direction.



---

## Curriculum Vitae

---

Surname : Moradi  
First name : Ahmad  
Date of birth : 21 March 1977  
Citizen of : Iran

### Education

1997 – 2001 Bachelor's degree in Soil Science, Department of Soil Science, College of Agriculture, Bu-Ali-Sina University, Hamadan, Iran  
2001 – 2003 Master's degree in Soil Science with specialization in solute transport in soils, Soil Science Department, College of Agriculture, Isfahan University of Technology (IUT), Isfahan, Iran

### Occupation

1999 – 2001 Teaching assistant, Department of Soil Science, College of Agriculture, Bu-Ali-Sina University, Hamadan, Iran  
2004 – Present PhD student and teaching assistant, Soil Protection Group, Institute of Terrestrial Ecosystems, ETH Zurich

